Line Formation in M-type Stars

Dissertation
zur Erlangung des mathematisch-naturwissenschaftlichen
Doktorgrades
"Doctor rerum naturalium"
an der Georg-August-Universität Göttingen

vorgelegt von
Sebastian Wende
aus Osterode/Harz

Göttingen, den 06.10.2010

Referent: Prof. Dr. Stefan Dreizler
Korreferent I: Dr. Ansgar Reiners
Korreferent II: Prof. Dr. Peter Hauschildt
Tag der mündlichen Prüfung: 28.10.2010

Abstract

The measurement of line broadening in cool stars is, in general, a difficult task. In order to detect slow rotation or weak magnetic fields, an accuracy of $1\,\mathrm{km\,s^{-1}}$ is needed. In this regime, the broadening from convective motion becomes important. Molecular FeH provides a large number of sharp and isolated absorption lines that can be used to measure the afore mentioned quantities with high accuracy.

I present an investigation of the velocity fields in early to late M-type star hydrodynamic models, and I simulate their influence on FeH molecular line shapes. The M star model parameters range between $\log g$ of $3.0 - 5.0$ and effective temperatures from 2500 K to 4000 K. These results can then be applied on a large sample of FeH lines in order to use their full potential in characterising the atmospheres of cool stars.

My aim is to investigate the T_{eff}- and $\log g$-dependence of the velocity fields and express them in terms of micro- and macro-turbulent velocities in the one dimensional sense. I present a direct comparison between 3D hydrodynamical velocity fields and 1D turbulent velocities. The velocity fields strongly affect the line shapes of FeH, and it is one of the goals to give a rough estimate of the $\log g$ and T_{eff} parameter range in which 3D spectral synthesis is necessary and where 1D synthesis suffices. I distinguish between the velocity-broadening from convective motion and the rotational- or Zeeman-broadening in M-type stars which is planned to be measured. For the latter, FeH lines are an important indicator. I also provide an FeH atlas for M-type stars in the spectral region from 986 nm to 1077 nm (Wing-Ford band). This atlas can be used to identify and characterise FeH lines in spectra of cool stars in the investigated region, where most of their flux is emitted. I also show how this large number of lines can be used to determine effective temperatures and detect magnetically sensitive lines.

In order to calculate M-star structure models, I employ the 3D radiative-hydrodynamics (RHD) code `CO`^{5}`BOLD`. The spectral synthesis in these models is performed with the line synthesis code `LINFOR3D`. The 3D velocity fields are described in terms of Gaussian standard deviations and are projected onto the line of sight to include geometrical and limb-darkening effects. The micro- and macro-turbulent velocities are determined with the “curve of growth” method and the convolution with a Gaussian velocity profile, respectively. To characterize the $\log g$ and T_{eff} dependence of FeH lines, the equivalent widths, line widths, and line depths are examined.

In order to create the FeH atlas, the FeH lines were identified in a CRIRES spectra of the magnetically inactive, slowly rotating, M5.5 dwarf GJ1002. I calculated model spectra for the selected spectral region with theoretical FeH line data in order to compare them with the observations. In general, this line list agrees with the observed data, but several individual lines differ significantly in position or in line strength. After the identification of as many FeH lines as possible, I corrected the line data for position and line strength to provide an accurate atlas of FeH absorption lines. For all lines, I used a Voigt function to obtain their positions and equivalent widths. The identification with theoretical lines was done by hand. For confirmation of the identified lines, I used statistical methods, cross-correlation techniques, and line intensities. The line intensities can be used to determine effective temperatures of the stars, either by using the whole set of lines or only line ratios.

The velocity fields in M-stars strongly depend on $\log g$ and T_{eff}. They become stronger with decreasing $\log g$ and increasing T_{eff}. The projected velocities from the 3D models agree within $\sim\ 100\,\mathrm{m\,s^{-1}}$ with the 1D micro- and macro-turbulent velocities. Correspondingly, the FeH line quantities systematically depend on $\log g$ and T_{eff}.

In the CRIRES spectrum of GJ1002, I was able to identify FeH lines from the $(0,0)$, $(1,0)$, $(1,1)$, $(2,1)$, $(2,2)$, $(3,2)$, and $(4,3)$ vibrational bands and correct the positions of some lines. The deviations between theoretical and observed positions follow a normal distribution approximately around zero. In order to empirically correct the line strengths, I determined T_{eff}, instrumental broadening (rotational broadening) and a van der Waals enhancement factor for the FeH lines in GJ1002. I also give the scaling factors for the Einstein A values to correct the line strengths. With the identified lines, I derived rotational temperatures from the line intensities for GJ1002. I was also able to use a pair of FeH lines to determine effective temperatures in a set of CES spectra of M dwarfs. From synthetic spectra with these determined temperatures it was possible to derive the stellar parameters surface gravity and metallicity.

I conclude that the influence of hydrodynamic velocity fields on line shapes of M-type stars can well be reproduced with 1D broadening methods. FeH lines turn out to provide a means to measure $\log g$ and T_{eff} in M-type stars. Since different FeH lines all behave in a similar manner, they provide an ideal measure for rotational and magnetic broadening.

I also conclude that FeH lines can be used for a wide variety of applications in astrophysics. With the identified lines it is possible, for example, to characterize magnetically sensitive or very temperature sensitive lines, which can be used to investigate the atmospheres of M-type stars.

Contents

Contents **ix**

List of Figures **xii**

List of Tables **xiii**

1 Introduction **1**
- 1.1 M-type Stars 1
- 1.2 Molecular FeH Absorption 2
- 1.3 Goals of this Work 3

2 Radiative Hydrodynamics **5**
- 2.1 Hydrodynamics 5
  - 2.1.1 Reference Frames 5
  - 2.1.2 Equation of Continuity 5
  - 2.1.3 Equation of Momentum 6
  - 2.1.4 Equation of total Energy 7
- 2.2 Radiative Transfer 8
  - 2.2.1 Specific Intensity 8
  - 2.2.2 Mean Intensity 8
  - 2.2.3 Flux 9
  - 2.2.4 Radiative Pressure 9
  - 2.2.5 Optical Depth 9
  - 2.2.6 Source Function 10
  - 2.2.7 Stefan-Boltzmann Law 11
  - 2.2.8 Radiative Transfer Equation 12
  - 2.2.9 Radiative Equilibrium 13
- 2.3 Equation of State 13
- 2.4 Convection 14

3 Atmosphere and Line Formation Codes **17**
- 3.1 `CO`^{5}`BOLD` Atmosphere Code 17
- 3.2 `MARCS` and `PHOENIX` Atmospheres 18
- 3.3 Line Formation Code `LINFOR3D` 18
- 3.4 Line Formation Code `SYNTH3` (`SYNMAST`) 19

4 Spectroscopy of Diatomic Molecules 21
- 4.1 General Treatment of Diatomic Molecules . . . 21
- 4.2 Rotational Spectroscopy . . . 25
  - 4.2.1 Selection Rules . . . 25
  - 4.2.2 Intensities . . . 26
  - 4.2.3 Non-Rigid Rotation . . . 27
- 4.3 Vibrational Spectroscopy . . . 29
  - 4.3.1 The Anharmonic Oscillator . . . 29
  - 4.3.2 Selection Rules . . . 30
  - 4.3.3 Intensities . . . 32
- 4.4 Electronic Spectroscopy . . . 33
  - 4.4.1 Selection Rules . . . 34
  - 4.4.2 Vibronic Transitions . . . 34
  - 4.4.3 Rovibronic Transitions . . . 36
  - 4.4.4 Rovibronic Intensities . . . 36

5 The FeH Molecule 39
- 5.1 Molecular Data . . . 39
  - 5.1.1 Ionisation Energy of FeH . . . 39
  - 5.1.2 Partition Function of FeH . . . 41
- 5.2 Van der Waals Broadening . . . 42
- 5.3 Appearance of FeH in Stellar Spectra . . . 42

6 Velocity Fields in M-type Stars 45
- 6.1 3D Model Atmospheres . . . 45
  - 6.1.1 `CO`^{5}`BOLD` Atmosphere Grid . . . 45
  - 6.1.2 Atmosphere Structures . . . 46
- 6.2 Velocity Fields in the `CO`^{5}`BOLD`-Models . . . 47
  - 6.2.1 Reduction of the 3D Velocity Fields . . . 51
  - 6.2.2 Radial Velocity Shifts . . . 56
  - 6.2.3 Micro- and Macro-Turbulent Velocities . . . 57

7 T_{eff}- and $\log g$-Dependence of FeH Molecular Lines 61
- 7.1 An Ensemble of 3D- and ⟨3D⟩-FeH Lines . . . 61
- 7.2 FeH Line Shapes . . . 62
  - 7.2.1 Equivalent Width W_λ . . . 63
  - 7.2.2 FWHM . . . 65
  - 7.2.3 Line Depth . . . 66

8 Line by Line Identification of FeH in the z-band 67
- 8.1 Data . . . 67
  - 8.1.1 CRIRES Spectra of GJ1002 . . . 67
  - 8.1.2 Theoretical FeH Molecular Data and Line Synthesis . . . 69
- 8.2 Methods . . . 70
  - 8.2.1 Voigt Fit . . . 70
  - 8.2.2 Method of Coincidence . . . 71
  - 8.2.3 Theoretical Line Strength . . . 72
  - 8.2.4 Line Strength Correction . . . 74

8.3 Results . . . 75
    8.3.1 Atomic Line Identification and Unidentified Lines . . . 75
    8.3.2 FeH Line Identification . . . 77
    8.3.3 Corrections to the Line Strengths . . . 85

9 Temperature Estimations Using FeH 89
9.1 Rotational Temperatures as a Measure of Atmospheric Temperatures . . . 89
9.2 Deriving Effective Temperatures with the Line Ratio Method . . . 90
    9.2.1 Basic Idea . . . 90
    9.2.2 First Results . . . 92

10 Magnetically Sensitive FeH Lines: An Outlook 97
10.1 Identification of Sensitive Lines . . . 97
10.2 Theoretical Zeeman Splitting . . . 98
10.3 Comparison Between Computations and Observations . . . 99

11 Summary and Conclusion 101

Bibliography I

List of Figures

4.1 Morse potential vs. harmonic oscillator potential 23
4.2 Rotational branches 27
4.3 Energy levels of the Morse potential 30
4.4 Franck-Condon principle 35
4.5 Vibrational band structure 37

5.1 Ionisation energy vs. dissociation energy 40
5.2 FeH partition function 41
5.3 FeH concentration as function of T_{eff} 41
5.4 Influence of ionisation energy on van der Waals broadening 43

6.1 Convective granulation pattern 48
6.2 Atmospheric structure of M dwarfs 48
6.3 Histogram of the velocity distribution in the vertical direction 49
6.4 Velocity fields vs. optical depth (T_{eff} sequence) 50
6.5 Velocity fields vs. optical depth ($\log g$ sequence) 50
6.6 Flow field of an M dwarf 51
6.7 Weighted velocities (T_{eff} sequence) 52
6.8 Weighted velocities ($\log g$ sequence) 52
6.9 Projection factor 53
6.10 Broadened FeH lines 58
6.11 Micro-turbulent velocities as a function of $\log \tau$ 58
6.12 Micro- and macro turbulent velocities (T_{eff} sequence) 59
6.13 Micro- and macro turbulent velocities ($\log g$ sequence) 59

7.1 FeH shape variations with T_{eff} 63
7.2 FeH shape variations with $\log g$ 63
7.3 FeH line quantity variations with T_{eff} 64
7.4 FeH line quantity variations with $\log g$ 64
7.5 FeH 3D abundance corrections 65

8.1 Wing-Ford band 68
8.2 FeH vibrational bands 68
8.3 Multiple Voigt fit 72
8.4 Influence of variable absorber number 72
8.5 Labeled spectrum of GJ1002 77
8.6 Histogram of the residuals between computed line positions and observed ones . . 78

8.7 Histogram of predicted and identified FeH lines 78
8.8 Cross-correlation curves 80
8.9 Logarithm of W_λ^{obs} and theoretical line strength vs. lower level energies 81
8.10 Logarithm of W_λ^{comp} and theoretical line strength against lower level energies . . . 82
8.11 $\log_{10}\tau_{mean}$ and W_λ as a function of lower state energy 82
8.12 Number of FeH molecules as a function of optical depth 83
8.13 χ^2 maps 86
8.14 Observed and computed spectrum of GJ1002 before and after A correction 87
8.15 Scaling factor for the Einstein A values against rotational quantum number 87

9.1 Rotational temperatures 90
9.2 Line ratio method 91
9.3 Resolution dependence of line ratio 91
9.4 Ti-FeH line pair shapes 92
9.5 Effective temperatures determined from line ratio (`MARCS`) 93
9.6 Effective temperatures determined from line ratio (`PHOENIX`) 93
9.7 CES M dwarf spectra I 95
9.8 CES M dwarf spectra II 96

10.1 Comparison between GJ1224 and GJ1002 98
10.2 Comparison between computed spectra with and without magnetic field 98

List of Tables

4.1 33

6.1 Table of model quantities 47
6.2 Line displacements due to convective motion 56

7.1 Several quantities of the investigated FeH lines 62

8.1 Identified atomic lines 75
8.2 List of unidentified lines deeper then 0.9. 76
8.3 Results from the coincidence method for lines with $W_\lambda > 2\,\mathrm{m\AA}$ 79
8.4 FeH molecular data of the identified lines 84

9.1 Derived stellar parameters for the set of M dwarfs 93

Every Man and Every Woman is a Star[1]

Alice & Marin

---

[1] The Book of the Law, A.C. 1904

Chapter 1

Introduction

Most of our knowledge about stars comes from spectroscopic investigation of atomic or molecular lines. In Sun-like and hotter stars, the strength and shape of atomic spectral lines provides information on atmospheric structure, velocity fields, rotation, magnetic fields, etc. Measuring the effects of velocity fields on the shape of spectral lines requires a spectral resolving power between $R \sim 10,000$ ($\mathit{\Delta} v = 30\,\mathrm{km\,s^{-1}}$) for rapid stellar rotation, $R \geq 30,000$ ($\mathit{\Delta} v = 10\,\mathrm{km\,s^{-1}}$) for slower rotation and high turbulent velocities, and resolution on the order of $R \sim 100,000$ for the analysis of Zeeman splitting and line shape variations due to slow convective motion.

In slowly rotating Sun-like stars, usually a large number of relatively isolated spectral lines are available for the investigation of Doppler broadened spectral lines. These lines are embedded in a clearly visible continuum allowing a detailed analysis of individual lines at high precision. At cooler temperatures, the number of atomic lines increases so that more and more lines become blended, rendering the investigation of individual lines more difficult.

At temperatures around 4000 K, molecular lines, predominantly VO and TiO, start to become important. At optical wavelengths, molecular bands in general consist of many lines that are blended so that the absorption mainly appears as an absorption band; individual molecular lines are difficult to identify. At temperatures in the M type star regime (4000 K and less), atomic lines start to vanish because atoms are mainly neutral and higher ionization levels are weakly populated. Only alkali lines that are strongly affected by pressure broadening appear. Thus, the detailed spectroscopic investigation of velocity fields in M dwarfs is very difficult at optical wavelengths and one has to go in the near infra red, where M-type stars become brightest and a lot of molecular bands provide a large number of narrow and well isolated lines.

1.1 M-type Stars

The spectral class of M-type stars is characterized by the appearance of TiO bands in early M stars and of VO bands in late M stars, since TiO bands become saturated (Bessell, 1991). An illustrative overview is given in Kirkpatrick et al. (1991), who also introduced a calibration based on the relative strengths of spectral features in the range 630 nm − 900 nm and the overall spectral slope across these wavelengths. Bessell (1991) used color-color diagrams in the range of the TiO and VO bands to define a classification of M dwarfs. From those color-color diagrams, which can be translated into Hertzsprung-Russel diagrams, it is possible to derive effective temperatures of these stars. M star effective temperatures range from $\sim 4\,000\,\mathrm{K}$ for early M stars down to $2\,500\,\mathrm{K}$ for late M stars. With the knowledge of the distance of the star, it is possible to interfere radii from effective temperatures and measured luminosities. A more approximately way, but easier is to match black bodies to the spectral energy distribution of the stars. The obtained radii of M dwarfs, range from $\sim 0.6 R_\odot$ for early M dwarfs, to $\sim 0.1 R_\odot$ for late ones. The masses of M stars are very difficult to obtain and only a few are known so far. Most of them were derived from their motion in a binary system and range from $\sim 0.6 M_\odot$ for early M stars, to less then $\sim 0.1 M_\odot$ for late M stars. The latter value almost approaches the hydrogen burning limit and these stars are close to the brown dwarf regime (Reid & Hawley, 2005).

The mass range that defines M-type stars is also the range in which a substantial transition in atmospheric structure takes place. The early M dwarfs exhibit a partly convective atmosphere and become fully convective towards later type stars (Kippenhahn & Weigert, 1990). The transition approximately takes place around spectral type M4 (but it also depends on the evolutionary stage of the star). It is interesting how this change of stellar structure affects other quantities like (differential) rotation or activity. The latter one becomes very significant towards late M dwarfs. Where only 0.8 % of M0 dwarfs show H_α emission (which is an indicator for magnetic activity), more than 70 % of the M8 dwarfs show signs of magnetic activity (Reid & Hawley, 2005). The connection between rotation and activity in these cool stars has been investigated by several authors in the last years (e.g. Basri et al., 1996; Simon, 2001; Messina et al., 2001).

The rotation-activity connections shows, that activity saturates at large rotational velocities. The saturation velocities depend on the spectral type: it is about $30\,\mathrm{km\,s^{-1}}$ for G-type stars, and only about $5\,\mathrm{km\,s^{-1}}$ for M dwarfs (Reiners, 2007). For such slow rotational velocities, the distinction between different broadening mechanisms, like magnetic-, pressure-, Doppler-, or turbulent-broadening, becomes difficult. Due to this, a set of narrow and well isolated spectral features is needed.

Because M-type stars emit the bulk of their flux at infrared wavelengths redward of $1\,\mu$m, observation of high SNR spectra is in principle easier in the infrared. Furthermore, M type stars exhibit a number of molecular absorption bands in the infrared, for example FeH . In these bands, the individual lines are relatively well separated and provide a good tracer of stellar velocity fields. The lines are intrinsically much narrower than atomic lines in sun-like stars because Doppler broadening, due to the temperature related motion of the atoms and molecules, is much reduced because of their higher masses. The latter fact is also the reason for a reduced pressure broadening, since the impact of the perturbers is smaller on molecules. Thus, the lines can be used for the whole arsenal of line profile analysis that has been applied successfully to Sun-like stars over the last decades.

1.2 Molecular FeH Absorption

The FeH molecule provides a particularly large number of strong and well isolated lines in the z-band ($\sim$ 990–1080 nm). It is the main opacity contributor in this region for late-type dwarf stars, and can be used for high-precision spectroscopy. FeH provides numerous unblended lines that are sufficiently narrow to measure small broadening effects or variations in the line position.

Wing & Ford (1969) first discovered the molecular band around 991 nm in the spectra of the cool dwarf Wolf 359. This band was also found in S-type stars (Wing, 1972) and was identified as the $(0,0)$ vibrational band of the FeH molecule by Nordh et al. (1977). An extensive analysis was carried out by Phillips et al. (1987). They identified seven vibrational bands of the ${}^4\Delta - {}^4\Delta$ electronic transition of the FeH molecule and provided tables with molecular constants and quantum numbers. An important theoretical work, partly based on the previous one, was carried out by Dulick et al. (2003). They computed a line list for the $F^4\Delta - X^4\Delta$ electronic transition and provided extensive tables of molecular data with quantum numbers and line intensities.

FeH absorption bands have also been detected in the J- and H-band with medium resolution spectra (Cushing et al., 2003). In the H-band the $E^4\Pi - A^4\Pi$ electronic transition is visible (Hargreaves et al., 2010). That FeH can be used to determine effective temperatures was shown, for example, by Schiavon et al. (1997) and will be shown also in this work. Its potential to measure magnetic field strengths was demonstrated by Reiners & Basri (2006, 2007). Theoretical work on the magnetic sensitivity of FeH was published by Afram et al. (2007, 2008).

Examples of analyses using FeH lines are the investigation of the rotation activity-connection in field M-dwarfs, which requires the measurement of rotational line broadening with an accuracy of 1 km s^{-1} (Reiners, 2007). Another example is the measurement of magnetic fields comparing Zeeman broadening in magnetically sensitive and insensitive absorption lines (see e.g. Reiners & Basri, 2006). A precise analysis of FeH lines, however, is only possible if the underlying velocity fields in the M dwarf atmospheres are thoroughly understood, a point also investigated in this work.

1.3 Goals of this Work

This dissertation is basically theoretical work, since most of the investigations and results are based on theoretical atmosphere models and synthetic line formation.

Because M-type stars have convective atmospheres, this must be included in any modelling. This is most realistically done in terms of **Radiative Hydrodynamics** (RHD), which is the title and the content of the next chapter in which a rough overview of the basic equations of hydrodynamics and radiative transfer is given. The equations of hydrodynamics describe the motion of a fluid, those of radiative transfer, a radiative field and its interactions with the surroundings. Both have to be coupled in the case of a moving, radiating fluid. These equations are the background of atmosphere or line formation codes, which will be described in the chapter **Atmosphere and Line Formation Codes**. That will be in particular the `CO`^{5}`BOLD` code, which simulates small boxes of atmospheres (solar and stellar) in three dimensions. It is able to describe convective motions purely from the interaction of *voxels* (volume pixels) with each other inside the model cube. The results from these simulations can be compared to one dimensional atmospheres which are also described in this chapter. For the generation of model spectra, I used codes which can compute line formation in one and three dimensional atmospheres, depending on the application.

Since the main focus in this work will be on the FeH molecular lines as a tool to explore M star atmospheres, I also give an overview of the theoretical description of diatomic molecules. The chapter **Spectroscopy of Diatomic Molecules** contains the basic ideas and equations of rotational, vibrational, and electronic spectroscopy. In general these are combined into *rovibronic* transitions, which is also the case for FeH . In the chapter **The** FeH **Molecule**, I describe and derive necessary quantities to compute spectra of it.

With these tools at hand, it is possible to approach the first goal of this work, which is the investigation of the **Velocity fields in M-type stars**. In this chapter, a set of 3D M star atmosphere models are investigated. The models vary in effective temperature and surface gravity in order to span a wide range of stellar parameters. The atmospheric structure of these models is described as well as the resulting velocity fields. The velocity field from the RHD models is then compared with the spectroscopic quantities micro- and macro-turbulent velocities. The latter describes the broadening by convective motion. It will be the question if the use of micro- and macro-turbulent velocities in one dimensional atmospheres resample the effect of the three dimensional velocity fields on line shapes.

The second goal is to study the effect of different stellar parameters and the related velocity fields on FeH lines and is investigated in the chapter **T_{eff}- and $\log g$-dependence of FeH molecular lines**. The line quantities of interest are the equivalent width, line width, and line depth. To be not dependent on a certain line, a set of ten lines with different quantum numbers have been chosen.

After the characterisation of a set of FeH lines, the third goal is the identification of as much as possible FeH lines in high resolution spectra of GJ1002. GJ1002 is a M5.5 dwarf and exhibits a very weak magnetic field and very slow rotation. This makes it an ideal target to compare synthetic FeH spectra to the observations. The investigated region range from 990 nm to 1076.6 nm. With the identified lines, an atlas of this region with a corrected theoretical line list has been created, all described in the chapter **Line by Line Identification of FeH in the z-band**.

The fourth and last goal of this work was to apply the identified FeH lines to derive several stellar parameters. In the chapter **Temperature Estimations using FeH**, I show how line intensities of a large number of FeH lines can be used to explore the temperature of M dwarf atmospheres. As an alternative, the line ratios of FeH line pairs can also be used to determine effective temperatures of M dwarfs. Using results from the latter method, I compute M dwarf spectra and compare them with observations in order to determine surface gravities and metallicities of the stars.

The FeH lines can also be applied to determine magnetic fields in M stars. Because some FeH lines are sensitive to Zeeman splitting and others not, one can use the insensitive lines to match the stellar parameters and the sensitive lines to determine the magnetic field strength. In the chapter **Magnetically Sensitive FeH lines: An Outlook**, I will show how to detect sensitive lines and investigate their dependence on rotational quantum number and Ω. Finally I compute spectra including the effect of magnetic fields and compare the results with the observations.

Chapter 2

Radiative Hydrodynamics

In this chapter I introduce the basic concepts of radiative hydrodynamics applied to stellar atmospheres. One can consider the gaseous atmosphere of a star as a radiating fluid. The motion of this fluid is described by equations of hydrodynamics, and its radiation by equations of radiative transfer. Both sets of equations have to be coupled to account for the exchange of energy in form of heat, momentum and radiation.

2.1 Hydrodynamics

In order to describe the simplified basic equations of hydrodynamics, I will follow Mihalas (1999).

2.1.1 Reference Frames

For the motion of the fluid, a description in two different frames of reference is possible:

1. The *Eulerian description*, in which the flow is viewed from a fixed laboratory frame. Here, any property α of the fluid can be considered as a function of position $\mathbf{x}$ and time t,

   $$\alpha = \alpha(\mathbf{x}, t). \tag{2.1}$$

   Variations in space and time are then given by the derivatives $(\partial/\partial x^i)$ and $(\partial/\partial t)$, respectively.

2. In the *Lagrangian description*, one studies the time variations of any quantity of a particular fluid parcel, while following its motion. These variations of the properties with time are described by the *fluid-frame time derivative* (D/Dt).

Both reference frames are connected via

$$\frac{D\alpha}{Dt} = \frac{\partial\alpha}{\partial t} + (\mathbf{v} \cdot \nabla)\alpha. \tag{2.2}$$

2.1.2 Equation of Continuity

If one considers a material volume element in the Lagrangian description, then it is composed, by definition, always of the same number of particles. Hence, the mass which is contained within the volume Υ, must be the same for any time. That can be expressed by

$$\frac{D}{Dt}\int\limits_{\Upsilon} \rho dV \equiv 0. \tag{2.3}$$

I.e. the mass of this element is conserved. Applying *Reynolds transport theorem*, one finds that

$$\int\limits_{\Upsilon} \left[\frac{D\rho}{Dt} + \rho(\nabla \cdot \mathbf{v}) \right] dV = 0, \tag{2.4}$$

and since the material volume can be regarded as arbitrary, the integral will only vanish if the integrand vanishes and hence,

$$\frac{D\rho}{Dt} + \rho(\nabla \cdot \mathbf{v}) = 0. \tag{2.5}$$

This is the equation of continuity in the Lagrangian frame. Using equation (2.2) gives the result in the Eulerian description,

$$\frac{\partial\rho}{\partial t} + \nabla(\rho\mathbf{v}) = 0. \tag{2.6}$$

If the flow would be independent of time (*steady flow*), then

$$\nabla(\rho\mathbf{v}) = 0. \tag{2.7}$$

2.1.3 Equation of Momentum

If one considers a material volume Υ, which is fully surrounded by the fluid, i.e. all surfaces lies entirely within the fluid, then all momenta generated by forces which act on the surfaces, have to be conserved (*conservation of linear momentum*). From this follows, that the change of the total momentum with time, has to equal the total force acting on the material element. This can be expressed as,

$$\frac{D}{Dt} \int\limits_{\Upsilon} \rho\mathbf{v} dV = \int\limits_{\Upsilon} \mathbf{f} dV + \int\limits_{\Sigma} \mathbf{t} dS. \tag{2.8}$$

The integral over the volume accounts for body forces $\mathbf{f}$ like gravity, and the integral over a surface Σ accounts for surface forces $\mathbf{t}$ like pressure. After some algebra one derives *Cauchy's equation of motion*,

$$\rho(D\mathbf{v}/Dt) = \mathbf{f} + \nabla \cdot \mathbf{T}. \tag{2.9}$$

No special assumptions about the physical mechanism producing the stress are made in deriving this equation. Due to this, it is more general than *Euler's equation of motion* which will be derived in the following. $\mathbf{T}$ in equation (2.9) is a second rank tensor, calls the *stress tensor.* It reduces to the pressure gradient $-\nabla p$ in case of an "ideal fluid". That means that no viscous forces (e.g. friction) are present in the fluid. However these viscous forces are very important in computing stellar atmospheres, but for the sake of simplicity they will be not regarded in deriving these equations of hydrodynamics. But one should keep in mind that these forces have to considered in realistic simulations. In the case of a radiating fluid, the pressure consists of both, gas- and radiation pressure. The latter is in most cases small in late-type stars, but becomes significant towards hotter stars or AGB stars. In the latter, the strong winds are driven by radiation pressure. For the ideal fluid one obtains *Euler's equation of motion*,

$$\rho(D\mathbf{v}/Dt) = \mathbf{f} - \nabla p, \tag{2.10}$$

which is the conservation of momentum in the Lagrangian frame. In the Eulerian frame equation (2.10) becomes,

$$\frac{\partial\rho\mathbf{v}}{\partial t} + \rho(\mathbf{v} \cdot \nabla)\mathbf{v} + \nabla p - \mathbf{f} = 0. \tag{2.11}$$

Hydrostatic Equilibrium

If one considers a static medium, where $\mathbf{v} = 0$ and also the acceleration $\mathbf{a} = 0$, equation (2.10) becomes,

$$\nabla p = \mathbf{f}. \tag{2.12}$$

That means, that the pressure stratification is determined by the acting body force, which is in general the gravitation $\mathbf{f} = -\rho \mathbf{g}$. $\mathbf{g}$ is the acceleration vector pointing in a certain direction. In an homogeneous plane parallel atmosphere $\mathbf{g} = (0, 0, -g)$ and hence equation (2.12) becomes

$$dp/dz = -\rho g. \tag{2.13}$$

The solution of equation (2.13) for an isothermal atmosphere is,

$$p = p_0 e^{-(z-z_0)/H}, \tag{2.14}$$

or if one solves for the density,

$$\rho = \rho_0 e^{-(z-z_0)/H}. \tag{2.15}$$

The *pressure scale height*,

$$H = -p\frac{dz}{dp} = -\frac{dz}{d\ln p}, \tag{2.16}$$

was introduced in equation (2.15). It describes the length scale over which the pressure changes locally, and is on the order of $\sim 100\,\mathrm{km}$ in the Sun's atmosphere and can be a few thousand kilometers in early-type stars, or a few tens of kilometers in late-type stars.

2.1.4 Equation of total Energy

The *conservation of energy* can be built up from the First Law of thermodynamics, which states:

> *The rate at which the energy E of a material element increases, must equal the rate at which heat Q is delivered to that element and the work W which is done against its surrounding,*

$$dE = dQ + dW. \tag{2.17}$$

In the context of hydrodynamics it goes beyond thermodynamics, and includes also gravitational and kinetic energy. It can be written as,

$$\frac{D}{Dt}\int_{\Upsilon} \rho(e + \frac{1}{2}v^2)dV = \int_{\Upsilon} \mathbf{f}\cdot\mathbf{v}dV + \int_{\Sigma} \mathbf{t}\cdot\mathbf{v}dS - \int_{\Sigma} \mathbf{q}\cdot d\mathbf{S}. \tag{2.18}$$

The left hand side term is the rate of change of the internal energy e plus kinetic energy of the material element. The first two terms on the right hand side represent the work which is done by external body forces and fluid stresses, respectively. The last term accounts for the rate of energy loss out of the fluid element which is caused by direct transport mechanisms like radiation. This is a heating rate Q_{rad}, described by the divergence of the flux, which is negative since it is directed outwards through the surface and the heat is lost from the volume element. After some algebra, equation (2.18) becomes for an ideal fluid,

$$\rho \frac{D(\epsilon_{ik})}{Dt} + \nabla \cdot (p\mathbf{v}) + Q_{rad} = \mathbf{f} \cdot \mathbf{v}. \tag{2.19}$$

This is the *total energy equation* in a Lagrangian description, where ϵ_{ik} stands for the sum of internal and kinetic energy. In the Eulerian description equation (2.19) becomes,

$$\frac{\partial(\rho\epsilon_{ik})}{\partial t} + \nabla \cdot [(\rho\epsilon_{ik} + p)\mathbf{v}] + \mathbf{f} \cdot \mathbf{v} - Q_{rad} = 0. \tag{2.20}$$

The derived equation accounts only for pure radiative hydrodynamics. If magnetic fields are also present, one has to include the magnetic energy. These situations can be described by equations of magneto-hydrodynamics (MHD) which is not treated in this work.

2.2 Radiative Transfer

The behaviour of a radiating medium can be described by a set of radiation terms and a description for the transport of the radiation. I will give an overview of the different quantities following the book of Gray (2008).

2.2.1 Specific Intensity

The specific intensity is one of the most basic quantities describing the radiation from a surface element. For a volume, filled with radiating gas, the specific intensity of a small area ΔA is defined as,

$$\begin{aligned} I_\nu &= \lim \frac{\Delta E_\nu}{\cos\theta\ \Delta A\ \Delta\omega\ \Delta t\ \Delta\nu} \\ &= \frac{dE_\nu}{\cos\theta\ dA\ d\omega\ dt\ d\nu}. \end{aligned} \tag{2.21}$$

In the limes, the finite quantities become infinitesimally small. In equation (2.21), $d\omega$ is the solid angle, $\cos\theta$ is the projection angle for the area dA, dt is the integrated time, and $d\nu$ defines the frequency range $[\nu, \nu + d\nu]$. dE_ν is the amount of energy emitted from the surface element.

2.2.2 Mean Intensity

The first moment of the intensity is defined as the mean intensity J_ν. It is the average over the angular direction,

$$J_\nu = \frac{1}{4\pi} \oint I_\nu d\omega. \tag{2.22}$$

The integration is performed over the whole unit sphere, with the considered point as center. The factor 4π results from the average.

2.2.3 Flux

The flux is the measure of the net energy flow across an area dA, over time dt, and spectral range $d\nu$ in the unit sphere $\cos\theta\ d\omega$. Integration of dE_ν over the whole unit sphere yields the total net energy that is needed to describe the same radiation in terms of the specific intensity.

$$F_\nu = \frac{\oint dE_\nu}{dA\ dt\ d\nu}. \tag{2.23}$$

The flux is related with the intensity via,

$$F_\nu = \oint I_\nu\ \cos\theta\ d\omega. \tag{2.24}$$

In general the flux is a three dimensional vector, but in the case of plane-parallel geometry, which is used in the following, it is reduced to one dimension.

2.2.4 Radiative Pressure

The second moment of the intensity is defined as the integral

$$K_\nu = \frac{1}{4\pi}\oint I_\nu\ \cos^2\theta\ d\omega. \tag{2.25}$$

This quantity K_ν can be identified with the pressure of the radiation. One considers the momentum which is transported by the photons to a solid wall per unit time and area.

$$dP_\nu = \frac{1}{c}\frac{dE_\nu\ \cos\theta}{dt\ dA}, \tag{2.26}$$

and this can also be related with the intensity through,

$$dP_\nu = \frac{I_\nu}{c}\cos^2\theta\ d\nu\ d\omega. \tag{2.27}$$

The total radiation pressure is then given by the integration of direction and frequency, which relates it with the second moment K_ν.

$$P_R = \frac{4\pi}{c}\int_o^\infty K_\nu\ d\nu. \tag{2.28}$$

In the three dimensional case, the radiation pressure would be a second rank tensor.

2.2.5 Optical Depth

If radiation passes trough a layer of non- or only weakly radiating material, then the beam of intensity will be weakened by this layer. The amount of radiation dI_ν which is absorbed on a path length dx, can be described with,

$$dI_\nu = -\kappa_\nu\ \rho\ I_\nu dx. \tag{2.29}$$

ρ is the density in mass per unit volume and κ_ν is the important *absorption coefficient*, with units of area per mass. In the absorption coefficient, two physical processes are considered:

i) true absorption, where an absorber (atom, molecule) is excited by the energy of the photon, which is consequently destroyed, and
ii) scattering, where the photon's direction and / or energy is changed and hence removed from the original radiation beam.
Since radiation is always confronted with a product of density and absorption coefficient over a path length L, the very useful concept of the optical depth τ_ν is appropriate to describe the absorption processes.

$$\tau_\nu = \int_0^L \kappa_\nu \, \rho \, dx, \tag{2.30}$$

where τ_ν is a unitless quantity. With the optical depth, equation (2.29) becomes,

$$dI_\nu = -I_\nu \, d\tau_\nu, \tag{2.31}$$

and has the solution

$$I_\nu = I_\nu^0 \, e^{-\tau_\nu}. \tag{2.32}$$

The latter is a common extinction law with I_ν^0 as the original intensity which will be weakened on its way through the material. It is obvious that, if $\tau_\nu \ll 1$, then radiation can easily and one speaks of an *optically thin* layer. If $\tau_\nu \gg 1$, then almost all radiation is absorbed and the layer is referred to as being *optically thick*.

2.2.6 Source Function

In the case of a radiating layer, the intensity will be enhanced by a certain amount which is given by,

$$dI_\nu = j_\nu \rho \, dx. \tag{2.33}$$

Here, j_ν is the *emission coefficient* with units of erg/(s rad^{2}Hz g). Again, two physical processes contribute two the emission coefficient:
i) real emission, where a photon is created, and
ii) photons which were scattered in the considered direction.

Because, the ratio of emission and absorption has the same unit as the intensity, it can be can thought of as the intensity emitted in a hot gas at some point. This ratio is also known as the *source function* and is defined as,

$$S_\nu = j_\nu / \kappa_\nu. \tag{2.34}$$

There are two extreme cases where the source function can be computed easily:
i) pure isotropic scattering where

$$S_\nu = J_\nu, \tag{2.35}$$

and
ii) pure absorption (which leads to the case of strict LTE in the next section), where the source function can be identified with the Planck function,

$$S_\nu = \frac{2h\nu^3}{c^2} \frac{1}{e^{h\nu/kT} - 1}. \tag{2.36}$$

In this case, the source function S_ν of the *Black Body* radiation is often denoted as B_ν.

2.2.7 Stefan-Boltzmann Law

It is very convenient and useful to regard parts of stellar atmospheres as a radiating black body. One assumes that a thin layer is isotropic and isothermal and in thermal equilibrium with incoming and outgoing radiation of its surroundings. This approximation is called "*Local Thermodynamic Equilibrium*" (LTE) and is a powerful assumption simplifying when considering stellar atmospheres. One can imagine an atmosphere constructed of several thin layers which are all for themselves in local thermodynamic equilibrium. For the physical description it is helpful to introduce the concept of Einstein Coefficients.

Consider the spontaneous emission in a two level atom between upper and lower level (u and l respectively) which is separated by the transition energy h/nu and assume the emission to be isotropic. In such a system, the probability that the atom emit a photon with energy $h\nu$ within a time dt is $A_{ul} dt d\omega$, with A_{ul} as the Einstein coefficient for spontaneous emission. The rate of emission of N_u excited atoms is then,

$$\frac{dN_u}{dt} = -A_{ul} N_u. \tag{2.37}$$

If a radiation field is present, emission by an excited atom can also be induced by this field. This process depends up on the intensity, so the probability is $B_{ul} I_\nu dt$. The rate of this stimulated emission is given by,

$$\frac{dN_u}{dt} = -B_{ul} I_\nu N_u. \tag{2.38}$$

Here, B_{ul} is the Einstein coefficient for stimulated emission. The probability for absorption is defined in the same way and is $B_{lu} I_\nu dt$ with B_{lu} as the Einstein coefficient for absorption. The rate is,

$$\frac{dN_u}{dt} = B_{lu} I_\nu N_l, \tag{2.39}$$

with N_l as the number of atoms in the lower state.

If the system is in thermal equilibrium, the rates of population and depopulation of the excited state by absorption and emission respectively must balance each other (*detailed balance*). Thus,

$$N_l B_{lu} I_\nu = A_{ul} N_u + B_{ul} I_\nu N_u. \tag{2.40}$$

The upper and lower levels of an atom are populated following the Boltzmann law,

$$\frac{N_u}{N_l} = \frac{g_u}{g_l} e^{-h\nu/kT}, \tag{2.41}$$

and the radiation through a thin atmospheric layer in LTE can be described by equation (2.40). Solving equation (2.40) for I_ν and use equation (2.41) gives

$$I_\nu = \frac{A_{ul}}{(g_l/g_u) B_{lu} e^{h\nu/kT} - B_{ul}}. \tag{2.42}$$

This expression must become the expression for the Rayleigh-Jeans approximation for small ν ($I = \frac{2kT\nu^2}{c^2}$) and this is only possible if

$$B_{ul} = \frac{g_l}{g_u} B_{lu} \qquad \text{and} \qquad A_{ul} = \frac{2h\nu^3}{c^2} B_{ul}, \tag{2.43}$$

where g_u and g_l are upper and lower statistical weights, respectively. With the use of equation (2.43), equation (2.42) becomes,

$$I_\nu = \frac{2h\nu^3}{c^2} \frac{1}{e^{h\nu/kT} - 1}. \tag{2.44}$$

In order to derive the flux, one integrates equation (2.24) with equation (2.44) over frequency.

$$F = \int\limits_0^\infty F_\nu \, d\nu = \frac{2\pi^2 k^4}{15 h^3 c^2} T^4 = \sigma T^4, \tag{2.45}$$

where σ is the Stefan-Boltzmann radiation constant. With equation (2.45), the radiative pressure P_R becomes,

$$P_R = \frac{4\sigma}{3c} T^4. \tag{2.46}$$

2.2.8 Radiative Transfer Equation

The net amount of radiation through a layer in plane parallel geometry with path length ds is given by the sum of absorption and emission,

$$dI_\nu = -\kappa_\nu \, \rho \, I_\nu \, ds + j_\nu \, \rho \, ds. \tag{2.47}$$

This can be written under the use of the optical depth and the definition of the source function as,

$$\frac{dI_\nu}{d\tau_\nu} = -I_\nu + S_\nu. \tag{2.48}$$

If the beam is considered under a certain angle θ, then equation (2.48) becomes

$$\mu \, \frac{dI_\nu}{d\tau_\nu} = -I_\nu + S_\nu, \tag{2.49}$$

with $\mu = \cos\theta$ and τ measured in vertical direction. The solution of this differential equation of radiative transfer can be split in an outward directed part with intensity I_ν^{out} and an inward directed parts with intensity I_ν^{in},

$$\begin{aligned} I_\nu(\tau_\nu) &= I_\nu^{out}(\tau_\nu) + I_\nu^{in}(\tau_\nu) \\ &= \int\limits_{\tau_\nu}^\infty S_\nu(\tau_\nu) e^{-(\tau_\nu - t_\nu)/\mu} \, dt_\nu/\mu \\ &- \int\limits_0^{\tau_\nu} S_\nu(\tau_\nu) e^{-(\tau_\nu - t_\nu)/\mu} \, dt_\nu/\mu. \end{aligned} \tag{2.50}$$

In LTE, the source function S_ν is given by the Planck function B_ν. In the case of the stellar surface, equation (2.50) becomes,

$$\begin{aligned} I_\nu^{in}(0) &= 0 \\ I_\nu^{out}(0) &= \int\limits_0^\infty S_\nu(\tau_\nu) e^{-(\tau_\nu - t_\nu)/\mu} \, dt_\nu/\mu. \end{aligned} \tag{2.51}$$

2.2.9 Radiative Equilibrium

Radiative equilibrium can express the conservation of energy (but is not essentially needed to conserve the energy). It states, that inside a stellar atmosphere no sinks or sources where energy is lost or generated are present. That means, that the divergence of the flux must be zero everywhere in the photosphere. In plane parallel geometry, the divergence condition is,

$$\frac{d}{dx}F(x) = 0 \qquad \text{or} \qquad F(x) = F_0. \tag{2.52}$$

That means that the total flux F_0 must be independent of depth, which is the first condition for radiative equilibrium. If also convective energy transport, in form of convective flux $\Phi(x)$, is included, then the total flux is given by,

$$F(x) = \Phi(x) + \int\limits_0^\infty F_\nu(x)\ d\nu. \tag{2.53}$$

Another condition for radiative equilibrium stems from the transfer equation (2.49) in the form of,

$$\mu\ \frac{dI_\nu}{dx} = \kappa_\nu\ \rho\ I_\nu - \kappa_\nu\ \rho\ S_\nu. \tag{2.54}$$

Integration over solid angle and frequency also expressions for flux and mean intensity give,

$$Q_{rad} = -\frac{d}{dx}\int\limits_0^\infty F_\nu(x)\ d\nu = -4\pi\ \rho \int\limits_0^\infty \kappa_\nu\ (J_\nu - S_\nu)\ d\nu. \tag{2.55}$$

This describes the radiative heating rate Q_{rad}, which is zero in the case of radiative equilibrium. Q_{rad} is very important in the treatment of radiation hydrodynamics, since there the condition of radiative equilibrium is not fulfilled and Q_{rad} enters the total energy conservation (see Section 2.1.4).

2.3 Equation of State

In order to close the system of equations for radiation hydrodynamics, one needs relations between the pressure P, temperature T, and density ρ. They are given by the thermodynamical properties of the matter in form of an *equation of state*. A simple approximation is to describe the stellar matter as a combination of an ideal gas and radiation. In this approximation, the specific inner energy and the pressure can be described with,

$$P = \frac{R}{\mu}\rho\ T + \frac{4\sigma}{3c}T^4 \tag{2.56}$$

$$e = \frac{3}{2}\frac{R}{\mu}T + \frac{4\sigma}{c\ \rho}T^4 + E_{ion}. \tag{2.57}$$

R is the ideal gas constant and μ the mean molecular weight, which depends on the ionisation state of the matter. E_{ion} also includes the influence of ionisation and recombination of the different elements. μ and E_{ion} can be determined under the assumption of statistical equilibrium with the Saha-Boltzmann equation.

2.4 Convection

As remarked in section 2.2.9, convection can play a significant role in energy transport. Solar-type stars exhibit a convectively unstable envelope and become fully convective towards late spectral types (around M3 to M4 or masses $< 0.25M_{\odot}$). For a better understanding under what conditions convection sets in, one can assume a hydrostatic atmosphere. I will briefly explain the convective mechanism following Kippenhahn (1990) and Gray (2008).

Convection sets in if the temperature gradient is not lowered sufficiently enough by radiative energy transport, i.e. diffusion. In this case, a rising volume element can poss an excess of heat in comparison to its surroundings. This element can transport the energy outwards, if it is optically thick to prevent radiative energy loss to the surroundings.

The convective flux Φ can be described by

$$\Phi = \rho C_p v \Delta T, \tag{2.58}$$

where ρ is the density of the volume element, C_p is the specific heat at constant pressure, v is the upward velocity, and ΔT is the temperature difference between the element and its surroundings.

For convection, three main conditions are required to occur: a gravitational field; horizontal density fluctuations; and roughly hydrostatic conditions. A density fluctuation can be achieved if a mass element is for some reason hotter than its surroundings. In this case, this element expands and the difference of pressure inside the mass element and the surroundings will equalize with the local velocity of sound c_S, which is usually faster than other motions of the element. Due to this, one can describe this as an adiabatic expansion. This means that the density decreases with increasing volume and the element starts to rise upwards due to the force of buoyancy. The question is now, if the density will be stay lower while the element passes higher, less dense, layers, or in other words if the stratification is convectively stable or not. It will be unstable if the density of the element decreases as rapidly (or even faster) as the average density of its surroundings. That can be expressed by,

$$\frac{1}{\Gamma_1} = \left(\frac{d\log\rho}{d\log p}\right)_e > \left(\frac{d\log\rho}{d\log p}\right)_s . \tag{2.59}$$

Here, $\Gamma_1 = \frac{d\log p}{d\log\rho}|_{S=const.}$ is the first adiabatic exponent and e and s indicate the mass element and its surrounding, respectively and capital S is the entropy which must be constant. With an equation of state $\rho = \rho(p, T, \mu)$, where μ is the molecular weight, dependent on the chemical composition, one can express equation (2.59) as

$$\nabla > \nabla_e + \frac{\phi}{\delta}\nabla_\mu . \tag{2.60}$$

Here the definitions,

$$\nabla := \frac{d\log T}{d\log p}|_{s,\mu}, \quad \nabla_e := \frac{d\log T}{d\log p}|_{e,\mu}, \quad \nabla_\mu := \frac{d\log\mu}{d\log p}|_{s,T} \tag{2.61}$$

and,

$$\delta := \frac{d\log\rho}{d\log T}|_{p,\mu}, \quad \phi := \frac{d\log\rho}{d\log\mu}|_{p,T}, \tag{2.62}$$

are used. The subscripts indicate where the derivative with respect to pressure is taken and which quantity is kept constant. In the adiabatic case, $\nabla_e = \nabla_{ad}$. If the energy is exclusively transported by radiation, then the actual temperature gradient ∇ is equal to the radiative temperature gradient ∇_{rad}. In this case, the stratification becomes unstable if

$$\nabla_{rad} > \nabla_{ad} + \frac{\phi}{\delta}\nabla_{\mu}. \tag{2.63}$$

This is known as the *Ledoux criterion.* The *Schwarzschild criterion* is obtained if the chemical composition is homogeneous over the convective region $\nabla_{\mu} = 0$. Then

$$\nabla_{rad} > \nabla_{ad}, \tag{2.64}$$

if the stratification is unstable. Since convection mixes the chemical stratification, ∇_{μ} becomes zero after some time convection sets in. A more general expression for the stability criterion is derived using the entropy S. It is stable if

$$\frac{dS}{dr} > 0, \tag{2.65}$$

and unstable otherwise.

The energy transport by convection can be described in 1D atmosphere models by the use of the *Mixing-Length-Theory*, derived by Böhm-Vitense (1958). In 3D modeling of stellar atmospheres, convection results in a natural way from the equations of radiation-hydrodynamics.

Chapter 3

Atmosphere and Line Formation Codes

3.1 `CO5BOLD` Atmosphere Code

`CO5BOLD` is the abbreviation for "COnservative COde for the COmputation of COmpressible COnvection in a BOx of L Dimensions with L=2,3" (Freytag et al., 2008). It can be used to model solar and stellar surface convection. In solar-like stars, a `CO5BOLD` model represents the 3D flow geometry and its temporal evolution in a small (relative to the star's radius) Cartesian domain at the stellar surface ("box in a star" set-up). The spatial size of the domain is chosen to be sufficient to include the dominant convective scales, i.e. the computational box is large enough to include a number of granular cells at any instant in time. A `CO5BOLD` model provides a statistical realization of the convective flow. In the following work, I usually average over five flow fields taken at different instances in time ("snapshots") to improve the statistics.

`CO5BOLD` solves the coupled non-linear time-dependent equations of compressible hydrodynamics coupled to the radiative transfer equation in an external gravitational field in 3 spatial dimensions. As set of independent quantities are chosen the mass density ρ, the three spatial velocities v_x, v_y, and v_z, and the internal energy ϵ_i. With these quantities, the 3D hydrodynamics equations, including source terms due to gravity, are the mass conservation equation

$$\frac{\partial\rho}{\partial t}+\frac{\partial\rho v_x}{\partial x}+\frac{\partial\rho v_y}{\partial y}+\frac{\partial\rho v_z}{\partial z}=0, \tag{3.1}$$

the momentum equation

$$\frac{\partial}{\partial t}\begin{pmatrix}\rho v_x\\ \rho v_y\\ \rho v_z\end{pmatrix}+\frac{\partial}{\partial x}\begin{pmatrix}\rho v_x v_x+P\\ \rho v_y v_x\\ \rho v_z v_x\end{pmatrix}+\frac{\partial}{\partial y}\begin{pmatrix}\rho v_x v_y\\ \rho v_y v_y+P\\ \rho v_z v_y\end{pmatrix}+\frac{\partial}{\partial z}\begin{pmatrix}\rho v_x v_z\\ \rho v_y v_z\\ \rho v_z v_z+P\end{pmatrix}=\begin{pmatrix}\rho g_x\\ \rho g_y\\ \rho g_z\end{pmatrix}, \tag{3.2}$$

and the energy equation which includes the radiative heating term Q_{rad}

$$\frac{\partial\rho\epsilon_{ik}}{\partial t}+\frac{\partial(\rho\epsilon_{ik}+P)v_x}{\partial x}+\frac{\partial(\rho\epsilon_{ik}+P)v_y}{\partial y}+\frac{\partial(\rho\epsilon_{ik}+P)v_z}{\partial z}=\rho(g_x v_x+g_y v_y+g_z v_z)+Q_{rad}. \tag{3.3}$$

ϵ_{ik} denotes the sum of specific internal and kinetic energy. The gas pressure P is related to the density ρ and internal energy ϵ_i via a (tabulated) equation of state $P=P(\rho,\epsilon_i)$. For the local models used here the gravity field is given by the constant vector $\vec{g}=(0,0,-g)$. (`CO5BOLD` uses the convention that the vertical axis points upwards.) The radiative heating term Q_{rad} is obtained from the solution of the non-local frequency-dependent radiative transfer equation. The frequency dependence of the radiation field is captured by considering a small number of representative wavelength bands ("opacity binning", see Ludwig et al., 2002, 2006). The resulting 3D radiative-hydrodynamic (RHD) models treat convection from basic physical principles and avoid approximations like mixing-length theory.

3.2 `MARCS` and `PHOENIX` Atmospheres

`MARCS`[1] (Gustafsson et al., 2008) and `PHOENIX`[2] (Hauschildt & Baron, 1999) are both numerical codes, which compute static, self consistent, one dimensional stellar atmospheres in plane parallel or spherical geometry. Both use the *opacity sampling method* in which the opacity for each wavelength is computed individually. Both include line data for a large number of known atomic species and available molecules. They are able to compute atmospheres of early type stars down to late type stars for a variety of surface gravities (from dwarfs to giants). `MARCS` model atmospheres reach down to 2500 K, the `PHOENIX` models go even lower in the region where dust formation becomes significant which can be handled. `PHOENIX` also describes atmospheres of extra solar giant planets.

The `MARCS` atmosphere models are available for download on the `MARCS` homepage (see footnote above) and the `Phoenix` models can be downloaded for example from the `PHOENIX` web simulater homepage [3] (NextGen, AMES-Cond, and AMES-Dusty models, BT... .).

3.3 Line Formation Code `LINFOR3D`

`LINFOR3D`[4] is a line formation code, which is in principle based on Baschek et al. (1966) but is strongly revised to match up to date theory. It is able to perform the spectral synthesis on the 3 dimensional `CO`^{5}`BOLD` models in local thermodynamic equilibrium. It calculates the specific intensity for a given number of horizontal positions, under a given number of solid angles. This is then integrated to compute the flux. It takes also the velocity of each *voxel* (volume pixel) into account and determines the resulting frequency shift. In this way, the spectral line will be broadened by the actual velocity field in the hydrodynamical model and no additional assumptions like the spectroscopic quantities micro- and macro-turbulence velocities are needed.

The code is also be able to perform line synthesis on 1 dimensional *reference* model atmospheres. These can be averaged 3D models (which will be called ⟨3D⟩-models, see Sect. 6.1.1 for a detailed description), or 1D models like `MARCS` or `Phoenix` atmospheres. This gives the opportunity to investigate the influence of three dimensional effects using comparisons between spectral line synthesis performed on 1D and 3D atmosphere models.

The `LINFOR3D` code can automatically compute the equivalent width of a spectral line,

$$W_\lambda = \int\limits_{\lambda_1}^{\lambda_2} \left(\frac{F_c - F_\lambda}{F_c} \right) d\lambda, \tag{3.4}$$

---

[1] `http://marcs.astro.uu.se/`

[2] `http://www.hs.uni-hamburg.de/EN/For/ThA/phoenix/index.html`

[3] `http://phoenix.ens-lyon.fr/simulator/index.faces`

[4] see `http://www.aip.de/~mst/Linfor3D/linfor_3D_manual.pdf`

where F_c is the continuum flux, and F_λ the flux of the line in the range of $[\lambda_1, \lambda_2]$. The latter should in principle extent over the whole region where the contribution of the whole absorption is not zero. One can also generate a sequence of ⟨3D⟩-lines with varying micro-turbulence velocities and produce a *curve of growth* (described in more detail in Sect. 6.2.3), which is helpful to determine micro-turbulence velocities in the 3D models or to derive abundance corrections due to hydrodynamical velocity fields.

In order to investigate the height of formation for the synthesized lines, `LINFOR3D` computes contribution functions after the description of Magain (1986). They are very helpful in order to decide if the formation region of the line is fully covered from integration of intensity over the atmospheric model and to decide in which region the maximal line contribution stems from. In general the code performs the line synthesis over a region ranging from $\log_{10} \tau_{max} = 2$ up to $\log_{10} \tau_{min} = -6$ but these borders can be adjusted if necessary.

`LINFOR3D` is able to perform single line calculation, as well as multi line calculations. In the latter case, the total line opacity for each wavelength point is calculated. In this way, the code accounts for line blends. As input data, one needs a *linefile*, which includes values for the species, lower level energy, wavelength, oscillator strength ($\log gf$), and van der Waals broadening constant. Optionally one can use also values for Stark and natural broadening which otherwise will be calculated internally.

3.4 Line Formation Code `SYNTH3` (`SYNMAST`)

The `SYNTH3`[5] (Kochukhov, 2007) code is a very fast spectrum synthesis code, designed for plane-parallel one dimensional stellar atmospheres ranging from early B- to late M-type stars. The input atmospheres have to be in “krz” format, which is equal to the ”mod” format by Kurucz. As input data for the code, one has to use the VALD[6] line list format. The `SYNMAST` code is basically the `SYNTH3` code, but is also able to compute Zeeman splitting for spectral lines.

---

[5] `http://www.astro.uu.se/~oleg/files/synth3/synth3.pdf`

[6] `http://vald.astro.univie.ac.at/~vald/php/vald.php`

Chapter 4

Spectroscopy of Diatomic Molecules

In order to treat the spectra of molecules, it is necessary to solve the Hamiltonian for the system of participating atoms and electrons. Since this is impossible in fully analytical form, the usage of the *Born-Oppenheimer-Approximation* is of great advantage. Within this approximation, one is able to describe the observed spectra in a satisfying way. The 'trick' is to separates the electronic and nuclear motion in the center of mass system. Then, one computes first the electron configuration for a fixed positions in the center of mass system of the participating atoms of the molecule, and then one can calculate the motion of the nuclei, which are rotation and vibration. I will give a basic picture of the theoretical background which is needed to understand the observed spectra. For this I will us the descriptions of Fliessbach (2000) and Bernath (2005).

4.1 General Treatment of Diatomic Molecules

The Hamiltonian of a diatomic molecule in the center of mass system is given by

$$H = \sum_{k=1}^{2} \frac{-\hbar^2}{2M_k} \mathit{\Delta}_k + \frac{Z^2 e^2}{|\mathbf{R}_1 - \mathbf{R}_2|} + H_{el}, \tag{4.1}$$

where $\mathit{\Delta}_k$ is the Laplace operator, $\mathbf{R_k}$ is the position of both nuclei, M_k their mass, e is the elementary charge and Z is the valence number. H_{el} is the Hamiltonian of the electrons, which is, in general,

$$H_{el} = \sum_{\nu=1}^{N} \frac{-\hbar^2}{2m_e} \mathit{\Delta}_\nu + \sum_{\nu=2}^{N} \sum_{\mu=1}^{\nu-1} \frac{e^2}{|\mathbf{r}_\nu - \mathbf{r}_\mu|} - \sum_{\nu=1}^{N} \sum_{k=1}^{2} \frac{Ze^2}{|\mathbf{r}_\nu - \mathbf{R}_k|}, \tag{4.2}$$

with N number of electrons and r_ν as their position. To solve H one uses a product of wave functions

$$\mathit{\Psi}(\mathbf{r}_1, ..., \mathbf{r}_N, \mathbf{R}_1, \mathbf{R}_2) = \mathit{\Psi}_K(\mathbf{R}_1, \mathbf{R}_2) \cdot \mathit{\Psi}_{el,\mathbf{R}_k}(\mathbf{r}_1, ..., \mathbf{r}_2). \tag{4.3}$$

What is left now, is a wave function for the electrons $\mathit{\Psi}_{el,\mathbf{R}_k}$ for fixed coordinates of the nuclei and a wave function for the nuclei $\mathit{\Psi}_K$, which can be further factorized into vibrational $\mathit{\Psi}_v$ and rotational $\mathit{\Psi}_r$ contributions. This yields the total energy of the molecule is the sum of the contributions from the electrons, vibrations and rotation.

$$E_{total} = E_{el} + E_v + E_r. \tag{4.4}$$

The excitation energies for the different transitions are about $\sim 0.01\,\text{eV}$ for rotational transitions, $\sim 0.1\,\text{eV}$ for vibrational transitions, and $\sim 3\,\text{eV}$ for electronic transitions. The next step is to construct a Hamiltonian from which one can determine the energies for the different transitions.

One uses equation (4.1) with Ψ so that

$$H\Psi = H\Psi_K\Psi_{el,\mathbf{R}_k} = \left(\sum_{k=1}^{2}\frac{-\hbar^2}{2M_k}\Delta_k + \frac{Z^2e^2}{|\mathbf{R}_1-\mathbf{R}_2|} + E_{el}(\mathbf{R})\right)\Psi_K\Psi_{el,\mathbf{R}_k}, \tag{4.5}$$

where it was implicitly used, that

$$H_{el}\Psi_{el,\mathbf{R}_k}(\mathbf{r}_1,...,\mathbf{r}_2) = E_{el}(\mathbf{R})\Psi_{el,\mathbf{R}_k}(\mathbf{r}_1,...,\mathbf{r}_2). \tag{4.6}$$

Then $H\Psi = E\Psi$ is reduced to $H_K\Psi_K = E\Psi_K$ and one can write H_K in coordinates of the relative motion and center of mass system,

$$\mathbf{R} = \mathbf{R}_1 - \mathbf{R}_2, \qquad \mathbf{R}_{cm} = \frac{\mathbf{R}_1+\mathbf{R}_2}{2}, \tag{4.7}$$

as

$$H_K = -\frac{\hbar^2}{2M_{cm}}\Delta_{\mathbf{R}_{cm}} - \frac{\hbar^2}{2\mu}\Delta_{\mathbf{R}} + \frac{Z^2e^2}{\mathbf{R}} + E_{el}(\mathbf{R}). \tag{4.8}$$

The reduced mass $\mu = \frac{M_1+M_2}{2}$ is introduced as well as the total mass $M_{cm} = M_1 + M_2$. Since H_K commutes with the operator $\mathbf{P}_{cm} = -i\hbar\nabla_{cm}$ of the center of mass momentum, a wave function Ψ_K as an Eigenfunction of P_{cm} can be found. This can again be factorized in a part for the relative motion and one for the translative motion in the center of mass system.

$$\Psi_K = \exp(i\mathbf{K}\cdot\mathbf{R_{cm}})\Phi_{rel}(\mathbf{R}) = \Phi_{cm}\Phi_{rel}, \tag{4.9}$$

with $\mathbf{K}$ as the wave vector. Now, $H_K\Psi_K = E\Psi_K$ is reduced to $H_K'\Phi_{rel} = E'\Phi_{rel}$ with

$$H_K' = -\frac{\hbar^2}{2\mu}\Delta_{\mathbf{R}} + \frac{Z^2e^2}{\mathbf{R}} + E_{el}(\mathbf{R}) - E_{el}(\infty) = -\frac{\hbar^2}{2\mu}\Delta_{\mathbf{R}} + V(\mathbf{R}). \tag{4.10}$$

The zero point energy is shifted using $E' = E - \hbar^2\mathbf{K}^2/2M_{cm} - E_{el}(\infty)$, to include the translation energy in this term. The contribution from the electrons and the coulomb forces from the repulsing nuclei are combined into the potential $V(\mathbf{R})$. This potential depends on the solution of the electron system and is different for each electronic transition. H_K' also commutes with the angular momentum operator $\mathbf{l} = \mathbf{r}\ x\ \mathbf{p}$ which makes it convenient to express the angular part of Φ_{rel} in the spherical harmonics $Y_{LM}(\theta,\phi)$,

$$\Psi_K = \Phi_{cm}\Phi_L(R)Y_{LM}(\theta,\phi). \tag{4.11}$$

The Laplace operator Δ can be expressed in spherical coordinates which introduces the angular momentum operator in spherical coordinates for which the Eigenvalues of the spherical harmonics are well known. This leads to,

$$H_K' = -\frac{\hbar^2}{2\mu}\left(\frac{\partial^2}{\partial R^2} + \frac{2}{R}\frac{\partial}{\partial R}\right) + \frac{\hbar^2L(L+1)}{2\mu R^2} + V(R). \tag{4.12}$$

The potential $V(R)$ can be approximated with a Taylor series to second order,

$$V(R) = \frac{Z^2e^2}{\mathbf{R}} + E_{el}(\mathbf{R}) - E_{el}(\infty) \approx V(R_0) + \frac{\mu\omega^2}{2}(R-R_0)^2, \tag{4.13}$$

where ω is dependent on the electronic transition. The zero order term is the energy for the electrons at R_0 and the second term is the potential for the harmonic oscillator. This approximation is valid for small deviations from the equilibrium position, but breaks down for larger deviations. A more realistic potential is for example the *Morse* potential which is described in more detail in section 4.3.1. A comparison between both is shown in Fig. 4.1. If a radial function $U(R) = R\Phi_L(R)$ is used, then

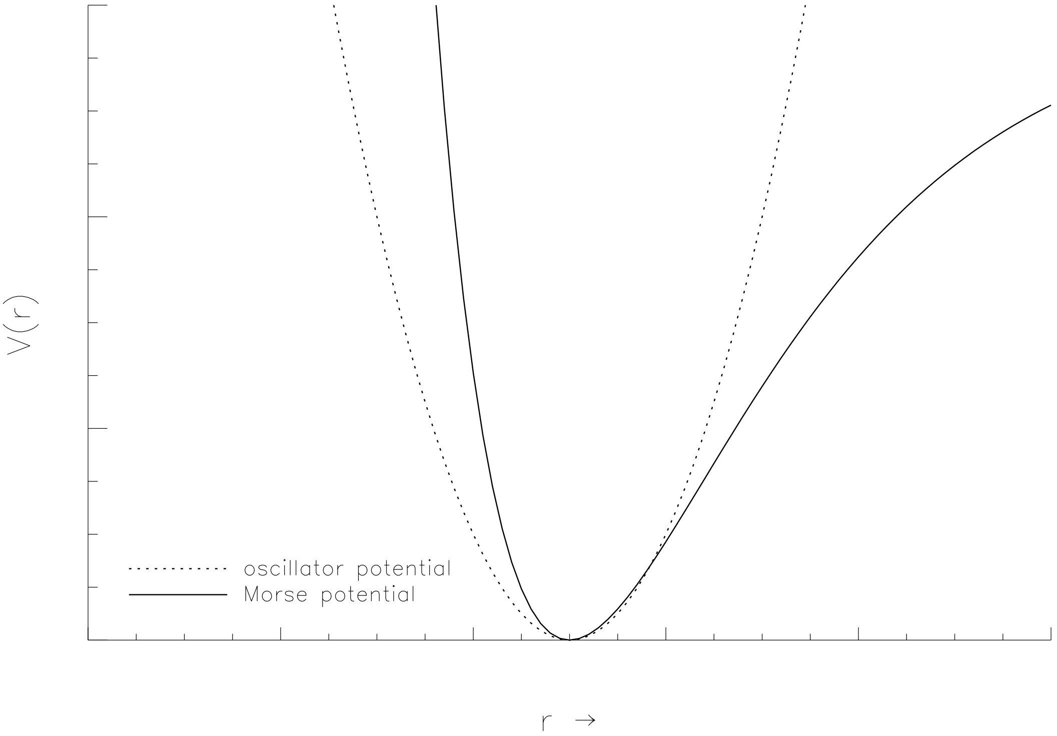

Figure 4.1: Comparison between Morse and harmonic oscillator potential.

$$\left(\frac{\partial^2}{\partial R^2} + \frac{2}{R}\frac{\partial}{\partial R}\right)\Phi_L(R) = \left(\frac{\partial^2}{\partial R^2} + \frac{2}{R}\frac{\partial}{\partial R}\right)\frac{U(R)}{R} = \frac{U''(R)}{R} \tag{4.14}$$

and the Hamiltonian looks like

$$H'_K = -\frac{\hbar^2}{2\mu}\frac{d^2}{dR^2} + \frac{\mu\omega^2}{2}(R-R_0)^2 + \frac{\hbar^2 L(L+1)}{2\mu R_0^2} + V(R_0) \tag{4.15}$$

Now equation (4.15) can be applied on equation (4.11) and $\Phi_L(R)$ the Hermitian polynomials are used, which are the solution for the harmonic oscillator. The energy E' will be

$$E' = E_{el} + \hbar\omega\left(n + \frac{1}{2}\right) + B_e L(L+1) \tag{4.16}$$

with $B_e = \frac{\hbar^2}{2\mu R_0^2}$ as the rotational constant. This is the energy for a molecular system which vibrates and rotates for a specific electronic transition. In the following sections, I will describe the energy levels in more detail.

4.2 Rotational Spectroscopy

4.2.1 Selection Rules

In equation (4.16), the energy $F(J)$ for the rotating molecule is given by

$$F(J) = BJ(J+1) + \nu_0, \tag{4.17}$$

where J is used instead of L for the rotational quantum number and ν_0 is added for sum of vibrational and electronic energy. I will now follow Bernath (2005) and determine the intensities for the pure rotational transitions which are dependent on the selection rules for the transitions. This is governed by the transition dipole moment

$$\mathbf{M} = \int Y^*_{J'M'} \mu Y_{J''M''} d\tau = \langle J'M'|\mu|J''M''\rangle, \tag{4.18}$$

with $d\tau = \sin\theta d\theta d\phi$ The spherical harmonics for a linear molecule can be written as

$$Y_{JM}(\theta,\phi) = \varTheta_{JM}(\theta)e^{iM\phi}/\sqrt{2\pi}. \tag{4.19}$$

For a diatomic molecule, the dipole moment is oriented along the internuclear axis, and one can express its components in laboratory axis system as

$$\mu = \mu_x \hat{\mathbf{e_1}} + \mu_y \hat{\mathbf{e_2}} + \mu_z \hat{\mathbf{e_3}} \quad = \mu_0(\sin\theta\cos\phi\hat{\mathbf{e_1}} + \sin\theta\sin\phi\hat{\mathbf{e_2}} + \cos\theta\hat{\mathbf{e_3}}). \tag{4.20}$$

If one also uses the relationships $\cos\phi = (e^{i\phi} + e^{-i\phi})$ and $\sin\phi = (e^{i\phi} - e^{-i\phi})$ and the recursion formula for the Legendre polynomials in the spherical harmonics, then

$$(2l+1)zP^m_l(z) = (l+m)P^m_{l-1}(z) + (l-m+1)P^m_{l+1}(z), \tag{4.21}$$

where $z = \cos\theta$, then $\varTheta_{JM} = NP^m_l \cos\theta$. Inserting in equation (4.18) and solving gives the selection rules

$$\varDelta M \quad = 0, \pm 1 \tag{4.22}$$

$$\varDelta J \quad = \pm 1. \tag{4.23}$$

From equation (4.20) one can see that if $\mu_0 = 0$, no transition is allowed, i.e. symmetric molecules have no pure rotational transitions. If additional vibrational or electronic transitions are present, then $\varDelta J = 0, \pm 1$ (except for $J = 0$). The rotational transitions with $\varDelta J = -1$ are called R-branch, with $\varDelta J = 0$ Q-branch, and $\varDelta J = 1$ are called P-branch. The transition frequencies for the three cases of rotational transitions, which take place on a vibrational or electronic transition with frequency ν_0, look in case of absorption like

$$\nu(R) \quad = F(J') - F(J'') \quad = \nu_0 + 2B' + (3B' - B'')J + (B' - B'')J^2 \tag{4.24}$$

$$\nu(Q) \quad = F(J') - F(J'') \quad = \nu_0 + (B' - B'')J + (B' - B'')J^2 \tag{4.25}$$

$$\nu(P) \quad = F(J') - F(J'') \quad = \nu_0 - (B' + B'')J + (B' - B'')J^2 \tag{4.26}$$

The upper states are indicated by primes (J') and the lower states with double primes (J''). Customarily, one writes the upper state first since the convention stems from emission spectroscopy. One can see in equation (4.25), that only for transition between vibrational states or electronic states, a Q-branch appears. For pure rotationally transitions, the transition energy of the Q-branch is zero. It would also be a transition into an identical state, which is forbidden due to Pauli's exclusion principle. For pure rotational transitions ($B'' = B'$) and the P- and R-branches show equally spaced transitions with distances of $2B'$.

4.2.2 Intensities

The intensity of a rotational transition for a spectral molecular absorption line is determined by the transition dipole moment and the population difference between the two levels (or ratio using the Boltzmann relation below). The latter is given by Boltzmann statistics. The transition dipole moment, which enters the Einstein A coefficient, is given by the solution of equation (4.18) for all three spatial directions

$$|\mathbf{M}|^2_{J''+1\leftarrow J'',M} = \sum_{M'} M_x^2 + M_y^2 + M_z^2 = \mu_0^2(J''+1). \tag{4.27}$$

This is the solution for absorption, but it is the same expression in the case of emission. The Einstein A values then becomes,

$$A = \frac{16\pi^3\nu^3\mu_0^2(J''+1)}{3\epsilon_0 hc^3(2J'+1)}, \tag{4.28}$$

which can be translated to the absorption cross section

$$\sigma = \frac{2\pi^2\nu\mu_0^2(J''+1)}{3\epsilon_0 hc(2J''+1)}. \tag{4.29}$$

The intensity is then described in a simple way by Beer's law, where stimulated emission is included

$$I = I_0 e^{-\sigma\left(N_0 - N_1\frac{2J''+1}{2J'+1}\right)l} = I_0 e^{-\alpha l}. \tag{4.30}$$

The absorption coefficient α was introduced. One can replace N_0 and N_1 by the total concentration N using the Boltzmann relation for N_1

$$\frac{N_1}{N_0} = \frac{2J'+1}{2J''+1}e^{-h\nu_{10}/kT}, \tag{4.31}$$

with ν_{10} as the transition frequency between the upper and lower state. For N_0, a relationship from statistical thermodynamics is used.

$$N_0 = \frac{N(2J''+1)e^{-E_0/kT}}{q_{rot}}, \tag{4.32}$$

where E_0 is the lower level energy, given by equation (4.17) and q_{rot} is the rotational partition function. In cases where also vibrational or electronic transitions are present, the partition function becomes $q = q_{el}q_{vib}q_{rot}$ and also the statistical weights of vibrational and electronic states have to be included in equation (4.32). For a given temperature T, α becomes

$$\alpha = \frac{2\pi^2\nu\mu_0^2(J''+1)Ne^{-E_0/kT}}{3\epsilon_0 hcq_{rot}}\left(1 - e^{-h\nu/kT}\right). \tag{4.33}$$

An example for rotational branches is plotted in Fig. 4.2 using equation (4.24) and (4.26) for line positions and equation (4.33) for intensity.

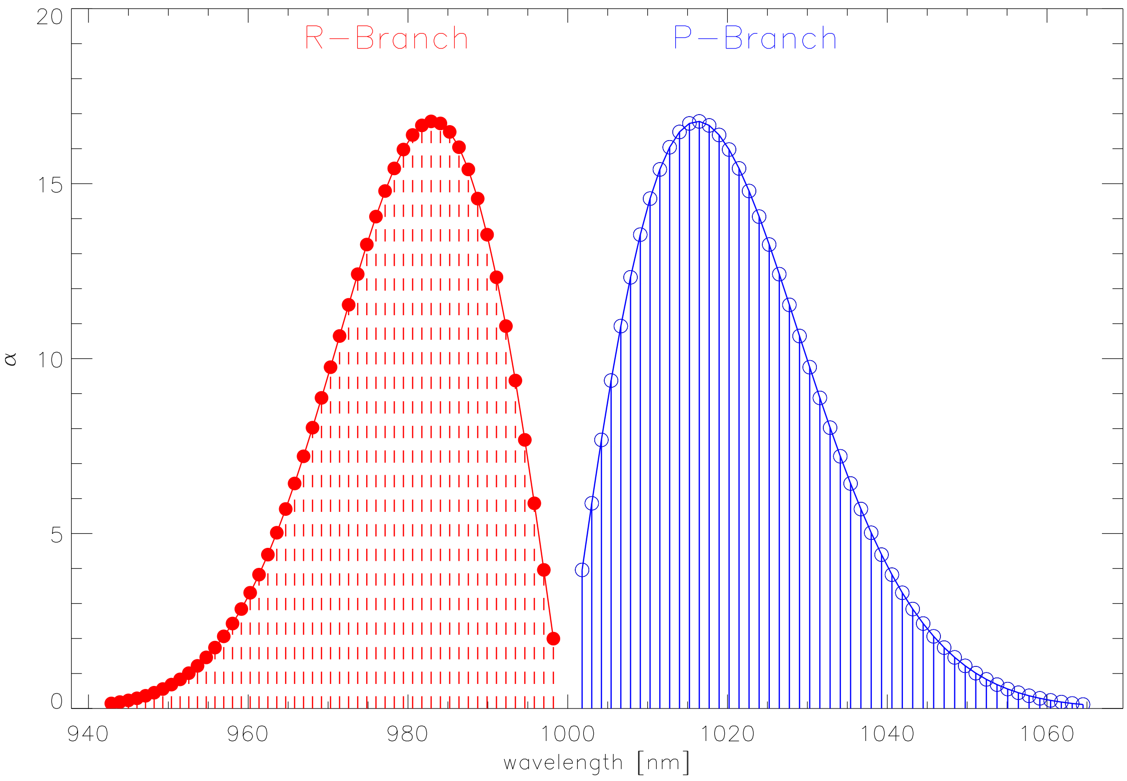

Figure 4.2: Rotational intensities of the P- and R-branches.

4.2.3 Non-Rigid Rotation

In the previous sections, the assumption of rigid rotation of the molecule was used. That means that the nuclei do not change their distance while they are rotating. But due to this rotation, a centrifugal force appears and the distance between the nuclei changes, since the bond is not rigid. For diatomic molecules, it is possible to describe the influence of the rotation, by stretching of the bond from r_e to r_c, which are the internuclear separations at equilibrium and under the action of centrifugal force, respectively. The centrifugal force (Herzberg, 1950)

$$F_c = \frac{\mu v^2}{r} = \mu \omega^2 r = \frac{J^2}{\mu r^3} \tag{4.34}$$

is compensated by the Hook's law restoring force in the bond

$$F_r = k(r_e - r_c). \tag{4.35}$$

The potential energy of the distorted rotator is

$$E = \frac{J^2}{2\mu r^2} + \frac{1}{2} k (r_c - r_e)^2. \tag{4.36}$$

Substituting $(r_c - r_e)$ in equation (4.36) by equating equation (4.34) and equation (4.35), gives

$$E = \frac{\hbar^2}{2\mu r_e^2} J(J+1) - \frac{\hbar^4}{2\mu^2 r_e^6} (J(J+1))^2, \tag{4.37}$$

where the quantum mechanical expression for J was inserted and the equilibrium distance r_e was used. This potential energy results for the energy levels of the distorted rotator in

$$F(J) = BJ(J+1) - D(J(J+1))^2, \tag{4.38}$$

with $D = \frac{4B_e^3}{\omega_e^2}$.

As indicated before, the rotational constant also depends on the vibrational and electronic state. That is because the molecule spends more time at larger separation distances r, where the potential is flatter. That means, that the average internuclear distance $\langle r \rangle$ increases with v and B decreases

$$B_v = \frac{\hbar^2}{2\mu}\langle\frac{1}{r^2}\rangle. \tag{4.39}$$

The dependence from the vibrational levels is parametrized by

$$B_v = B_e - \alpha_e(v + \frac{1}{2}) + \gamma_e(v + \frac{1}{2})^2 + \cdots \tag{4.40}$$

and

$$D_v = D_e + \beta_e(v + \frac{1}{2}) + \cdots . \tag{4.41}$$

So, equation (4.38) becomes

$$F(J) = B_v J(J+1) - D_v(J(J+1))^2. \tag{4.42}$$

4.3 Vibrational Spectroscopy

4.3.1 The Anharmonic Oscillator

From equation (4.16) one can see that the energy for the harmonic oscillator is

$$E_v = \hbar\omega(v + \frac{1}{2}). \tag{4.43}$$

The vibrational quantum number v is used instead of n, and $\omega = \sqrt{\frac{k}{\mu}}$. The approximation of the harmonic oscillator is only valid for small v, because for larger v the internuclear distance changes and the bond is stretched and contracted more strongly. In order to describe these states one assumes an anharmonic oscillator which can be described adding a cubic term to the harmonic oscillator potential

$$V(r) = k(r - r_e)^2 + g(r - r_e)^3. \tag{4.44}$$

One can add higher terms for more accuracy. The same result is obtained if the Taylor series used in equation (4.13) is expanded to higher order terms. In this way also the constants are determined by the derivations of the potential at the equilibrium position r_e. Another popular choice for the potential is the Morse potential

$$V(r) = D(1 - e^{-\beta(r-r_e)})^2. \tag{4.45}$$

The Morse potential is able to approach the dissociation limit $V(r) = D$ as $r \to \infty$ (see Fig. 4.3). At this limit the bond breaks and the molecule is separated in its constituents. For molecules in the ground state, this results always in neutral atoms. With the approximation of the anharmonic oscillator, the energy levels of the vibrational states become

$$G(v) = \omega_e(v + \frac{1}{2}) - \omega_e x_e((v + \frac{1}{2}))^2. \tag{4.46}$$

The energy states for the vibrating rotator then become using equation (4.40), (4.41), and (4.42),

$$E(\mathrm{cm}^{-1}) = \omega_\mathrm{e}(\mathrm{v} + \frac{1}{2}) - \omega_\mathrm{e}\mathrm{x_e}((\mathrm{v} + \frac{1}{2}))^2 + \mathrm{B_e J(J+1)} - \mathrm{D_e(J(J+1))}^2 - \alpha_\mathrm{e}(\mathrm{v} + \frac{1}{2})\mathrm{J(J+1)} + \cdots \tag{4.47}$$

With the Morse potential, it is possible to solve the Schrödinger equation analytically and one can obtain analytical expressions for the constants in equation (4.47),

$$\omega_e = \beta\left(\frac{Dh \cdot 10^2}{2\pi^2 c\mu}\right)^{1/2} \tag{4.48}$$

$$\omega_e x_e = \frac{h\beta^2 \cdot 10^2}{8\pi^2 \mu c} \tag{4.49}$$

$$B_e = \frac{h \cdot 10^2}{8\pi^2 \mu r_e^2 c} \tag{4.50}$$

$$D_e = \frac{4B_e^3}{\omega_e^2} \tag{4.51}$$

$$\alpha_e = \frac{6(\omega_e x_e B_e^3)^{1/2}}{\omega_e} - \frac{6B_e^2}{\omega_e}. \tag{4.52}$$

The spectroscopic constants which were used here are given in cm^{-1}, because it is custom in molecular spectroscopy, but the physical constants are given in SI units.

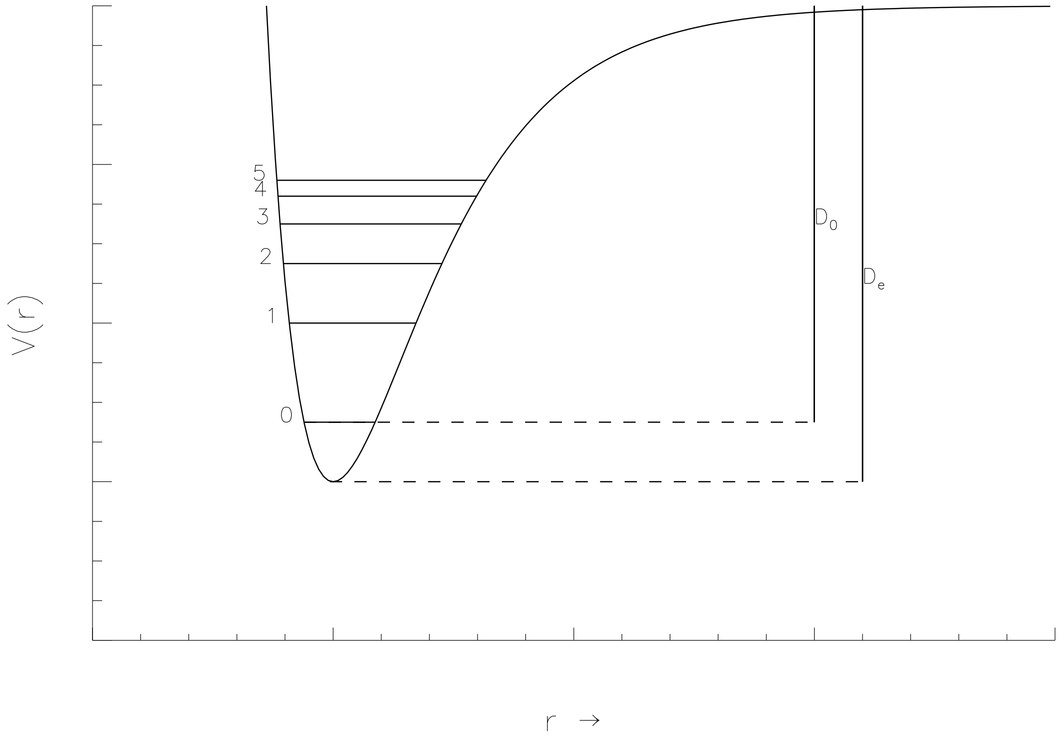

Figure 4.3: Morse potential with energy levels.

4.3.2 Selection Rules

In order to describe the line intensities, selection rules are required as seen before for the rotational transitions. Again, the intensity of a vibrational transition is determined by the transition dipole moment integral,

$$\mathbf{M} = \int \Psi'^{*}_{vib} \mu(r) \Psi''_{vib} dr. \tag{4.53}$$

Expansion of the transition dipole moment in a Taylor series about $r = r_e$ gives,

$$\mu = \mu_e + \frac{d\mu}{dr}|_{r_e}(r - r_e) + \frac{1}{2}\frac{d^2\mu}{dr^2}|_{r_e}(r - r_e)^2 + \cdots , \tag{4.54}$$

so that

$$\mathbf{M} = \mu_e \int \Psi'^{*}_{vib} \Psi''_{vib} dr + \frac{d\mu}{dr}|_{r_e} \int \Psi'^{*}_{vib}(r - r_e)\Psi''_{vib} dr + \cdots . \tag{4.55}$$

Since vibrational wave functions for the same potential are orthogonal to each other, the first term in equation (4.55) vanishes. The dominant contribution for the intensities of most infrared fundamental transitions stems from the second term in equation (4.55). It depends on the derivative of the dipole transition moment at the equilibrium distance. The intensity is then proportional in first order to the square of the second term in equation (4.55),

$$I \propto |M_{v',v''}|^2 \propto |\frac{d\mu}{dr}|^2_{r_e}. \tag{4.56}$$

In this approximation, it is assumed that the electrical dipole moment function is a linear function of r in the region close to $r = r_e$. In contrast to equation (4.29), where the intensity depends on μ_0^2 for rotational transitions, the intensity for vibrational transitions depends not only on μ, but also on the distance between the atoms. Again, if a molecule has no dipole moment, no transitions are allowed in first order.

The intensity of a vibrational transition also depends on the value of

$$\langle v'|x|v''\rangle = \int \Psi'^{*}_{vib}(r - r_e)\Psi''_{vib} dr, \tag{4.57}$$

where $x = r - r_e$. In the case of the harmonic oscillator, one can use the Hermitian polynomials as valid wave functions in equation (4.57). For the Hermitian polynomials, there is the recursive relationship

$$2xH_n(x) = H_{n+1}(x) + 2nH_{n-1}(x). \tag{4.58}$$

Employing this in equation (4.57), one obtains the result

$$\langle v'|x|v''\rangle = \left(\frac{\hbar}{2m\omega}\right)^{1/2} (\sqrt{v+1}\delta_{v',v+1} + \sqrt{v}\delta_{v',v-1}), \tag{4.59}$$

where the allowed transitions are those with

$$\Delta v = \pm 1, \tag{4.60}$$

because $v' = v + 1$ or $v - 1$ in the Kronecker δ. With the use of wave functions for the anharmonic oscillator, which are given by an expansion of the harmonic wave functions $\Psi_{i,HO}$ as linear combinations

$$\Psi_{vib} = \sum c_i \Psi_{i,HO}, \tag{4.61}$$

transitions with

$$\Delta v = \pm 2, \pm 3, \ldots\ , \tag{4.62}$$

are also only allowed. The intensities of these so called overtones decrease strongly with increasing Δv by factors of 10 or 20 per one unit in Δv. If one does not truncate the expansion of the transition dipole moment in equation (4.54) after the first order and allows higher order terms, also vibrational transitions with $\Delta v = \pm 2, \pm 3, \ldots$ also become allowed. The contribution of both, mechanical anharmonicity and electrical anharmonicity, results in observable overtones. Later, it will be seen, that if electronic transitions are present, also vibrational transitions with $\Delta v = 0$ become allowed.

Nomenclature

There are specific names for the different vibrational transitions. Transitions from the ground state to the first state $v = 1 \leftarrow 0$ is called the *fundamental*, from the ground state to second state $v = 2 \leftarrow 0$ is called the *first overtone* or *second harmonic* and so on. Transitions which occur not from the ground state are called *hot bands*, because they increase in intensity with increasing temperature. Transitions with the same Δv are called a *sequence* e.g. the $(0, 1)$, $(1, 2)$, $(2, 3)$ bands form the $\Delta v = -1$ sequence. If a series of bands occur all from the same level, like $(3, 1)$, $(2, 1)$, $(1, 1)$, $(0, 1)$, then it is called a *progression.*

4.3.3 Intensities

In order to calculate the intensities of the lines in a vibrational transition, one has again to compute the transition dipole moment. This is given by the line strength factor $S_{J'J"}$ and consists of both, transition dipole moment from rotation and vibration,

$$S_{J'J''} = \sum_{M'} \sum M'' |\langle \Psi_{v'J'M'} | \mu | \Psi_{v''J''M''} |^2 = |\mathbf{M}_{v'v''}|^2 \cdot S_{J''}^{\Delta J} \cdot F(m). \tag{4.63}$$

$|\mathbf{M}_{v'v''}|^2$ is the vibrational part, $S_{J''}^{\Delta J}$ is the rotational part, given by a Hönl-London factor, and $F(m)$ is a correction term, called a Herman-Wallis factor. $|\mathbf{M}_{v'v''}|^2$ can be calculated from equation (4.53) - (4.59) and the Hönl-London factors will be described later. $S_{J'J''}$ can then be used in the absorption cross section

$$\sigma = \frac{2\pi^2 \nu S_{J'J''}}{3\epsilon_0 hc(2J'' + 1)}, \tag{4.64}$$

which enters the absorption coefficient

$$\alpha = \frac{\sigma(2J'' + 1)}{q_{rot,vib}} e^{-E_0/kT} \left(1 - e^{-h\nu/kT}\right) N. \tag{4.65}$$

Then Beer's absorption law becomes,

$$I = I_0 e^{-\alpha l}. \tag{4.66}$$

4.4 Electronic Spectroscopy

In order to describe the electronic states, one can start with equation (4.6)

$$H_el\Psi_{el,\mathbf{R}_k}(\mathbf{r}_1,...,\mathbf{r}_2) = E_{el}(\mathbf{R})\Psi_{el,\mathbf{R}_k}(\mathbf{r}_1,...,\mathbf{r}_2), \tag{4.67}$$

where the electron Hamiltonian is given by equation (4.2)

$$H_{el} = \sum_{\nu=1}^{N} \frac{-\hbar^2}{2m_e}\Delta_\nu + \sum_{\nu=2}^{N}\sum_{\mu=1}^{\nu-1} \frac{e^2}{|\mathbf{r}_\nu - \mathbf{r}_\mu|} - \sum_{\nu=1}^{N}\sum_{k=1}^{2} \frac{Ze^2}{|\mathbf{r}_\nu - \mathbf{R}_k|}. \tag{4.68}$$

For the solution of equation (4.67), it is assumed that Ψ_{el} consists of molecular orbitals (MOs) where each MO is a linear combination of atomic orbitals. In the molecular system, the atomic orbitals of the involved atoms are not spherically symmetric anymore, due to the distortion from the other atoms in the molecule. That means that each electron with orbital angular momentum l starts to precess about the internuclear axis. This means, that l is no longer a good quantum number, but the projection of $\hat{\mathbf{l}}$ onto the internuclear axis, m_l, is still useful. When the circulation of the electron around the internuclear axis is left- or right-handed, the sign of m_l is positive or negative, but that does not change the energy of the electronic state, and hence it is degenerate.

$$\lambda = |m_l| = 0, 1, 2, ..., l. \tag{4.69}$$

Labeling of the Molecular Electronic States

m_l can have the values of l, therefore the labeling of the different orbitals for molecules can be analogous to the labeling of atomic orbitals and is given in Table 4.1 The electronic states of diatomic molecules are also labeled in analogy to the atomic states with $^{2S+1}\Lambda_\Omega$ instead of $^{2S+1}L_J$. In the atomic case, L is the total orbital angular momentum, S is the total electron spin, and $J = S + L$ is the total angular momentum. In the molecular case, the projection of the orbital angular momentum along the internuclear axis is $\Lambda = \sum \lambda_i$ and can take the values:

Table 4.1

Atomic Orbital l	Molecular Orbital λ
s	sσ
p	pσ, pπ
d	dσ, dπ, dδ
f	fσ, fπ, fδ, fϕ

$$\begin{array}{rcl} \Lambda & = & 0\ 1\ 2\ 3\ 4\ ... \\ & & \Sigma\ \Pi\ \Delta\ \Phi\ \Gamma\ ...\ . \end{array} \tag{4.70}$$

The capital Greek letters, are used for the multi-electron molecular, parallel to the atomic case, where S, P, D, F, ..., are used. S is also the total electron spin whose projection onto the internuclear axis is labeled with $\Sigma = S, S-1, ..., -S$. $\Omega = \Lambda + \Sigma$ is the projection of the total angular momentum in the molecular case onto the internuclear axis, The total angular momentum $\mathbf{J}$ itself is the vectorsum of orbital $\mathbf{L}$, spin $\mathbf{S}$, and rotational $\mathbf{R}$ angular momenta, $\mathbf{J} = \mathbf{L} + \mathbf{S} + \mathbf{R}$.

There is an additional labeling to the electronic states in diatomic molecules, which gives the excitation state. X is for the ground state, and in order of increasing energies, A, B, C and so on, except X are for the excited states of the same multiplicity $(2S+1)$ as the ground state. If the multiplicity is different from the ground state, then the states are labeled with lowercase letters a, b, c and so on.

4.4.1 Selection Rules

The different electronic states are again governed by selection rules, which are based on the allowed transitions for the described quantum numbers. The most common selection rules are:

1. $\Delta\Lambda = 0, \pm 1$. That means, that e.g. the transitions between $\Sigma - \Sigma$, $\Pi - \Sigma$, $\Sigma - \Pi$, ..., are allowed.
2. $\Delta S = 0$. This rule is more or less empirical, since the transition with $\Delta S \neq 0$ are very weak for molecules which consists only of light atoms. For molecules with heavy atoms, the spin-orbit coupling increases and the change of multiplicity become more strongly allowed.
3. $\Delta\Sigma = 0$. This relation holds only for Hund's case (a) coupling scheme, which will described later.
4. $\Delta\Omega = 0, \pm 1$. In the case of Hund's case (a), $\Delta\Omega = \Delta\Lambda$ and the selection rule for Λ is applied.
5. $+ \leftrightarrow +$ and $- \leftrightarrow -$. This symmetry selection rule applies only to $\Delta\Lambda = 0$ transitions and is a consequence of the μ_z transition dipole moment having Σ^+ symmetry. It states that only transitions between symmetric or anti-symmetric wave functions are allowed.
6. $g \leftrightarrow u$. This selection rule is only valid for homonuclear molecules and states that only transitions between grade and ungrade parity are allowed.

With these selection rules, one is able to determine the possible electronic transitions, where then the vibrational and rotational transitions can take place.

4.4.2 Vibronic Transitions

The spectral distribution of a molecule is built up on the electronic transition on which the vibrational transitions take place which are made up of rotational lines. That means that one finds for a specific electronic transition a vibrational band structure, and in these various bands, one can find the rotational line structure.

The positions of the vibrational bands, can be determined using equation (4.46) and adding $\Delta T_e = E_{upper} - E_{lower}$, which is the separation between the potential minima of the two electronic states.

$$E(\mathrm{cm}^{-1}) = \Delta\mathrm{T_e} + \omega_\mathrm{e}'(\mathrm{v}' + \frac{1}{2}) - \omega_\mathrm{e}\mathrm{x}_\mathrm{e}'((\mathrm{v}' + \frac{1}{2}))^2 + \cdots - \omega_\mathrm{e}''(\mathrm{v}'' + \frac{1}{2}) - \omega_\mathrm{e}\mathrm{x}_\mathrm{e}''((\mathrm{v}'' + \frac{1}{2}))^2 + \cdots \tag{4.71}$$

In this case, also vibronic transitions with $\Delta v = 0$ are allowed, since the upper and lower electronic states are different.

In principle all possible vibrational transitions are now allowed, but their intensities in a certain electronic transition are governed by the strength of the electronic transition itself, the population of the vibrational transition, and the *Franck-Condon factor*, which describes the squared overlap integral of the two vibrational wave functions. The latter results from the *Franck-Condon principle*. In the classical description, it can be explained by the idea, that the electronic transitions occur very quickly ($\sim 10^{-15}$ s), and in this short time, the nuclei have no time to move, which means, that vibration, rotation, and translation are "frozen". In a plot with two electronic states, with the potential location on the x-axis and the energy on y-axis, the electronic transition occurs 'vertically' (see Fig. 4.4). If one adds the quantizised vibrational levels in this plot and assume

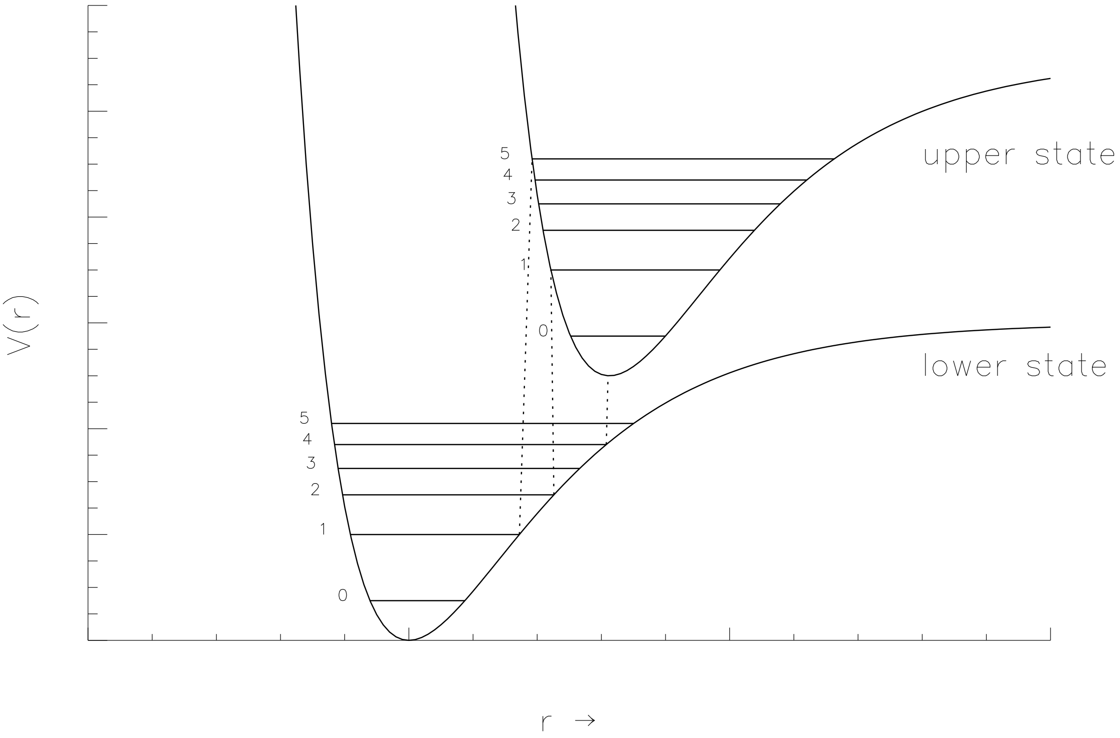

Figure 4.4: Visualisation of the Franck-Condon principle.

that the vibrating molecule spents more time at the turning points for transitions with $v > 0$, then it is assumed that the transitions with equal potential positions are strong, since the overlap of their wave functions is large.

The transition dipole moment for the electronic transition is given by

$$R_e = \int \Psi'_e \mu \Psi''_e dr_e, \tag{4.72}$$

with μ as the dipole moment and the integration is over the electronic coordinates r_e. In case of a vibronic transition, the transition dipole moment R_{ev} is given by

$$R_{ev} = \int \Psi'_{ev} \mu \Psi''_{ev} dr_e, \tag{4.73}$$

and the vibronic wave function Ψ_{ev} can be factorized into $\Psi_e \Psi_v$. The transition dipole moment then becomes

$$R_{ev} = \int \Psi'_e \mu \Psi''_e dr_e \int \Psi'_{ev} \mu \Psi''_{ev} dr_v = R_e \int \Psi'_v \mu \Psi''_v dr_v = R_e \langle v' | v'' \rangle. \tag{4.74}$$

The intensity of the vibronic transition is proportional to the square of the transition dipole moment, which then is

$$I_{e'v'e''v''} \propto |R_e|^2 q_{v'-v''}, \tag{4.75}$$

where $q_{v'-v''} = |\langle v' | v'' \rangle|^2$ is the *Franck-Condon factor*.

4.4.3 Rovibronic Transitions

For the rotational transitions in the vibronic system (rovibronic transitions) are in case of $\Delta\Omega = 0$ (singlet-singlet transitions) only three types possible:

1. $\Delta\Lambda = 0$, $\Lambda'' = \Lambda' = 0$. In this case, only R- and P-branches are possible.
2. $\Delta\Lambda = \pm 1$. Strong Q-branches are present, but also strong P- and R-branches.
3. $\Delta\Lambda = 0$, $\Lambda'' = \Lambda' \neq 0$. These transitions are characterized by weak Q-branches, but strong P- and R-branches.

The occurrence of a Q-branch is dependent on the difference between the rotational constants for the upper and lower level. This difference is in general very small in pure vibrational transitions, but can be large for different electronic states, since the bonding between the nuclei can be very different in these states.

Reconsider equation (4.24)-(4.26),

$$\begin{aligned} \nu(R) &= F(J') - F(J'') &&= \nu_0 + 2B' + (3B' - B'')J'' + (B' - B'')J''^2 && (4.76) \\ \nu(Q) &= F(J') - F(J'') &&= \nu_0 + (B' - B'')J'' + (B' - B'')J''^2 && (4.77) \\ \nu(P) &= F(J') - F(J'') &&= \nu_0 - (B' + B'')J'' + (B' - B'')J''^2, && (4.78) \end{aligned}$$

which shows that for large difference between B' and B'' the quadratic term in J'' becomes significant. The spacing between the rotational lines for $B' < B''$ will increase for the P-branch as J'' increases, but the spacing for the R-branch will decrease with increasing J''. In the latter case there will also be a turning point, where the R-branch change its direction in line positions. In this case a *band head* is formed, since at this turning point, the R-branch lines overlap and are very dense distributed. Such a band head is called red degraded since it turns to longer wavelengths. If $B' > B''$, then the band head will be in the P-branch and it is called blue degraded since it turns to shorter wavelengths. An example for a progression of rovibronic transitions is plotted in Fig. 4.5. In this figure, $\Delta B = 0.2$ and the R-branch is red degraded.

4.4.4 Rovibronic Intensities

The Einstein A value, which determines the intensities of the rovibronic lines is given by:

$$A = \frac{16\pi^3\nu^3}{3\epsilon_0 h c^3 (2J' + 1)} q_{v'-v''} |R_e|^2 S_{J''}^{\Delta J}, \tag{4.79}$$

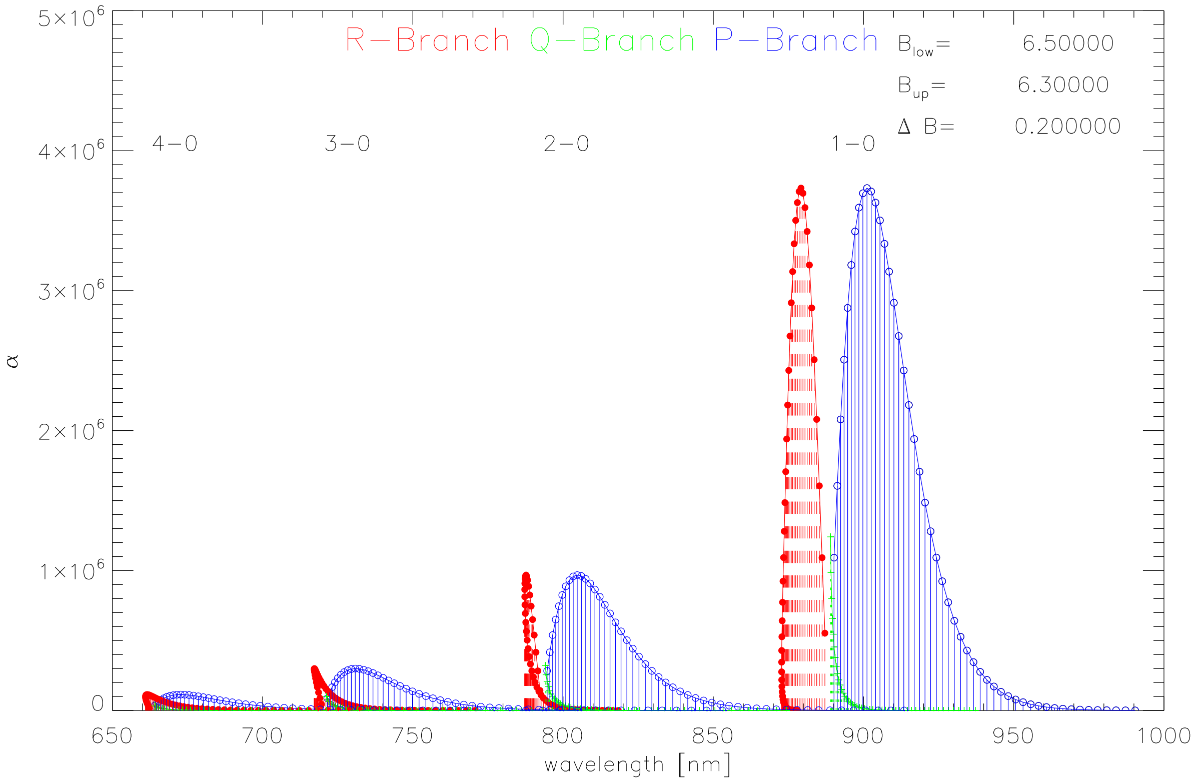

Figure 4.5: Fundamental sequence of vibrational bands.

where $\mu_0^2(2J''+1)$ from equation (4.28) was substituted with $q_{v'-v''}|R_e|^2 S_{J''}^{\Delta J}/(2J''+1)$. $S_{J''}^{\Delta J}$ is the term for the rotational line strength which is in the case of rovibronic transitions given by the Hönl-London factors which describes the relative intensities of rotational lines. For Hund's case (a) and $\Delta\Sigma = 0$ the Hönl-London factors for $\Delta\Lambda = 0$ are given by:

$$\begin{aligned} S_{J''}^{R} &= \frac{(J''+1+\Lambda)(J''+1-\Lambda)}{J''+1} \\ S_{J''}^{Q} &= \frac{(2J''+1)\Lambda^2}{J''(J''+1)} \\ S_{J''}^{P} &= \frac{(J''+\Lambda)(J''-\Lambda)}{J''} \end{aligned} \tag{4.80}$$

Hund's Cases

There are different Hund's cases, which gives rules for describing the coupling between the total angular momentum J and the total electron spin S in the separate atoms. This is important since the rotation and vibration of the molecule takes place simultaneously with the electronic motions. In general the interaction between vibration and electronic motion is already taken into account, since the approximation of the anharmonic oscillator potential includes it. What is left is the interaction between the rotation and electronic motion. The interaction is described in terms of Hönl-London factors, which are computed in the appropriate Hund's case. Only in the case when

$S = \mathit{\Lambda} = 0$, which describes a $^1\mathit{\Sigma}$ state, the angular momentum of nuclear rotation is identical with the total angular momentum J and it can be treated as simple rotator (see Chapter 4.2). In all other cases, one needs a special description. There are two limiting cases which will be briefly described in the following:

Hund's case (a) coupling describes the case, where the electric field of a molecule is so strong, that the interaction between the individual rotational levels J_i and spins S_i can be disregarded because it is very weak. Due to this assumption, the angular momentum $\mathit{\Omega} = \mathit{\Lambda} + \mathit{\Sigma}$ is well defined and a 'good' quantum number.

Hund's case (b) coupling describes the case where $\mathit{\Lambda} = 0$ and $S \neq 0$, that means that the spin vector S is not coupled to the internuclear axis, and hence $\mathit{\Omega}$ is not well defined anymore. In light molecules, even if $\mathit{\Lambda} \neq 0$, S is only be weakly or not coupled to the internuclear axis.

There are also Hund's case (c), (d), and (e) coupling schemes, which will not be described here. It can also be that the coupling is between one of these cases, or changes from one to another case with changing J, in this case the description is more complicated and can be treated numerically or asymptotically.

Chapter 5

The FeH Molecule

Wing & Ford (1969) were the first to detect a broad molecular absorption band around 991 nm in late M dwarfs. This band was later found in S stars (Wing, 1972) and in sun spots. Nordh et al. (1977) identified the Wing-Ford band as the $0-0$ band of an FeH electronic transition. The FeH molecule is well suited for the measurements mentioned in the introduction because of its intrinsically narrow and well isolated spectral lines. These lines are also an ideal tracer of line broadening in M-stars due to convection or very slow rotation (Reiners, 2007).

In this chapter I will describe the basic properties of the FeH molecule. Since it is so far only rarely described in the literature, it was necessary to derive some more properties from the basic molecular data, to make it feasible for the use in stellar spectral line formation synthesis.

5.1 Molecular Data

The FeH molecule consists of the atomic elements hydrogen (H) and iron (Fe). They have an atomic mass of 1.0079 u and 55.8450 u, respectively (Mortimer, 2001). Hence the molecular mass of FeH is 56.8529 u, which is $9.4404243 \cdot 10^{-26}$ kg. The reduced mass $\mu = \frac{m_H \cdot m_{Fe}}{m_H + m_{Fe}}$ is 0.990032 u or $1.6439478 \cdot 10^{-27}$ kg.

The FeH molecules separates in its constituents at a dissociation energy $D = 1.598\,\mathrm{eV}$ (Dulick et al., 2003). The ionisation energy could not found in the literature, and hence had to be calculated.

5.1.1 Ionisation Energy of FeH

In order to obtain the ionisation energy of FeH, it is assumed that there is a correlation between dissociation energy and ionisation energy due to the description which was given by Sauval & Tatum (1984), which, in the case for FeH, is

$$D(\mathrm{FeH}\ ) + E_{Ion.}(Fe) = D(\mathrm{FeH}\ ^{+}) + E_{Ion.}(\mathrm{FeH}\ ). \tag{5.1}$$

If there is a correlation for hydride, this could be visible in an “Ionisation Energy - Dissociation Energy”-diagram (Fig.5.1). For hydride’s the influence of the hydrogen atom is similar in the molecules, and the ionisation energy E_{Ion} of atoms becomes lower with higher periods in the period diagram, and higher towards a noble gas configuration. If one also neglects the dissociation energy D of the ionized hydrides, then a direct correlation between D and E_{Ion} for the molecules can be expected. In this Fig.5.1 $E_{Ion.}$ and D for a large number of hydride (Wilkinson, 1963)

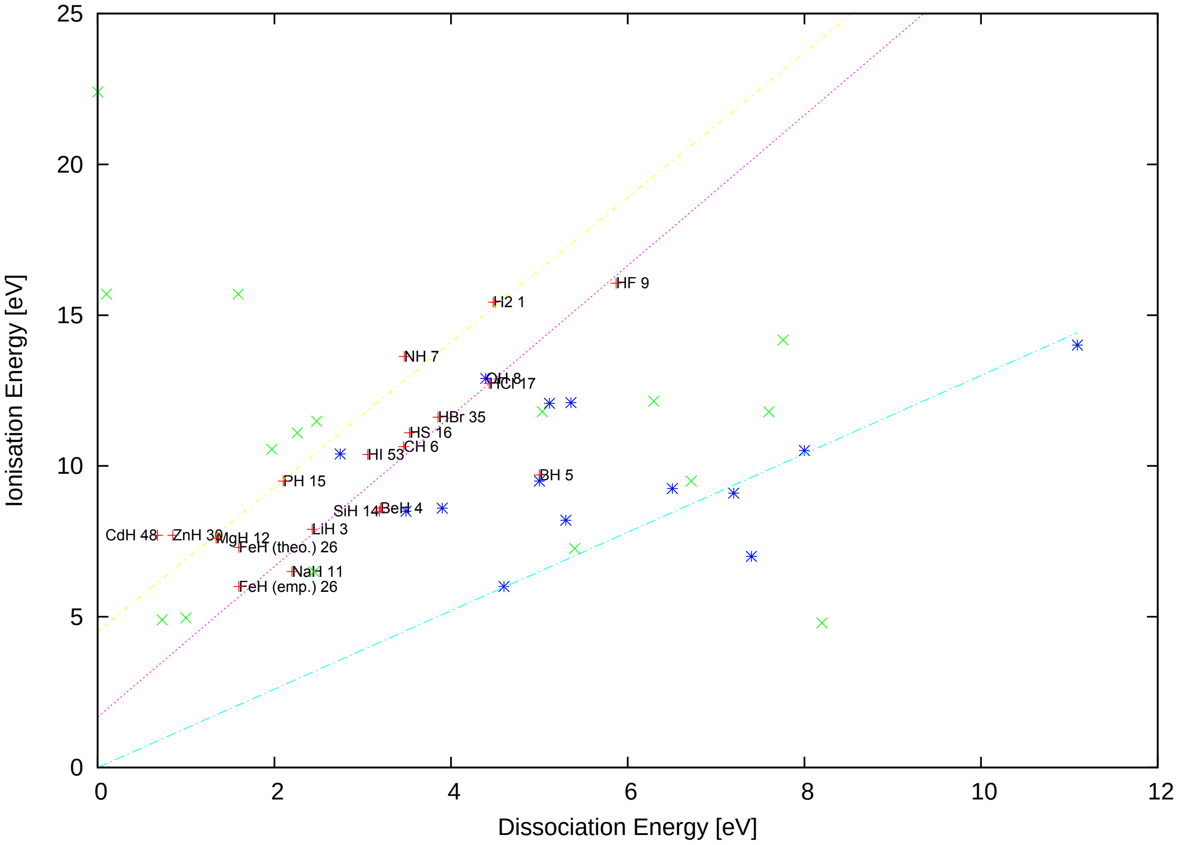

Figure 5.1: Ionisation energy as a function of dissociation energy for a sample of molecules. Red crosses are for hydride, labeled with names and atomic number. Blue asterisk are for oxides, and green × are for other molecules.

is plotted. It is clear that there is a linear dependence of $E_{Ion.}$ on D which can be used to determine $E_{Ion.}$. For FeH a linear fit through the hydride (red symbols in Fig.5.1) was made, in order to obtain an ionisation energy for FeH of approximately 6 eV. However, there are two sorts of hydride, which can be fitted separately. I assume that these two groups consists of different kinds of bounding which results in different ionisation energies. I also tried to fit the oxides (blue symbols in Fig.5.1) in a similar way, but there is no clear correlation visible. Also some other molecules (green symbols in Fig.5.1) show no correlation between ionisation energy and dissociation energy.

A theoretical computation of $E_{Ion.}$ for FeH was done by Bernath 2008 (private communication) also from the ionisation-potential of Fe and the dissociation energies of FeH $^+$ and FeH which yields 7.3 eV. This value is also included in Fig. 5.1 and for the dissociation energy of FeH, it is between the two groups of hydride. So it is still not clear to which group FeH belongs, and I will use in the following the empirically obtained value of $E_{Ion.} = 6$ eV. Since this value is only required for the computation of the pressure broadening of FeH lines, which will turn out is rather insensitive to this parameter, the possible error which is introduced is negligible.

5.1.2 Partition Function of FeH

The partition function of a molecule is needed in order to derive the dissociative equilibrium constant. This describes the relative fraction of the participating atoms to the resulting molecule dependent from the surrounding temperature.

In order to compute the partition function Q for FeH a combination of the tabulated partition function in Dulick et al. (2003) and an analytically determined one from Eq.1 in Sauval & Tatum (1984) is used (in collaboration with Matthias Steffen 2007).

$$Q = \exp\left[\frac{hc}{kT}\left(\frac{1}{2}\omega_e - \frac{1}{4}\omega_e x_e\right)\right] \sum_e \sum_v \frac{g_e kT}{\sigma hc}\left[B_e - \alpha_e\left(v + \frac{1}{2}\right)\right]^{-1} \times \exp\left\{-\frac{hc}{kT}\left[\omega_e\left(v+\frac{1}{2}\right) - \omega_e x_e\left(v+\frac{1}{2}\right)^2 + T_e\right]\right\}. \quad (5.2)$$

In this equation, σ is a symmetry factor, which is unity for heteronuclear (which is the case for FeH), and two for homonuclear molecules. g_e is the statistical weight of the electron and it is $2S+1$ for Σ states and $2(2S+1)$ for others. The other molecular constants used in equation (5.2) are taken from Table 9 and 10 in Dulick et al. (2003). In Fig. 5.2, the partition functions for the summation of energy levels and analytical ones from Dulick et al. (2003) are plotted together with the one derived from equation (5.2). The one from the summation of energy levels is much lower for high temperatures than the analytic one and my own. This will be important for the concentration of FeH in M-type stars.

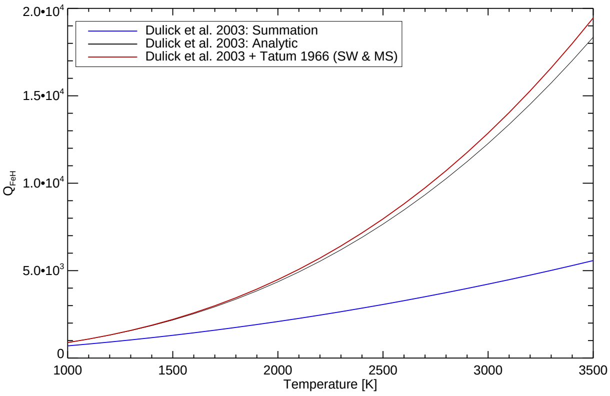

Figure 5.2: Partition function for the FeH molecule from different descriptions against temperature.

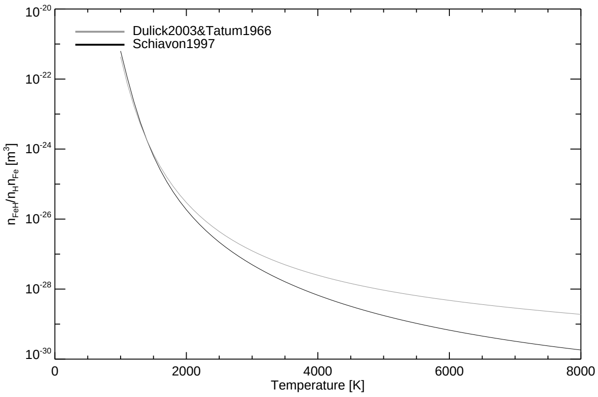

Figure 5.3: Concentration of FeH relative to H and Fe as a function of temperature.

The equilibrium constant K for FeH is given by (e.g. Tatum, 1966),

$$\frac{p_H p_{Fe}}{p_{FeH}} = K(T) = \left(\frac{2\pi\mu kT}{h^2}\right)^{\frac{3}{2}} kT \frac{Q_H Q_{Fe}}{Q_{FeH}} e^{-D/kT}. \quad (5.3)$$

Q_H and Q_{Fe} are the partition function for hydrogen and iron, respectively. K can be converted to a concentration C of FeH relative to the number of hydrogen and iron atoms.

$$K(T) = \frac{p_H p_{Fe}}{p_{FeH}} = \frac{n_H n_{Fe}}{n_{FeH}}\, kT, \quad (5.4)$$

and hence,

$$C(T) = kT/K(T). \tag{5.5}$$

With the partition function from the summation of energy levels, the concentration of the FeH molecule would be underestimated. In Fig. 5.3 the concentration for my partition function is plotted and for comparison, the one used by Schiavon et al. (1997). The latter ones returns lower FeH number for high temperatures, which would result in weaker band strength.

5.2 Van der Waals Broadening

Since the FeH molecular lines become significant towards low effective temperatures in dwarfs, the influence of pressure broadening becomes important. The common way to describe the interaction of two different neutral perturbers is the van der Waals broadening $\Delta\nu = \frac{C_6}{r^6}$. $\Delta\nu$ is the frequency shift which results, and r is the relative distance between the perturbers. C_6 is the interaction constant. The van der Waals broadening produces a Lorentzian shape $\left(g(\nu) = \frac{\gamma}{(\gamma/2)^2+(2\pi)^2\nu^2}\right)$ in the line profiles, 'van der Waals wings'. The full-width half maximum is given by

$$\gamma = 17 C_6^{2/5} v^{3/5} N_P. \tag{5.6}$$

C_6 can be calculated by the hydrogenic approximation from Unsöld (1955). This is of course not the best way to describe the perturbation of a molecule from other particles, but there are no detailed calculations for FeH in the literature, so far. Schweitzer et al. (1996) provide a sophisticated description for the van der Waals broadening in M dwarfs, including the polarizability and the concentration of the most significant perturbers.

$$C_6^0 = \frac{\alpha_P}{\alpha_H} 1.01 \times 10^{-32} (Z+1)^2 \times \left[\frac{E_H^2}{(E_{Ion}-E_l)^2} - \frac{E_H^2}{(E_{Ion}-E_u)^2}\right] cm^6 s^{-1}. \tag{5.7}$$

$E_H = 13.6\,\mathrm{eV}$ is the ionisation energy of hydrogen, $E_{Ion} = 6\,\mathrm{eV}$ that of FeH, E_u and E_l are the upper and lower energy levels respectively, α_P the polarizability of the perturbers, α_H that of hydrogen, and Z is the charge of the absorber. The total van der Waals broadening constant is then the sum over the individual ones for the different perturbers

$$\gamma_{tot} = \sum_i \gamma_i. \tag{5.8}$$

In equation (5.7), the ionisation energy of FeH enters the van der Waals broadening and introduces an uncertainty. In order to roughly estimate the error, in Fig. 5.4 the dependence of γ_{tot} from E_{Ion} is shown (upper panel). I also compute an FeH line with different γ_{tot} for different E_{Ion} and measure the $FWHM$. This is plotted in the lower panel of Fig. 5.4. From this figure it is visible that the difference in the line profile is on the order of $25\,\mathrm{ms}^{-1}$.

5.3 Appearance of FeH in Stellar Spectra

FeH molecular lines seem to appear over a wide range in the infrared. There are detections of FeH band system in the z-, J-, and H-band filter regions. A great overview is given in the paper from Cushing et al. (2003) and the dependence of these FeH bands on effective temperature is

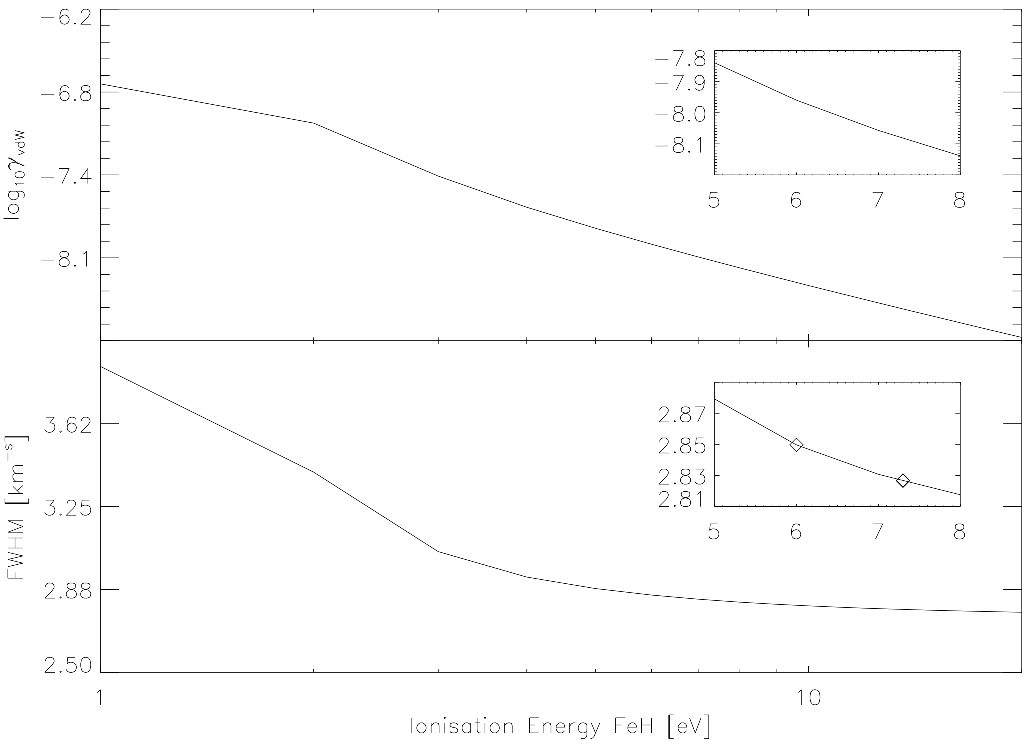

Figure 5.4: Van der Waals broadening constant (upper panel) and FWHM (lower panel) for an arbitrary FeH line as a function of ionisation energy.

nicely shown in Cushing et al. (2005). In the z-, and J-band, the FeH features are produced by the $F\,{}^4\Delta{-}X\,{}^4\Delta$ electronic transition and in the H-band by the $E\,{}^4\Pi{-}A\,{}^4\Pi$ electronic transition. The latter transition is theoretically described by Balfour et al. (2004) and Hargreaves et al. (2010). Due to the significant differences in upper and lower B values, FeH shows band structures with band heads due to inversion of the P- and R-branches. Also the Q-branches are nicely visible. I will go in more detail in the later sections of this work.

Chapter 6

Velocity Fields in M-type Stars

In order to investigate the atmospheric structure with focus on the velocity fields present, I used 3D-`CO`^{5}`BOLD` structure models which serve as an input for the line formation program `LINFOR3D`. Turbulence is included in a natural way using hydrodynamics, so that I am able to investigate the modeled spectral lines for effects from micro- and macro-turbulent velocities in the classical sense and their influence on the line shapes. The comparison with 1D-models gives a rough estimate of the necessity of using 3D-models in the spectral domain of cool stars. In this chapter, I investigate the velocity fields in the models and their dependence on $\log g$ and T_{eff}. Most of the content in this chapter is already published in Wende et al. (2009).

6.1 3D Model Atmospheres

6.1.1 `CO`^{5}`BOLD` Atmosphere Grid

In order to analyze the influence of velocity fields in M-stars on FeH lines, I construct a set of `CO`^{5}`BOLD`-models with $T_{\text{eff}} = 2500\,\text{K} - 4000\,\text{K}$ and $\log g = 3.0 - 5.0$ [cgs]. Table 6.1 gives the model parameters. In the T_{eff}-sequence, I simulated main sequence stars and varied the surface gravity slightly with increasing effective temperature. For the $\log g$-sequence, I computed models with different $\log g$ values aiming at the same effective temperature of 3300 K but the models settle to slightly higher or lower T_{eff} values. Because the effective temperature can only be adjusted via the inflowing entropy, I decided not to adjust these resulting effective temperatures, because slight differences in T_{eff} do not change the line profiles significantly. I accepted the T_{eff} deviations to avoid the large computational effort which would be necessary to adjust the models to a common effective temperature. However, corrections to the line shape related quantities such as equivalent width (see Section 7.2) are applied.

The opacities used in the `CO`^{5}`BOLD` model calculations originate from the `PHOENIX` stellar atmosphere package (Hauschildt & Baron, 1999) assuming a solar chemical composition according to Asplund et al. (2005). The opacity tables were computed after Ferguson et al. (2005) and Freytag et al. (2009) and are particularly well-suited for this investigation since they are adapted to very cool stellar atmospheres. The raw data consist of opacities sampled at 62,890 wavelength points for a grid of temperatures and gas pressures. In order to represent the wavelength dependence of the radiation field in the `CO`^{5}`BOLD` models, the opacities are re-sampled into six wavelength groups using the opacity binning method (Nordlund, 1982; Ludwig, 1992; Ludwig et al., 1994). In this approach, the frequencies that reach monochromatic optical depth unity within a certain depth range of the model atmosphere are grouped into one frequency bin on the basis of their opacities. For each investigated atmospheric parameter combination, the sorting of the wavelengths into groups is performed according the run of monochromatic optical depth in a corresponding `PHOENIX` 1D model atmosphere. The thresholds for the sorting are chosen in logarithmic Rosseland optical depth as $\{+\infty, 0.0, -1.0, -2.0, -3.0, -4.5, -\infty\}$. In each group a switching is done from a Rosseland average in the optically thick regime to a Planck average in the optically thin regime, except for the group representing the highest opacities, where the Rosseland average is used throughout. In this last bin, which describes the optically thick regions, only the Rosseland average is used because the radiative transfer is local and can be described as a diffusive process (Vögler et al., 2004). Despite this, the Rosseland opacity is much smaller than the Planck opacity which keeps the radiative time scale large.

The horizontal size of the models provide sufficient space to allow the development of a small number (10–20) of convective cells. Their number has to be large enough to avoid box-size dependent effects, but also small enough that there is a sufficient number of grid points available to resolve each individual cell. The size of the convective cells scales roughly inverse proportionally to the surface gravity. Accordingly, the horizontal size of the computational box is set to larger sizes towards lower $\log g$ values. The horizontal size of the model with $T_{\rm eff} = 3275\,{\rm K}$ is just large enough to fulfill the criteria of the minimal number of 10 convective cells (see Fig. 6.1), and it was seen in test simulations that the results will not change with a larger model (in horizontal size). Therefore I will use this well evolved model as well. The vertical dimension is set to embed the optically thin photosphere, and a number of pressure scale heights of the sub-photospheric layers below. The depth of the models is kept rather small to avoid problems due to numerical instabilities analogous to the ones encountered and discussed in previous works on the hydrodynamics of M-type stellar atmospheres (Ludwig et al., 2002, 2006; Freytag et al., 2010).

For the comparison with 1D models, the 3D-model are spatially averaged over surfaces of equal Rosseland optical depth at selected instants in time. I call this sequence of 1D structures the ⟨3D⟩-model. Following the procedure of Steffen et al. (1995), the fourth moment of the temperature and the first moment of the gas pressure is averaged, in order to preserve the radiative properties of the 3D-model as far as possible. The 3D velocity information is ignored in the ⟨3D⟩-model and replaced by a micro- and macro-turbulent velocity. By construction, the ⟨3D⟩-model has the same thermal profile as the 3D-model, but evidently without the horizontal inhomogeneities related to the convective granulation pattern. I will call the spectral lines synthesized from ⟨3D⟩-models "⟨3D⟩-lines".

6.1.2 Atmosphere Structures

The temperature stratification shown in Fig.6.2 (top left) of the models with changing $T_{\rm eff}$ is very similar for all models in the region below $\log\tau \sim 1$. They reach their $T_{\rm eff}$ around $\tau \sim 2/3$ and continue to decrease to higher atmospheric layers. Above $\log\tau \sim 1$, the temperature of the two hottest models increases more strongly than in the cooler cases. Since the models are almost adiabatic in the deeper layers (see below), the temperature gradient follows the adiabatic gradient, which is given by the equation of state and is steeper in hotter models due to the inefficient H_2 molecule formation. This increase of temperature is also very similar to the lower $\log g$ models shown on the right side of Fig.6.2. These models also show a temperature gradient which becomes steeper towards deeper atmospheric layers and with decreasing surface gravity, again due to a steeper adiabatic gradient. All models reach an almost equal effective temperature at $\tau \sim 2/3$ and their temperature stratification does not differ strongly towards smaller optical

Table 6.1: Overview of different model quantities for models at constant T_{eff} and different $\log g$ (upper part) and at constant $\log g$ and different T_{eff} (lower part).

Model code	Size(x,y,z) [km]	Grid points (nx,ny,nz)	H_p [km][a]	z-size [H_p]	T_{eff} [K]	$\log g$ [cgs]
d3t33g30mm00w1	85000 x 85000 x 58350	180 x 180 x 150	2821	20.7	3240	3.0
d3t33g35mm00w1	28000 x 28000 x 11500	180 x 180 x 150	826	13.9	3270	3.5
d3t33g40mm00w1	7750 x 7750 x 1850	150 x 150 x 150	250	7.4	3315	4.0
d3t33g50mm00w1	300 x 300 x 260	180 x 180 x 150	18	14.5	3275	5.0
d3t40g45mm00n01	4700 x 4700 x 1150	140 x 140 x 141	109	10.6	4000	4.5
d3t38g49mm00w1	1900 x 1900 x 420	140 x 140 x 150	36	11.7	3820	4.9
d3t35g50mm00w1	1070 x 1070 x 290	180 x 180 x 150	20	14.5	3380	5.0
d3t28g50mm00w1	370 x 370 x 270	250 x 250 x 140	13	20.8	2800	5.0
d3t25g50mm00w1	240 x 240 x 170	250 x 250 x 120	12	14.2	2575	5.0

[a] at $\tau = 1$

depth.

The entropy stratification for models with varying T_{eff} (mid left in Fig.6.2) shows a similar behavior for all models. It is adiabatic ($dS/d\tau = 0$) in layers below $\log \tau \sim 1$ and has a superadiabatic region ($dS/d\tau > 0$) between $\log \tau \sim 1$ and ~ -1 that moves slightly towards smaller optical depth for hotter models. In these regions, with $dS/d\tau \geq 0$, the models are convectively unstable and become convectively stable in the outer parts of the atmosphere where $dS/d\tau < 0$. In the models with changing $\log g$ (mid right in Fig.6.2), one can see that the entropy behaves almost as in the T_{eff} case. At lower surface gravities, the superadiabatic region is more significant. In higher layers, the models become convectively stable except for the model with $\log g = 4.0$ [cgs] which shows a second decrease of entropy in the outer layers. To understand this behavior, one has to investigate the adiabatic gradient of this region which is very small and changes very little along the upper atmosphere. This is due to the equation of state used in the models and can be seen in Fig.16 of Ludwig et al. (2006) (model H4 in this figure equates to our $\log g = 4.0$ model). This figure shows that the upper atmosphere lies in a plane of small and constant adiabatic gradient. Due to this, the model becomes convectively unstable again in the upper layers. This is probably the reason for the, higher velocities in this model, in comparison to other models.

In the left bottom panel of Fig.6.2, the horizontal and vertical rms-velocities are plotted for models with different T_{eff}. Both velocity components increase with increasing T_{eff}. The maxima of the vertical velocity moves to slightly deeper layers with higher temperatures and the maxima of the horizontal velocity stays almost at the same optical depth. One can see a qualitatively similar dependence in the $\log g$ model sequence in the right bottom plot in Fig.6.2. Only the model with $\log g = 4.0$ [cgs] shows peculiar behavior in the upper atmospheric layers, which is probably related to the entropy stratification in this model. The velocity fields in the models will be described in more detail and with a slightly different method in the next section.

6.2 Velocity Fields in the CO^{5}BOLD-Models

Before the investigation of the effect of velocity fields on spectral lines, it is useful to analyze the velocity fields in the models themselves and this will be done in a description relative to the broadening of spectral lines. Spectral lines are broadened by velocity fields where the wavelength of absorption or emission of a particle is shifted due to its motion in the gas. Here one is mostly concerned with the macroscopic, hydrodynamic motion but one should has in mind that thermal motion also constitutes a significant contribution. If each voxel in the RHD model cube is considered to form its own spectral line, the whole line consists of a (weighted) sum of single lines. The velocity distribution might be represented by a histogram of the velocities of the voxels which gives us the velocity dispersion. It is tried to describe the velocity fields in that sense instead of using the rms-velocities shown in Fig.6.2. In the `CO`^{5}`BOLD`-models, a velocity vector is assigned to each voxel and consists of the velocities in the x-, y-, and z-direction. I will investigate the vertical and horizontal component of the velocity dispersion in the models and the total velocity dispersion $\sigma_{\mathrm{tot}} = \sqrt{\sigma_x^2 + \sigma_y^2 + \sigma_z^2}$. In order to describe the height-dependent velocity dispersion, I applied a binning method, i.e. I plot all velocity components of a certain horizontal plane of

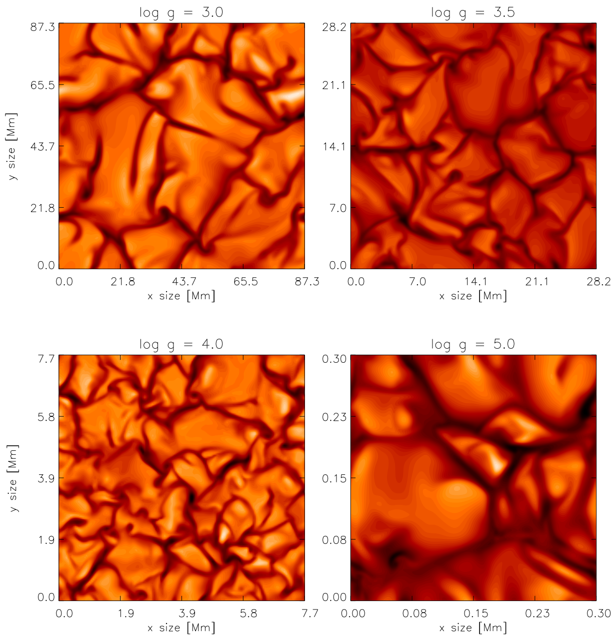

Figure 6.1: Horizontal cross-section around $\tau \sim 1$ of vertical velocity components. The models are located at $\log g$ values of 3.0, 3.5, 4.0, and 5.0 [cgs] (from upper left corner to lower right, respectively).

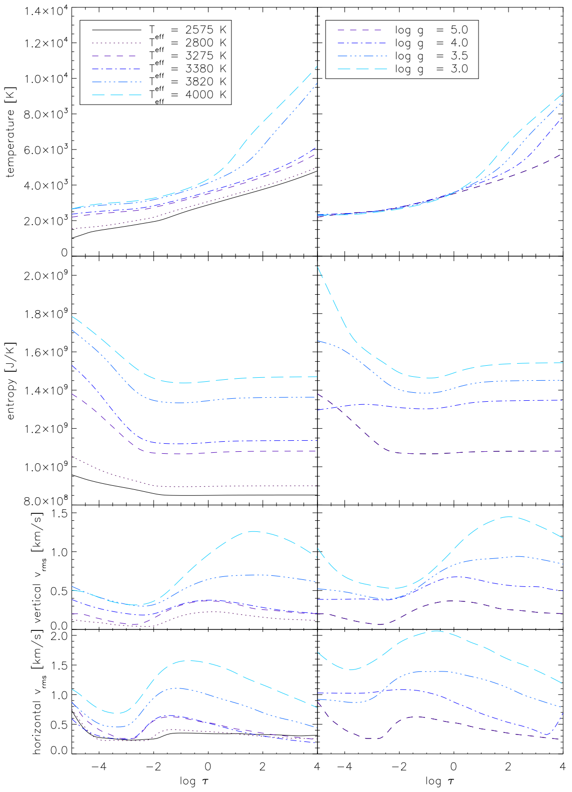

Figure 6.2: From top to bottom, the temperature, entropy, vertical, and horizontal velocity are plotted as a function of optical depth. The column on the left side shows models with different T_{eff} and constant $\log g$, on the right side the models are at a constant T_{eff} with varying $\log g$. The rise of horizontal velocity in the $\log g = 4.0$ [cgs] model in the deeper atmospheric layers is due to interpolation from the z- to τ-scale.

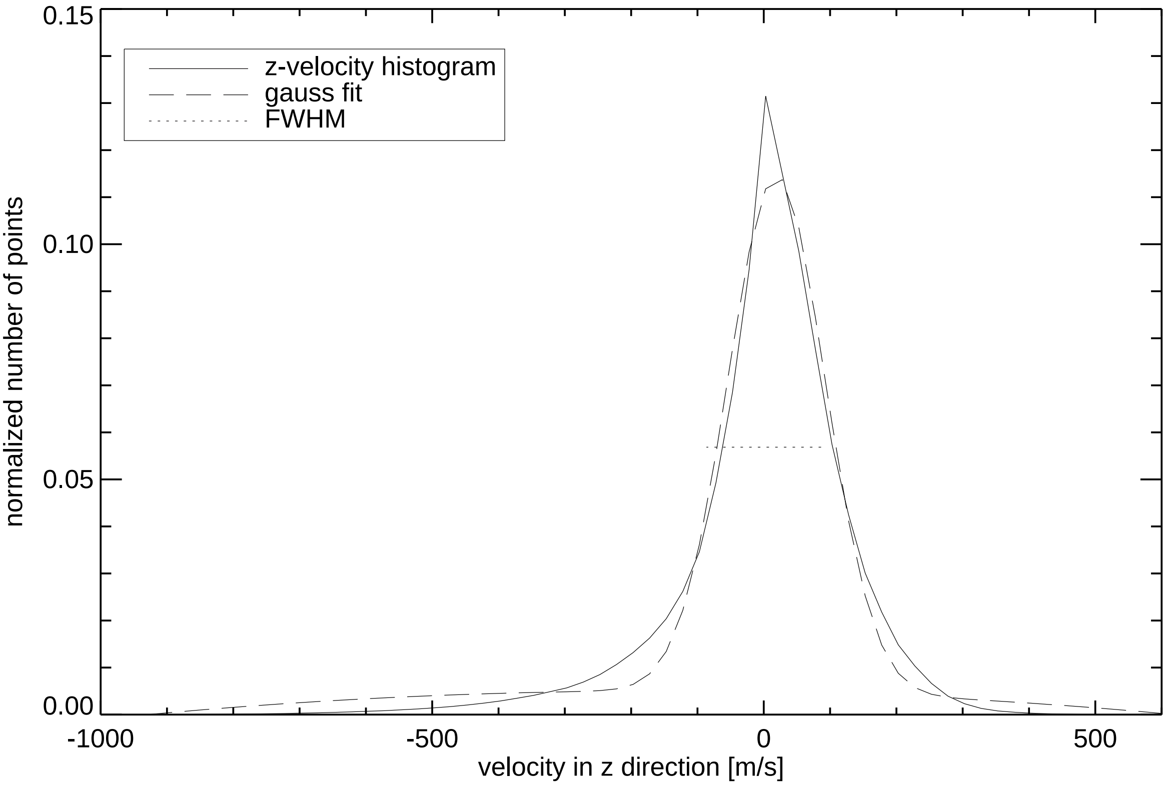

Figure 6.3: Histogram of the velocity distribution in the vertical direction. The normalized number of points is plotted against the vertical velocity in m/s (solid line). The Gaussian (dashed line) fits the velocity distribution and determined an FWHM value (dashed-dotted line), which is related to σ with $FWHM = 2\sqrt{\ln 2} \cdot \sigma$. The underlying model is located at $T_{\text{eff}} = 2800\,\text{K}$ and $\log g = 5$ [cgs].

equal optical depth τ in the CO^{5}BOLD cube in a histogram with a bin size of $25\,\text{m}\,\text{s}^{-1}$.

I fit the histogram velocity distribution with a Gaussian normal distribution function $G = \exp\left(-(\frac{x}{\sigma})^2\right)$ and take the standard deviation σ as a measure for the velocity dispersion σ in the models (see Fig. 6.3) (The relation between the Gaussian standard deviation σ and the standard deviation σ_{rms} of the mean velocity is $\sigma = \sqrt{2}\cdot\sigma_{\text{rms}}$). This is done for the σ_x, σ_y, and σ_z component of the velocity vector for each horizontal plane from τ_{min} to τ_{max}, which are the highest and the deepest point, in each model atmosphere. In this way I obtained the height-dependent velocity dispersion $\sigma_{x,y,z}(\tau)$. I average over five model snapshots for a better statistical significance. In Figs. 6.4 and 6.5, the velocity dispersions for the horizontal components $\sigma_{\text{H}} = \sqrt{\sigma_x^2 + \sigma_y^2}$ and vertical component σ_z are plotted against optical depth (black solid and dotted lines). In the latter figures, I identify the maxima around $\log\tau = -1$ of the velocity dispersions as the region where the up-flowing motion spreads out in the horizontal direction and starts to fall back to deeper layers. I will call this point the "convective turn-over point". In a horizontal 2D cross-section of the vertical velocities, somewhat below this area, the up-flowing granulation patterns are clearly visible (see Fig.6.1 for models with different $\log g$ or Ludwig et al. (2006)). In a vertical 2D cross-section one can see the behavior of the up-streaming material (Fig. 6.6 shows an example

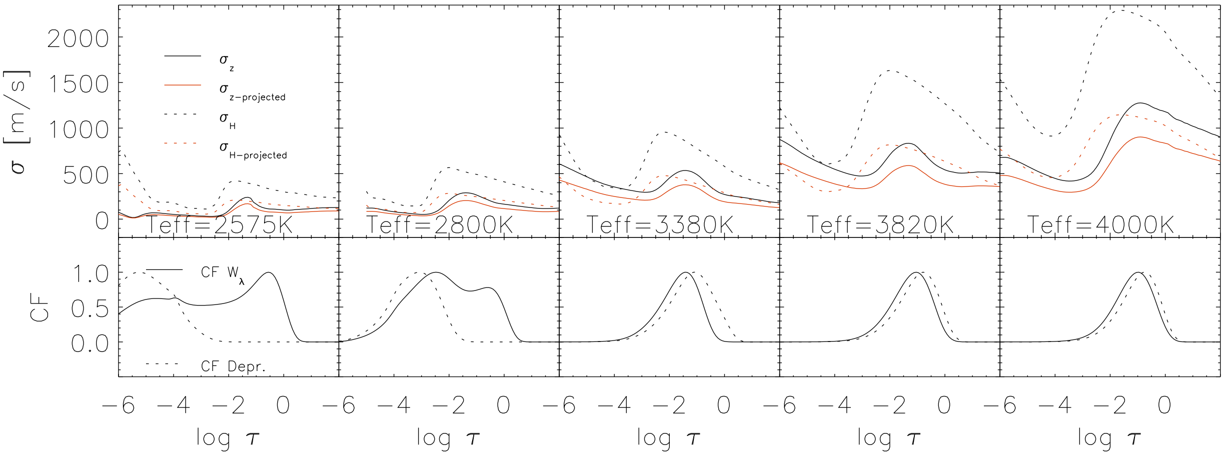

Figure 6.4: Upper panel: Radial (σ_z) and horizontal (σ_H) components of the velocity dispersion plotted against the optical depth on a logarithmic scale. Bottom panel: The contribution functions (CF) of an FeHline at a wavelength of 9956.72 . Equivalent width W_λ (solid) and the depression at the line center (dashed) of the line are plotted as a function of optical depth on a logarithmic scale. The models (from left to right) are located at T_{eff} of 2800 K, 3380 K, 3820 K and 4000 K and a $\log g$ value of 5.0, except the one with $T_{\text{eff}} = 3820$ K ($\log g = 4.9$), and the one with $T_{\text{eff}} = 4000$ K ($\log g = 4.5$) [cgs].

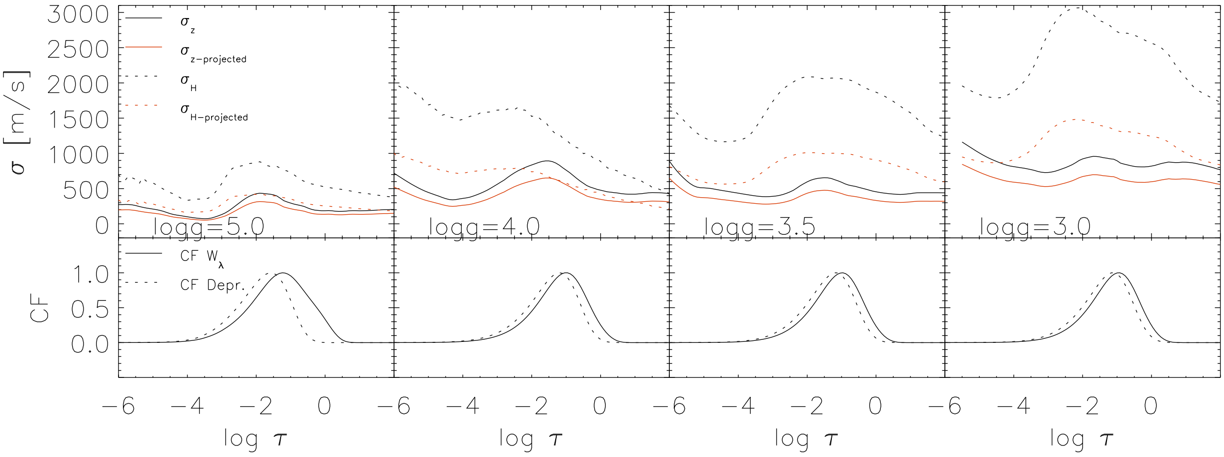

Figure 6.5: Upper panel: Radial (σ_z) and horizontal (σ_{H}) components of the velocity dispersion plotted against the optical depth on a logarithmic scale. Bottom panel: The contribution functions (CF) of an FeHline at a wavelength of 9956.72 . Equivalent width W_λ (solid) and the depression at the line center (dashed) of the line are plotted as a function of optical depth on a logarithmic scale. The models are located at $\log g$ values from left to right of 5.0 ($T_{\text{eff}} = 3275$ K), 4.0 ($T_{\text{eff}} = 3315$ K), 3.5 ($T_{\text{eff}} = 3270$ K) and 3.0 ($T_{\text{eff}} = 3240$ K) [cgs].

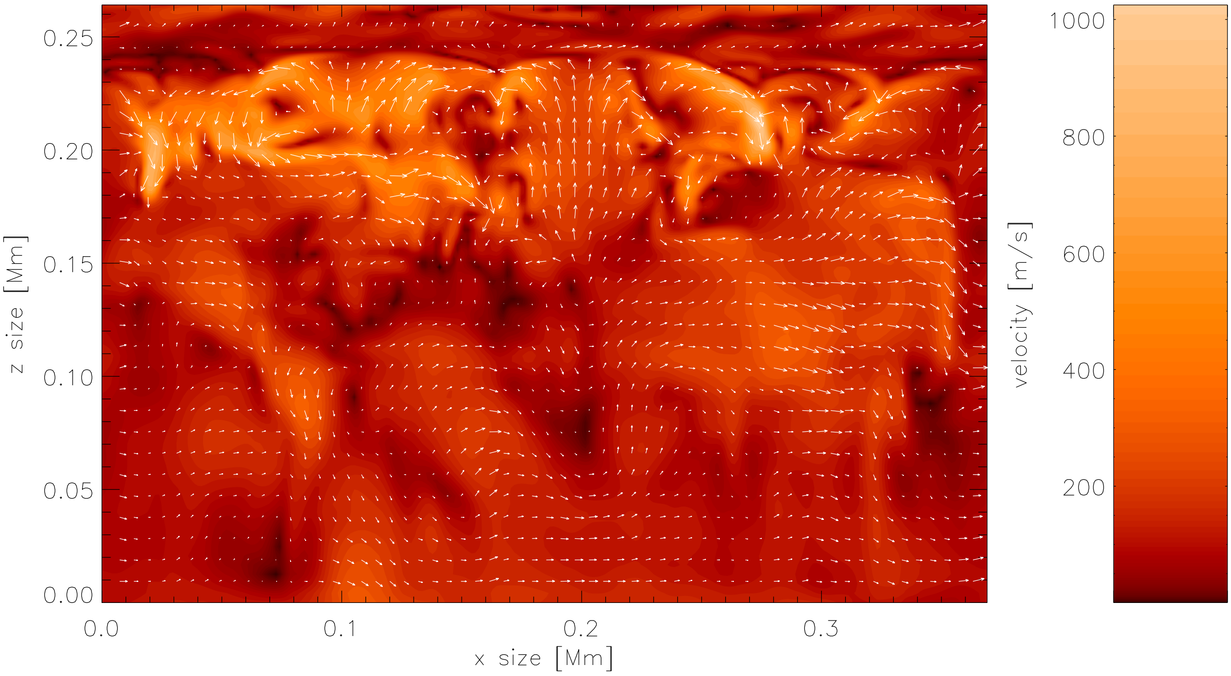

Figure 6.6: 2D cross-section in x-z direction of the x-z velocity in a model with $\log g = 5.0$ [cgs] and $T_{\rm eff} = 2800\,$K. Overplotted are x-z velocity vectors. The direction of the material flow is indicated by the velocity vectors.

for a model with $T_{\rm eff} = 2800\,$K). The material starts moving upwards almost coherently and before reaching higher layers (around $z = 200$ km in Fig. 6.6) of the atmosphere, the vertical velocity dispersion σ_z becomes maximal. After that point, the material spreads out in horizontal directions and starts falling again. At this point, the dispersion of horizontal velocities σ_H becomes maximal (the convective turn-over point).

In Fig.6.5 one can see at lower surface gravities that the maxima of the horizontal velocity dispersion are not centered around a specified optical depth any longer; it spreads out in the vertical direction and spans the widest range at $\log g = 3.0$ [cgs]. The pressure stratification changes, and the convective turn-over point moves to lower gas-pressure (not shown here) but stays at almost constant optical depth between $\log\tau = 0$ and $\log\tau = -2$. With varying temperature, the position of the convective turn-over point stays at almost constant optical depth.

6.2.1 Reduction of the 3D Velocity Fields

Commonly, micro- and macro-turbulence derived from spectroscopy are interpreted as being associated with actual velocity fields present in the stellar atmosphere. In the simulations, no oscillations are induced externally but small oscillations are generated in the simulations itself. The velocity amplitudes of these oscillations reach a maximum of 10 % of the convective velocities and have no significant influence on the macro-turbulent velocity. I would also not expect

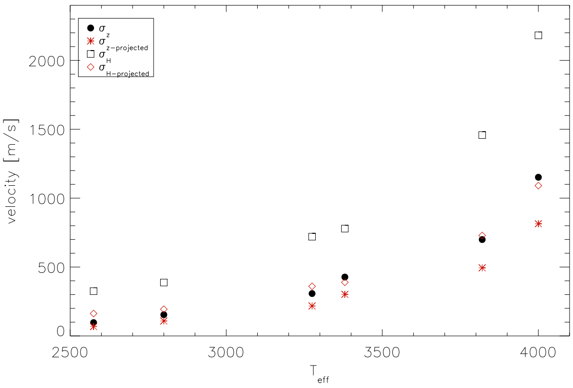

Figure 6.7: The weighted projected and unprojected velocity dispersions of the horizontal and vertical component for models with different $T_{\rm eff}$. The models are located at $T_{\rm eff}$ values of 2575 K, 2800 K, 3275 K, 3380 K, 3820 K and 4000 K and a $\log g$ value of 5.0, except the one with $T_{\rm eff} = 3820\,$K ($\log g = 4.9$), and the one with $T_{\rm eff} = 4000\,$K ($\log g = 4.5$) [cgs].

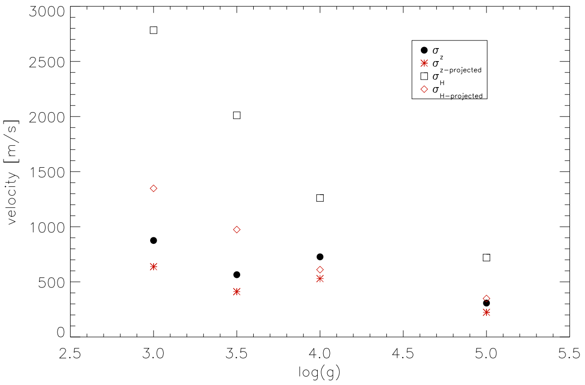

Figure 6.8: The weighted projected and unprojected velocity dispersions of the horizontal and vertical component for models with different $\log g$. The models are located at $T_{\rm eff}$ around $3300K$ and different $\log g$ values of 3.0 ($T_{\rm eff} = 3240\,$K), 3.5 ($T_{\rm eff} = 3270\,$K), 4.0 ($T_{\rm eff} = 3315\,$K) and 5.0 ($T_{\rm eff} = 3275\,$K) [cgs].

global oscillations for these objects, except for young stars with solar masses lower than 0.1 $M_\odot$ induced by D-burning (Palla & Baraffe, 2005). In the following, I try to make the connection between micro- and macro-turbulence and actual hydrodynamical velocity fields by considering the velocity dispersion determined directly from the hydrodynamical model data, and comparing it with the micro- and macro-turbulence derived from synthesized spectral lines (see Sect. 6.2.3). This connection is algebraically not simple, and I only apply a simple model to translate the hydrodynamical velocities into turbulent velocities relevant to spectroscopy.

Geometrical Projection

To compare the hydrodynamical velocity dispersion in 3D-`CO`^{5}`BOLD` models with the spectroscopic quantity micro- and macro-turbulent velocities, I assume a simple geometrical model and try to resample the broadening of absorption lines. An intensity beam “sees” the velocity field under a certain angle and the spectral line is broadened by the projection of these velocities. In this sense I project the geometrical velocity components on a line of sight under a certain angle and integrate over all angles in a half sphere. I also take a linear limb-darkening law into account. I assume a velocity function $f(v)$ in velocity space and an intensity line profile

$$I(v) = V(v) \cdot I_c^0 \cdot L(\theta), \tag{6.1}$$

where $V(v)$ is a line profile function, I_c^0 the continuum intensity at the center of the disk and $L(\theta)$ the limb-darkening law. The integrated flux of the intensity line profile broadened by the velocity function is then given by their convolution and disk integration, i.e.

$$F = \oint f(v) * I(v) \cos\theta \; d\omega, \tag{6.2}$$

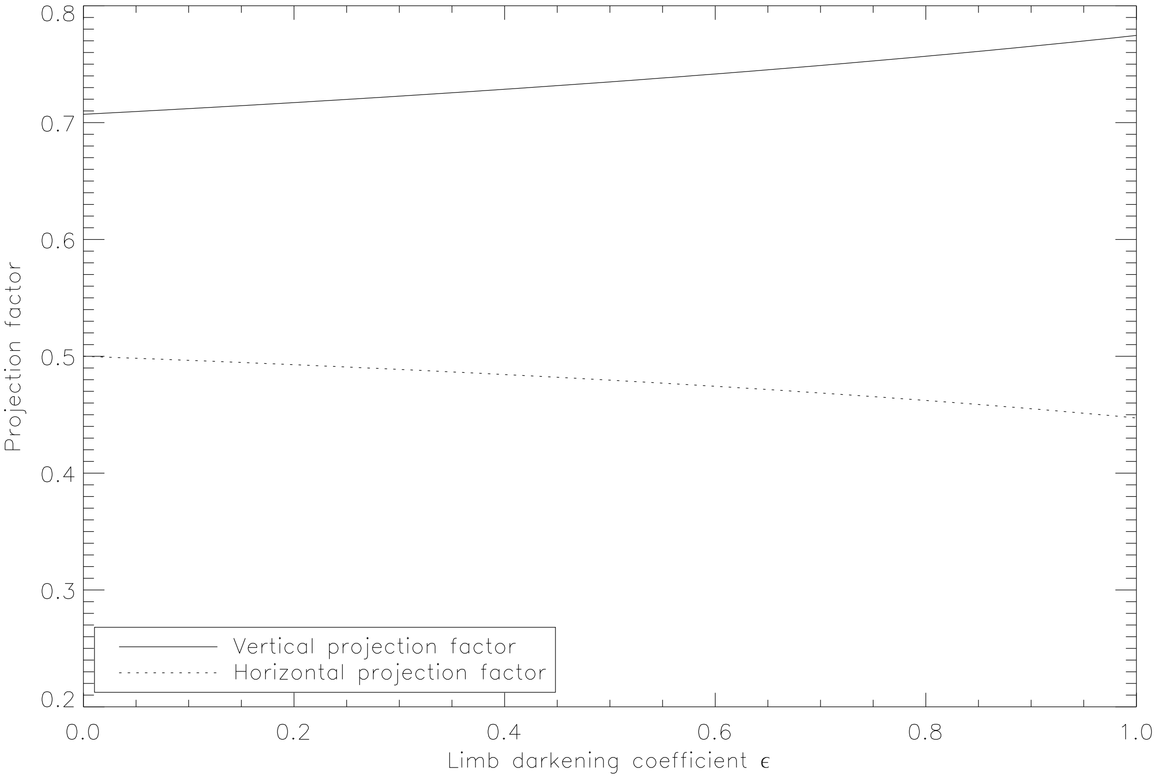

Figure 6.9: Projection factors (vertical solid line and horizontal dotted line) as a function of the limb darkening coefficient ϵ.

with $d\omega = \sin\theta \; d\theta \; d\phi, \; \phi \in [0, 2\pi], \; \theta \in [0, \pi/2]$. If I assume that $V(v)$ does not vary with different positions on the disk, it can be factored out (Gray, 2008) and

$$F = V(v) * I_c^0 \cdot W(v), \tag{6.3}$$

with

$$W(v) = \oint f(v) \cdot L(\theta) \cos\theta \; d\omega. \tag{6.4}$$

With Eq. 6.4 one is left with a flux-like expression for the velocity function. The dispersion of the velocity function is given by

$$\sigma^2 = \langle f(v)^2 \rangle - \langle f(v) \rangle^2 \tag{6.5}$$

and one can write for the projected velocity dispersion Σ:

$$\Sigma^2 = \frac{1}{N} \int_0^{2\pi} \int_0^{\pi/2} (\langle (f(\vec{v})\vec{e})^2 \rangle - \langle f(\vec{v})\vec{e} \rangle^2) \cdot L(\theta) \;\; \cos\theta \; d\omega \tag{6.6}$$

where $f(\vec{v}) = \begin{pmatrix} f_x(v) \\ f_y(v) \\ f_z(v) \end{pmatrix}$ is the velocity vector containing all velocities in a model cube, $\vec{e} = \begin{pmatrix} \cos\phi\sin\theta \\ \sin\phi\sin\theta \\ \cos\theta \end{pmatrix}$ is the basis vector in spherical coordinates, and $L(\theta) = 1 - \epsilon + \epsilon \cdot \cos(\theta)$ a linear limb-darkening law with the limb-darkening coefficient ϵ. N is a normalization factor $N = \int_0^{2\pi} d\phi \int_0^{\pi/2} L(\theta)\ \cos\theta\ \sin\theta\ d\theta = \pi(1 - \frac{\epsilon}{3})$. I included the limb-darkening in the normalization because, opposite to the flux, the velocity dispersion for an isotropic velocity field has to be conserved. The average is taken over the velocities and does not affect the angle dependent parts. One has to integrate:

$$\begin{aligned} \langle(\vec{f}\vec{e})^2\rangle - \langle\vec{f}\vec{e}\rangle^2 = (\langle f_x^2\rangle - \langle f_x\rangle^2)\cos\phi^2\sin\theta^2 + \\ (\langle f_y^2\rangle - \langle f_y\rangle^2)\sin\phi^2\sin\theta^2 + (\langle f_z^2\rangle - \langle f_z\rangle^2)\cos\theta^2 + \\ 2(\langle f_x f_y\rangle - \langle f_x\rangle\langle f_y\rangle)\cos\phi\sin\phi\sin\theta^2 + \\ 2(\langle f_x f_z\rangle - \langle f_x\rangle\langle f_z\rangle)\cos\phi\sin\theta\cos\theta\quad + \\ 2(\langle f_y f_z\rangle - \langle f_y\rangle\langle f_z\rangle)\sin\phi\sin\theta\cos\theta. \end{aligned} \tag{6.7}$$

If one wants to compute the average of this quantity, the mean and the squared mean of the quantities are needed, but not the combinations of the velocity components, because these products vanish in the integration over the half sphere due to their angle-dependent coefficients. After the integration of Eq.6.6, Σ^2 becomes

$$\begin{aligned} \Sigma^2 = \frac{(\langle f_x^2\rangle - \langle f_x\rangle^2 + \langle f_y^2\rangle - \langle f_y\rangle^2)(7\epsilon - 15)}{20(\epsilon - 3)} + \\ \frac{(\langle f_z^2\rangle - \langle f_z\rangle^2)(6\epsilon - 30)}{20(\epsilon - 3)}. \end{aligned} \tag{6.8}$$

One can see, that for an isotropic velocity field $f_x(v) = f_y(v) = f_z(v) = f(v)$ follows that $\Sigma^2 = \sigma^2\langle f(v)^2\rangle - \langle f(v)\rangle^2$ and does not depend on ϵ or the geometrical projection any longer. Setting $\epsilon = 0$, it then follows from Eq. 6.8 that $\Sigma^2_{x,y} = \frac{1}{4}\sigma^2_{x,y}$ and $\Sigma^2_z = \frac{1}{2}\sigma^2_z$ due to geometrical effects.

The projection factors for the vertical $\left(\frac{6\epsilon-30}{20(\epsilon-3)}\right)$ and horizontal $\left(\frac{7\epsilon-15}{20(\epsilon-3)}\right)$ component are plotted as a function of the limb-darkening coefficient ϵ in Fig. 6.9. They vary only about 5% from no darkening to a full darkened disk. The reduction for the vertical velocity is about 30% and for the horizontal components 50%.

For completeness, one can obtain in a similar way the mean velocities in three spatial directions $\langle f_{x,y,z}(v)\rangle$ which are given by

$$\langle f_{x,y,z}(v)\rangle_{projected} = \frac{1}{N}\int_0^{2\pi}\int_0^{\pi/2} \langle \vec{f}_{x,y,z}(v)\vec{e}\rangle \cdot L(\theta)\ \cos\theta\ d\omega. \tag{6.9}$$

The horizontal velocities vanish due to projection but there is still a vertical component which is reduced to geometrical and limb-darkening effects.

$$\begin{aligned} \langle f_x(v)\rangle_{projected} &= \langle f_y(v)\rangle_{projected} = 0, \\ \langle f_z(v)\rangle_{projected} &= \frac{(\epsilon - 4)}{2(\epsilon - 3)}\langle f_z(v)\rangle. \end{aligned} \tag{6.10}$$

When interpreting the comparisons shown below, the very approximate nature of this model should be kept in mind. In this model, I include the geometric projection of the components of $\sigma_{x,y,z}$ to the line of sight of the observer. One also has to consider the effect of limb-darkening of the stellar disk. For each velocity dispersion component, I calculate the projection factor which includes both geometrical projection and limb-darkening effects. I take a limb-darkening coefficient of 0.4 which follows from the continuum from the angle dependent line synthesis performed in `LINFOR3D`. These simulations suggest that a linear limb-darkening law with a limb-darkening coefficient of 0.4 is suited to describe the brightness variation. The projected velocity dispersions are also plotted in Figs. 6.4 and 6.5 (red solid and dotted lines). The reducing effect of this projection factor is stronger in the horizontal components than in the vertical because the projected area at the limb of the stellar disk, where σ_H reaches its maximum value, is much smaller than in the center where σ_z has its maximum value. The influence of limb-darkening is not strong and the dependence of the projection factor from the limb-darkening coefficient is only small (see Fig. 6.9).

Weighted Velocities

To investigate the influence of broadening from the projected and unprojected velocity dispersion on spectral lines, I use contribution functions for the equivalent width W_λ and the depression at the line center of an FeH line at 9956.7 (Magain, 1986). The line gains its W_λ and depression in the region between $\log\tau = 1.0$ and $\log\tau = -4.0$, i.e. that is the region of main continuum absorption caused by FeH molecules. The maximum is roughly centered around $\log\tau = -1.0$ and moves to slightly lower optical depth with lower temperatures (at the lowest T_{eff} of 2575 K, the maximum is centered around $\log\tau = -2.0$) or higher surface gravities. The contribution function of W_λ ranges over the region of the convection zone and reflects its influence on the line shape. Due to the latter fact, FeH lines are a good means to explore the convective regions in M-dwarfs. In order to measure the velocities in the region where the lines originate, I compute the mean of the (projected) velocities weighted by the contribution function of W_λ.

$$\sigma_{\mathrm{weighted}} = \frac{\sum_{\tau=2}^{-6} \sigma_\tau \cdot CF_\tau}{\sum_{\tau=2}^{-6} CF_\tau}. \tag{6.11}$$

The horizontal and vertical components of these weighted velocity dispersions are plotted in Figs. 6.7 and 6.8. One can see an increase of $\sigma_{H,z}$ with increasing effective temperature or decreasing surface gravity. One can see again that the projected horizontal velocity dispersions are significantly smaller than the unprojected ones due to the reasons mentioned above. The difference in the vertical component is much smaller. The velocity dispersions for the vertical component range from a few hundred m/s for cool, high gravity models to $\sim 1\,\mathrm{km\,s^{-1}}$ for hot or low gravity models. The horizontal component range from $\sim 500\,\mathrm{m\,s^{-1}}$ for cool, high gravity models to $\sim 2\,\mathrm{km\,s^{-1}}$ for hot or low gravity models. I compare the total projected velocity dispersion $\sigma_{tot} = \sqrt{\sigma_H^2 + \sigma_z^2}$ in Sec. 3.2 with micro- and macro-turbulent velocities in the classical sense.

The strong increase of the velocity dispersions in the atmospheres to higher layers (Figs. 6.4 and 6.5) which some models show is related to convective overshoot into formally stable layers. These velocities are generated by waves excited by stochastic fluid motion and by advective motion (Ludwig et al., 2002, and references therein). However, it will not affect the spectral lines, because the lines are generated in the region between an optical depth of $\log\tau = 1.0$ and $\log\tau = -4.0$. The lines in the model with $T_{\mathrm{eff}} = 2575\,\mathrm{K}$ are an exception, they are formed in the outermost

Table 6.2: Displacement Δv_{Flux} and $\Delta v_{\mathrm{Intensity}}$ in m/s of the position of an FeH line from the rest wavelength in models with different T_{eff} (left side) and different $\log g$ (right side).

T_{eff}	Δv_{Flux} [m/s]	$\Delta v_{\mathrm{intensity}}$ [m/s]	v_{ad} [m/s]	$\log g$	Δv_{Flux} [m/s]	$\Delta v_{\mathrm{intensity}}$ [m/s]	v_{ad} [m/s]
2800	0	2	3750	3.0	−56	−25	6100
3275	−1	3	4000	3.5	−47	−36	5500
3380	−2	2	4850	4.0	−16	−7	5400
3820	−1	−5	6000	5.0	−1	3	4500
4000	−44	−28	7000				

layers of the model and it is not possible to compute the full range of formation of these lines, because the atmosphere is not extended enough. One has to keep this in mind when regarding the line dependent results of this model later in this chapter.

6.2.2 Radial Velocity Shifts

Due to the fact that in convective motion the up-flowing area is larger, because it is hotter and less dense than the down-flowing one, one expects a net shift of the velocity distribution to positive velocities. That means the net amount of up-flowing area with hotter temperature, i.e. more flux in comparison to the down-flowing area, results in a blue shift in the rest wavelength position of a spectral line (see e.g. Dravins, 1982).

To see how the area of up-flowing material affects the rest wavelength position of a spectral line, ten FeH lines are computed (described in Sect. 4) in 3D models to measure the displacement of the line positions. In order to determine the center of the line, I used the weighted mean $C = \frac{\sum F \cdot v}{\sum F}$ which accounts for the asymmetric line shape. (To use the weighted mean is appropriate here since there is no noise in the computed data.) The line shifts of the flux and the intensity are given in Table 6.2. A negative value stands for a blue shift, and a positive for a red shift. The values for each model are the mean of five temporal snapshots. The absolute displacement of the flux and intensity in the $\log g$ series reflects the dependence of the velocity fields on surface gravity, but for the T_{eff} series a connection is barely visible (see Figs. 6.7 and 6.8). This could be due to the small geometrical size of the atmospheres in the T_{eff} series (see Table 6.1). Only the the one with $T_{\mathrm{eff}} = 4000\,\mathrm{K}$ shows a significant line shift and in this model the atmosphere is 1150 km high due to the slightly smaller $\log g$ value of 4.5 [cgs]. At this point I will not continue with a deeper analysis of this topic.

Since only five snapshots are used, one is dealing with statistics of small numbers and hence a large scatter in the results. This scatter σ_{shift} is in general one order lower than the shift of the line and the integrated jitter of the line, which is important for radial-velocity measurements, scales as $\sigma_{\mathrm{jitter}} = \frac{\sigma_{\mathrm{shift}}}{\sqrt{N}}$, where N is the number of snapshots. Since in a star N is of the order of 10^6, the jitter will be of the order of $\mathrm{mm\,s^{-1}}$.

I did not further investigate the effect of granulation patterns on the line profiles but, as it will be seen below, the lines are almost Gaussian and show no direct evidence for significant granulation effects.

6.2.3 Micro- and Macro-Turbulent Velocities

Due to the large amount of CPU time required to compute 3D RHD models and spectral lines in these models, I study the necessity of 3D models in the range of M-stars. My goal is to compare the broadening effects of the 3D velocity fields on the shape of spectral lines with the broadening in terms of the classical micro- and macro-turbulence profiles (see e.g. Gray, 1977, 2008). The latter description is commonly used in 1D atmosphere models like `ATLAS9` (Kurucz, 1970) or `PHOENIX` and related line formation codes. If the difference between 1D and 3D velocity broadening is small, the usage of fast 1D atmosphere codes to simulate M-stars for comparison with observations, e.g. to determine rotational- or Zeeman-broadening, would be an advantage.

If the size of a turbulent element is small compared to unit optical depth, one is in the regime of micro-turbulence. The micro-turbulent velocities might differ strongly from one position to another and have a statistical nature. The broadening effect on spectral lines can be described with a Gaussian which enters the line absorption coefficient (Gray, 2008). It can be treated similarly to the thermal Doppler broadening. The effect on the shapes of saturated lines is an enhancement of line wings due to the fact that at higher velocities the absorption cross section increases and as a consequence the equivalent width (W_λ) of the line is increased.

If the size of a turbulent element is large compared to unit optical depth (or of the same size), one is in the regime of macro-turbulence. This can be treated similarly to rotational broadening as a global broadening of spectral lines. The effect is an increase of the line width but the equivalent width remains constant.

As it was seen before, the velocity fields in M-stars are not very strong in comparison to the sound speed (see Table6.2) and one could expect that their influence on line shapes does not deviate strongly from Gaussian broadening.

I compared line broadening with the radial-tangential profile from Gray (1975) and a simple Gaussian profile and found that the latter is a good approximation with an accuracy high enough for determination of rotational- or Zeeman-broadening. Hence, in this investigation I will assume Gaussian broadening profiles. That means, that we can assume a height-independent isotropic velocity distribution for micro- and macro-turbulent velocities. This is a very convenient way to simulate the velocity fields. One would expect that the anisotropic nature and the height dependence of the hydrodynamical velocity fields have a significant influence on line shapes, so it is remarkable that their influence on spectral lines can be described with high accuracy in this way (at least in the investigated M-type stars). In Fig. 6.10, a few examples of ⟨3D⟩-FeH spectral lines are plotted, which were computed with a given micro-turbulent velocity (determined below) and then convolved with a Gaussian broadening profile with a given macro-turbulent velocity. The broadened ⟨3D⟩-FeH lines fit the 3D-FeH lines very well. The difference in the 1D and 3D centroid ($C = \frac{\sum F \cdot v}{\sum F}$) is of the order of m/s for small velocity fields up to $30 - 40\,\mathrm{m\,s^{-1}}$ for strong velocity fields in hot M star models or with low $\log g$. The error in flux is less than 1% (see Fig. 6.10); this corresponds to an uncertainty in velocity, for example rotational velocity, of less than $150\,\mathrm{m\,s^{-1}}$ depending on the position on the line. It is also visible in Fig.6.10 that at low effective temperature, effects from velocity broadening are not visible in comparison with an unbroadened ⟨3D⟩-line in which the van de Waals broadening is dominant. At higher effective temperatures, the difference between broadened and unbroadened ⟨3D⟩-lines is clearly visible. I found that in the range of M-type stars, 1D spectral synthesis of FeH-lines using micro- and macro-turbulent velocities in the classical description is sufficient to include the effects of the velocity fields. In the following I will determine the velocities needed.

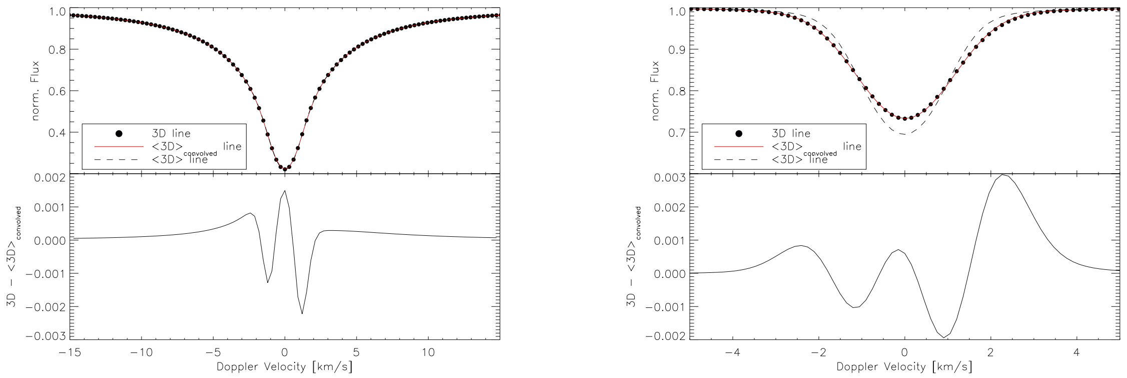

Figure 6.10: FeH lines for models with $T_{\text{eff}} = 2800\,\text{K}$, $\log g = 5.0$ [cgs] (top) and $T_{\text{eff}} = 3820\,\text{K}$, $\log g = 4.9$ [cgs] (bottom). The upper panels show the 3D-line (dots) and the $\langle 3\text{D}\rangle_{\text{convolved}}$-line (solid line) broadened by a Gaussian profile. For comparison a ⟨3D⟩-line which was not broadened by any velocities (dashed line) is plotted. In the lower panels the 3D-$\langle 3\text{D}\rangle_{\text{convolved}}$ residuals are plotted. One can see the asymmetry which stems from the line shifts due to convective motion. Note the different y-axis scale.

Determination of Micro- and Macro-Turbulent Velocities

Investigation of the micro-turbulent velocities was done with the *curve of growth* (CoG) method (e.g., Gray, 2008). We artificially increase the line strength of an absorption-line (increase the $\log gf$ value), which in turn increases the saturation of the line and its influence on the micro-turbulent velocity, which results in an enhancement of W_λ. In order to determine micro-turbulent-velocities, I use Fe I- and FeHlines produced in ⟨3D⟩-models with different micro-turbulent velocities (there are no differences in micro-turbulent velocities between either type of line), i.e. for each $\log gf$-value we compute a ⟨3D⟩-line with micro-turbulent velocities between $0\,\text{km}\,\text{s}^{-1}$ and $1\,\text{km}\,\text{s}^{-1}$ in $0.125\,\text{km}\,\text{s}^{-1}$ steps. In this way CoGs for 9 different micro-turbulent velocities are obtained. I compare the equivalent widths in the CoGs with the ones computed in the 3D-models and selected the velocity of the CoG which fits the 3D CoG best in the sense of χ^2-residuals. Since

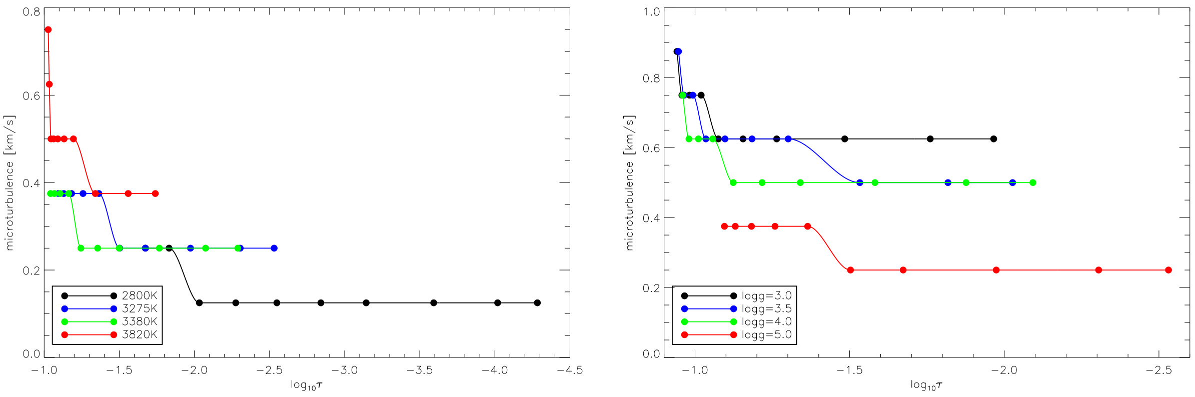

Figure 6.11: Micro-turbulent velocities as a function of $\log \tau$ for different T_{eff} (left) and different $\log g$ (right).

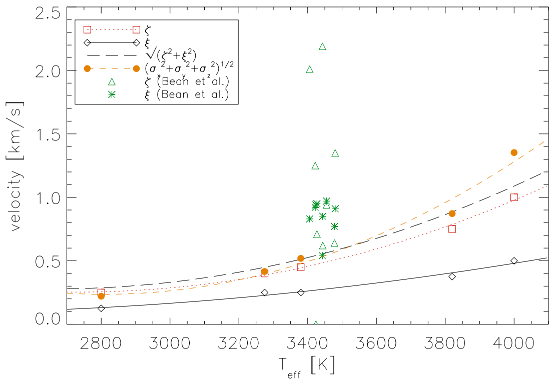

Figure 6.12: Macro- (solid) and micro- (dotted) turbulent velocities and the sum of both (long dashed line) as a function of T_{eff}. The data points are fitted by a second order polynomial and the sum of micro- and macro-turbulent velocities is given by the sum of the fits. For comparison, velocities from Bean et al. and the total projected weighted 3D velocity dispersions are plotted, too (short dashed line). The models are located at T_{eff} values of 2800 K, 3275 K, 3380 K, 3820 K and 4000 K and a $\log g$ value of 5.0, except the one with $T_{\mathrm{eff}} = 3820$ K ($\log g = 4.9$), and the one with $T_{\mathrm{eff}} = 4000$ K ($\log g = 4.5$) [cgs].

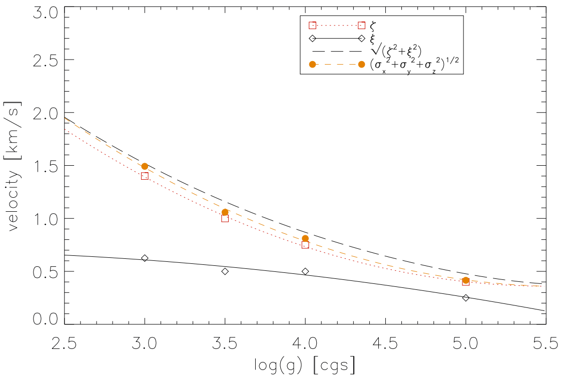

Figure 6.13: Macro- (solid) and micro- (dotted) turbulent velocities and the sum of both (long dashed line) as a function of $\log g$. The data points are fitted by a second order polynomial and the sum of micro- and macro-turbulent velocities is given by the sum of the fits. For comparison, the total projected weighted 3D velocity dispersion is plotted (short dashed line). The models are located at T_{eff} around 3300 K and different $\log g$ values of 3.0 ($T_{\mathrm{eff}} = 3240$ K), 3.5 ($T_{\mathrm{eff}} = 3270$ K), 4.0 ($T_{\mathrm{eff}} = 3315$ K) and 5.0 ($T_{\mathrm{eff}} = 3275$ K) [cgs].

strong (saturated) lines tend to be formed in the upper atmosphere, and weak (unsaturated) lines in deeper layers of the atmosphere, $\log gf$ and the height of formation are related. I fit a micro-turbulent velocity to each $\log gf$ point of the 3D CoG, and convert the $\log gf$ value into a mean optical depth τ, using again contribution functions (see equation (6.11) with τ instead of σ). In this way, a height-dependent micro-turbulent velocity structure was obtained (see Fig.6.11). One can see that both, $\log g$ and T_{eff}sequence, show decreasing velocities towards outer layers. This behavior seems to coincidate more with the vertical hydrodynamical velocity field than with the horizontal field (see Figs. 6.4 and 6.5). However, one has to be careful, since the optical depth is a weighted mean over the range of formation. The influence from micro-turbulent motion is more significant in the line core than in the line wings, which are formed in deeper layers than the core. Hence, in order to investigate the region of significant influence from micro-turbulent motion, one has to shift the derived mean optical depth towards higher atmospheric layers.

The macro-turbulent velocities are determined by computing a ⟨3D⟩-model FeH line (at $\lambda =$ 9956.7) including the micro-turbulent velocities. This line is then broadened with a Gaussian profile and different velocities until it matches the 3D-model line.

The dependence of the micro- (ξ) and macro- (ζ) turbulent velocities on surface gravity and effective temperature is plotted in Figs. 6.12 and 6.13. The macro-turbulent velocities in both cases show a quadratic dependence, and can be fitted with a second order polynomial. The micro-turbulent velocities could be fitted by a linear function or a second order polynomial. I decided to use the second order polynomial, too.

Micro- and macro-turbulence velocities both show a similar dependence on surface gravity and effective temperature, which implies that there is a direct connection between both. A comparison of the macro (ζ)- and micro (ξ)-turbulent velocities with the sum of both ($\sqrt{\zeta^2+\xi^2}$) and the total projected weighted velocity dispersion σ_{tot} (see Sec. 3) is also shown in Figs. 6.12 and 6.13. The total projected weighted velocity dispersion (see Sec.3) is very similar to the macro-turbulent velocities and in most cases smaller than the sum of micro- and macro-turbulent velocity. It is possible, with this simple description of the total projected weighted velocity, to describe the broadening influence of the hydrodynamical velocity fields on spectral lines in comparison with the classical micro- and macro-turbulent description.

In order to obtain a good estimate of the line profile in 1D spectral line synthesis, knowledge of the micro- and macro-turbulent velocities is very important. Otherwise one could underestimate the equivalent width or the line width and hence obtain a wrong line depth.

I compare the determined micro- and macro-turbulent velocities to observational results from (Bean et al., 2006a,b) and (Bean, 2007). The determined values of the macro-turbulent velocities are roughly of the same order. The higher macro-turbulent velocities from Bean et al. possibly contain rotational broadening, but the Bean et al. micro-turbulent velocities are roughly a factor of two or three higher than the determined ones. These velocities were obtained from observed spectra by the authors of the afore mentioned papers using spectral fitting procedures. They used `PHOENIX` atmosphere models and the stellar analysis code `MOOG` (Sneden, 1973). One has to keep in mind that the empirical determination of micro-turbulence may also suffer from systematic errors. For most of the lines that Bean and collaborators employ (line data from Barklem et al. (2000)), the van de Waals damping constant is available. However, if not, then Unsöld's hydrogenic approximation is applied to calculate the value, and different authors use significantly different enhancement factors, changing its value. This illustrates the level of uncertainty inherent to this approach. For instance, Schweitzer et al. (1996) used an enhance factor of 5.3 (for the resulting γ_6 values) for their Fe I lines, while Bean et al. prefer 2.5 for Ti I lines (Bean, 2007). To investigate the detailed influence of van de Waals broadening on determination of micro-turbulence velocities is very interesting, but is beyond the scope of this paper. Uncertainties in the damping constant may introduce significant systematic biases in the resulting value of spectroscopically micro- and macro-turbulence which could easily be overestimated.

As mentioned above and illustrated in Fig. 6.12, the prediction of the micro-turbulence grossly underestimates the micro-turbulence values measured by Bean et al.. This might hint at deficits in the hydrodynamical modeling and one cannot exclude the possibility that a process is missing in the 3D models leading to a substantially higher micro-turbulence. But due to the argumentation above and a comparison with the solar micro- and macro-turbulence, one can argue that the Bean et al. values for the micro-turbulence are too high. However, before being able to draw definite conclusions, the observational basis has to be enlarged.

Chapter 7

T_{eff}- and $\log g$-Dependence of FeH Molecular Lines

In this chapter I study the dependence of FeH molecular lines on T_{eff} and $\log g$ in the 3D- and $\langle$3D$\rangle$-models. Again, the intention is to identify multi-D effects which might hamper the use of the FeH line diagnostics in standard 1D analyses. For this purpose, I compute the $\langle$3D$\rangle$-lines with no micro- and macro-turbulence velocity. With this method one can study the FeH lines without any velocity effects and can, through direct comparison between 3D- and $\langle$3D$\rangle$-lines, clearly identify velocity-induced effects. The results can also be found in Wende et al. (2009).

7.1 An Ensemble of 3D- and $\langle$3D$\rangle$-FeH Lines

I investigate ten FeH lines between 9950 Å and 9990 Å chosen from Reiners & Basri (2006) (see Table 7.1). We choose lines from different branches (Br), orbital angular momentum ω, and rotational quantum number J. The wavelengths in Table 7.1 are given in vacuum and E_l is the lower transition energy. While not directly relevant in the present context, because not the effects of magnetic fields are studied, it is noted that five lines are magnetically sensitive and five insensitive. The line synthesis were performed for fixed abundances with the `CO`^{5}`BOLD` atmosphere models listed in Table 6.1. The spectral resolution is $R \approx 2 \cdot 10^6$ ($\equiv 5 \cdot 10^{-3}$ Å) corresponding to a Doppler velocity of $v \approx 150\,\mathrm{m\,s^{-1}}$ at the wavelength of the considered lines ($\sim$ 9950). Figures 7.1 and 7.2 illustrate the strong influence of surface gravity and effective temperature on the line shape for the 3D-models. In Fig. 7.1, one can see that for both $\langle$3D$\rangle$- and 3D-lines, the line depth, line width and equivalent width W_λ decrease strongly with increasing effective temperature. The decrease of W_λ is due to stronger dissociation of the FeH molecules at higher temperatures, i.e the number of FeH molecule absorbers decreases. Differences in the line shape between 3D- and $\langle$3D$\rangle$-lines with changing temperature are barely visible. At higher T_{eff} values, the influence of broadening on the 3D lines due to velocity fields is slightly visible and not covered by thermal and van de Waals broadening any longer. At cooler temperatures, the velocity fields decrease and the differences between the $\langle$3D$\rangle$- and 3D-line shapes vanish. The van de Waals broadening is larger then the thermal broadening or that from the small velocity fields in the RHD models. In the model with $T_{\text{eff}} = 2800\,\mathrm{K}$, the lines start to become saturated. The FeH lines in the z-band at effective temperatures below $\sim$ 2600 K become too saturated and too broad for investigations of quantities like magnetic field strength or rotational broadening below $10\,\mathrm{km\,s^{-1}}$.

The differences between 3D- and ⟨3D⟩-line shapes of the $\log g$-series in Fig. 7.2 is more obvious than in the $T_{\rm eff}$ case. The differences in line depth and line width become significant with decreasing $\log g$. The lines in the 3D-models are significantly broadened due to the velocity fields in the RHD models, hence the line width is larger and the line depth lower. As it was seen in Sect.6.2, these velocity fields increase with decreasing $\log g$ and could be described in the 1D case in terms of macro- and micro-turbulent velocities.

The ⟨3D⟩-lines become slightly shallower and narrower towards smaller $\log g$. The equivalent width of the lines decreases with decreasing $\log g$ due to decreasing pressure and hence decreasing concentration of of FeH molecules. Also the van de Waals broadening loses its influence at lower pressures and the line width decreases. In all models the same chemical compositions is used, hence the concentration of Fe and H stays the same. The creation of FeH also depends on the number of H_2-molecules, which becomes larger towards lower temperatures and will be important in cool models.

The slightly different effective temperatures in the models with different $\log g$ (see Table 6.1) affect the line depths as well. If the effective temperatures were the same in the $\log g$-models, one would expect a monotonic behavior with decreasing line strength for decreasing surface gravity in the ⟨3D⟩-lines. However, because the model with $\log g = 3.0$ is cooler, the line depth is deeper than that of the one with $\log g = 3.5$. In the following analysis, I will correct the FWHM, W_λ, and the line depth of the lines in models with different $\log g$ for their slightly different effective temperatures.

The ten FeH lines all behave in the same way as the presented ones. I do not see any effect of different excitation potentials or $\log gf$ values on the line shapes that cannot be explained by their different height of formation. Thus, one can expect that an extraordinary interaction between these quantities and effective temperature or surface gravity can be excluded. I will quantify this preliminary result in the next section.

Table 7.1: Several quantities of the investigated FeH lines (Reiners & Basri, 2006).

λ_{rest} [Å]	$\log gf$	E_l [eV]	*Br.*	J	Ω	*magn. sen.*
9953.08	-0.809	0.156	R	10.5	1.5	weak
9954.00	-2.046	0.199	P	16.5	2.5-3.5	strong
9956.72	-0.484	0.375	R	22.5	3.5	strong
9957.32	-0.731	0.194	R	12.5	1.5	weak
9973.80	-0.730	0.196	R	12.5	1.5	weak
9974.46	-1.164	0.108	R	4.5	0.5	weak
9978.22	-1.190	0.030	Q	2.5	2.5	strong
9979.14	-1.411	0.093	R	2.5	0.5	strong
9981.46	-1.006	0.130	R	6.5	0.5	weak
9982.60	-1.322	0.035	Q	3.5	2.5	strong

7.2 FeH Line Shapes

To quantify the visual results of Fig. 7.1 and Fig. 7.2, I measured W_λ, the FWHM, and the line depth of the ten investigated FeHlines (see Table 7.1). The 3D- and ⟨3D⟩-lines are compared with each other to study the effects of the velocity fields in the 3D models and to explore the behavior

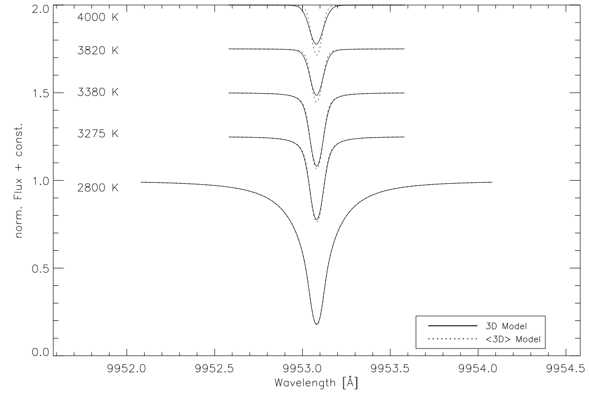

Figure 7.1: FeH lines with constant $\log g$ and varying $T_{\rm eff}$. Pairs of 3D- and ⟨3D⟩-lines are shifted by a constant for better visibility. The models are located at $T_{\rm eff}$ values of 2800 K, 3275 K, 3380 K, 3820 K and 4000 K and a $\log g$ value of 5.0, except the one with $T_{\rm eff} = 3820\,{\rm K}$ ($\log g = 4.9$), and the one with $T_{\rm eff} = 4000\,{\rm K}$ ($\log g = 4.5$) [cgs].

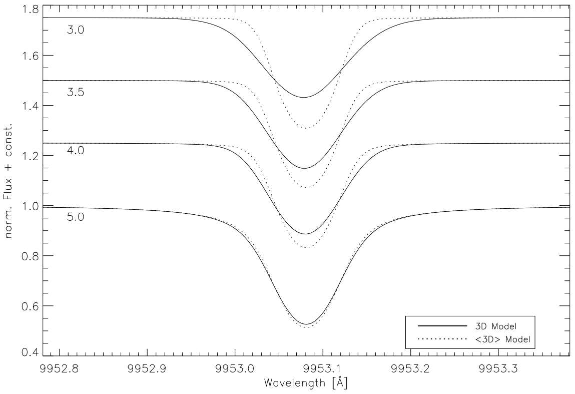

Figure 7.2: FeH lines wit constant $T_{\rm eff}$ and varying $\log g$. Pairs of 3D- and ⟨3D⟩-lines are shifted by a constant for better visibility. The models are located at a $T_{\rm eff}$ around $3300K$ and different $\log g$ values of 3.0 ($T_{\rm eff} = 3240\,{\rm K}$), 3.5 ($T_{\rm eff} = 3270\,{\rm K}$), 4.0 ($T_{\rm eff} = 3315\,{\rm K}$) and 5.0 ($T_{\rm eff} = 3275\,{\rm K}$) [cgs]. The large differences between 3D- and ⟨3D⟩-lines stem from the hydrodynamical velocity fields in the 3D models.

of the FeH without broadening effects from the hydrodynamical motion. These quantities are plotted in Fig. 7.3 and Fig. 7.4.

As mentioned above, one has to correct the line quantities in models with changing $\log g$ for their slightly different $T_{\rm eff}$. In Figs. 7.1 and 7.3 one can see how the investigated quantities depend on $T_{\rm eff}$. I determined spline fits $\wp$ for the three quantities of each line. For these fitting functions $\wp$ all five different effective temperatures were taken into account. In order to correct the line quantities to a reference temperature of ${T_{\rm eff}}^{\rm Ref.} = 3275\,{\rm K}$, a correction factor $\gamma = \frac{\wp_{\rm quant.}({T_{\rm eff}}^{\rm Ref.})}{\wp_{\rm quant.}(T_{\rm eff}.)}$ was used and was multiplied with the quantity for the $\log g$-model. This gives the value of the quantity for a $\log g$-model which would have $T_{\rm eff} = 3275\,{\rm K}$.

7.2.1 Equivalent Width W_λ

In the $T_{\rm eff}$-series, W_λ (see Fig. 7.3 upper panel) decreases with increasing $T_{\rm eff}$. At higher $T_{\rm eff}$ the number of FeH molecules decreases due to dissociation and hence W_λ. This can be seen in the 3D lines as well as in the ⟨3D⟩-lines. At $T_{\rm eff} = 2800\,{\rm K}$, the influence of van de Waals broadening in the 3D- and ⟨3D⟩-lines becomes clearly visible in the line profile due to saturation of the FeH lines. The ten different FeH lines all behave in a similar manner. The only difference is the absolute value of W_λ, which depends on the $\log gf$-value and the excitation potential E_l of each line.

In the $\log g$-series, the W_λ (see Fig. 7.4 upper panel) increases with increasing $\log g$. The change in concentration of FeH with lower $\log g$, which results in smaller W_λ, depends on the changing pressure and density stratification. The difference between 3D- and ⟨3D⟩-lines at small

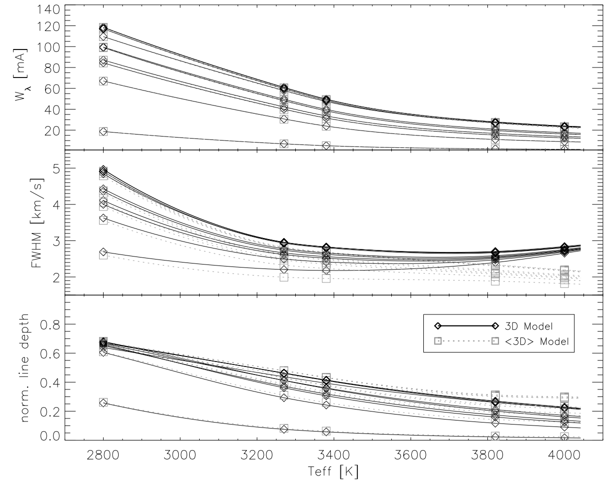

Figure 7.3: W_λ (top), FWHM (middle) and the line depth (bottom) of ten FeHlines (see Table 7.1) on models with different $T_{\rm eff}$. Squares are the data points for the ⟨3D⟩-models and diamonds for the 3D-models. W_λ and FWHM are on a logarithmic ordinate for better visibility. The data points of each line were connected with fitting functions (see text) to guide the eye. Plotted are the quantities of the 3D-models (black solid lines) and the ⟨3D⟩-models (gray dotted lines). The models are located at $T_{\rm eff}$ values of 2800 K, 3275 K, 3380 K, 3820 K and 4000 K and a $\log g$ value of 5.0, except the one with $T_{\rm eff}$ = 3820 K ($\log g$ = 4.9), and the one with $T_{\rm eff}$ = 4000 K ($\log g$ = 4.5) [cgs].

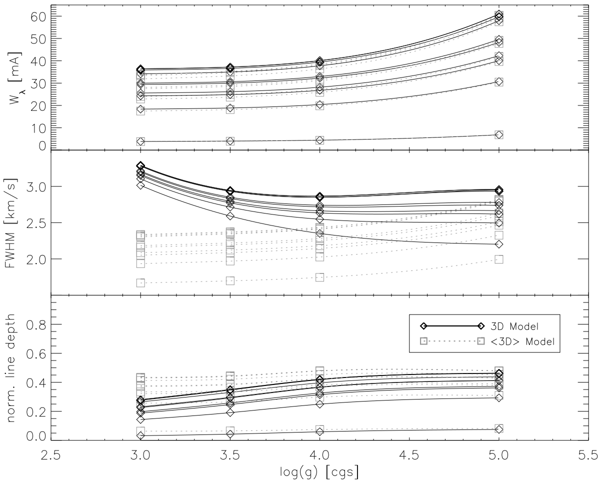

Figure 7.4: W_λ (top), FWHM (middle) and line depth (bottom) of ten FeH-lines (see Table 7.1) on models with different $\log g$. Squares are the data points for the ⟨3D⟩-models and diamonds for the 3D-models. The data points of each line were connected with fitting functions (see text) to guide the eye. The quantities of the 3D-models (black solid lines) and the ⟨3D⟩-models (gray dotted lines) are shown. All quantities are corrected to a $T_{\rm eff}$ of 3275 K.

$\log g$-values stems from the broadening by micro-turbulent velocities and vanishes at higher $\log g$ values. This time the FeH lines are only mildly saturated, but the velocity fields in the RHD models (see Sec.3) are strong enough to affect the W_λ as well. As in the $T_{\rm eff}$-series, the ten different lines show no significant variations in their behavior. They only vary in the amount of W_λ due to different $\log gf$-values.

Abundance Correction

Since the differences in W_λ are very small, one can expect that the 3D correction to the FeH abundance is very small too. I derive abundance corrections from a comparison between 3D and ⟨3D⟩ curve of growths for each set of lines on the different model atmospheres. The results are plotted in Fig. 7.5. In this case the correction to the different $T_{\rm eff}$ of the $\log g$ models is not applied. The 3D-⟨3D⟩ abundance correction is between -0.001 dex for the coolest high $\log g$ model and

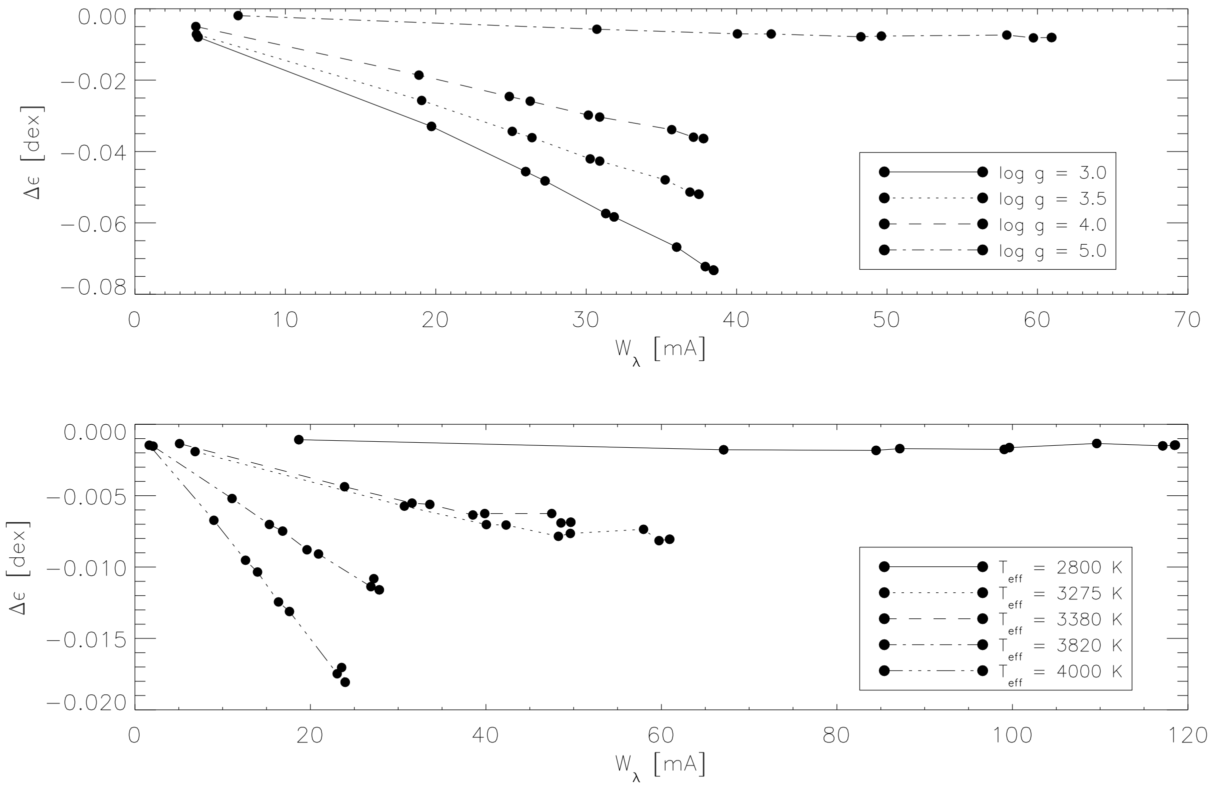

Figure 7.5: 3D – ⟨3D⟩ corrections to FeH abundances derived from different FeH lines with varying quantities, see Table 7.1. Upper panel: The models are located at a T_{eff} around $3300K$ and different $\log g$ values of 3.0 ($T_{\text{eff}} = 3240\,\text{K}$), 3.5 ($T_{\text{eff}} = 3270\,\text{K}$), 4.0 ($T_{\text{eff}} = 3315\,\text{K}$) and 5.0 ($T_{\text{eff}} = 3275\,\text{K}$) [cgs]. Lower panel: The models are located at T_{eff} values of 2800 K, 3275 K, 3380 K, 3820 K and 4000 K and a $\log g$ value of 5.0, except the one with $T_{\text{eff}} = 3820\,\text{K}$ ($\log g = 4.9$), and the one with $T_{\text{eff}} = 4000\,\text{K}$ ($\log g = 4.5$) [cgs].

-0.07 dex for the $\log g = 3.0$ model. In all cases the abundance correction is negative which mean that the 3D lines appear stronger due to the enhanced opacity which becomes larger due to the micro-turbulent velocity.

7.2.2 FWHM

The dependence of the line width (measured as the width of the line at their half maximum (FWHM)) on T_{eff} is shown in the middle panel of Fig. 7.3. At low T_{eff}, one can see that the FWHM of the 3D- and ⟨3D⟩- FeH lines decreases with increasing T_{eff}. The van de Waals broadening loses influence and also the dissociation of FeH molecules leads to smaller and narrower lines. After T_{eff} around 3380 K, the FWHM of the 3D lines reaches a flat minimum and starts to become larger again at higher T_{eff}. This rise in the line width is probably related to the rising velocity fields in the RHD models, since thermal broadening takes place in both 3D- and ⟨3D⟩-lines and the latter still decrease. The rise of the velocity in the models with a T_{eff} of 3380 K and 4000 K could also be due to the slightly lower surface gravity in these models, but I think that the main influence stems from the higher temperatures. The ⟨3D⟩-lines decrease monotonically with increasing $T_{\rm eff}$ and reflects, the behavior of W_λ. The difference in FWHM between 3D- and ⟨3D⟩-lines is very small at $T_{\rm eff} = 2800\,{\rm K}$ and increases with increasing $T_{\rm eff}$ to $\sim\ 0.8\,{\rm km\,s^{-1}}$ at the highest $T_{\rm eff}$. It was seen in Sect. 6.2.2 that this can be explained with the micro- and macro-turbulence description. The offset between the FWHM of the ten lines is due to their different $\log gf$-values i.e. large $\log gf$-values results in large FWHM. But since one is interested in broadening by the velocity fields, one has to take into account that lines with small $\log gf$-values, i.e. weak lines, formed deeper in the atmosphere where the convective motions are stronger. These lines are more broadened by the hydrodynamical velocity fields and hence more widened. One can see in Fig. 7.3 that the difference in FWHM between the ten 3D lines becomes smaller to high $T_{\rm eff}$. This is also valid for the lines in the $\log g$-series where the difference in FWHM between the ten 3D lines becomes smaller at small $\log g$-values.

In the $\log g$-series, the dependence of FWHM (Fig. 7.4 middle panel) is very different for 3D- and ⟨3D⟩-lines. In the 3D case, the FWHM stays almost constant with decreasing surface gravity between $\log g$ of 5.0 and 4.0 for most lines. This is due to the smaller amount of van de Waals broadening, which loses its influence due to lower pressure in models with smaller surface gravity. This is compared with the broadening due to the rising velocity fields. With $\log g$ smaller than 4.0, the width starts to increase for all lines. This increase of line width in the 3D case is a consequence of the hydrodynamic velocity fields which increase strongly with decreasing $\log g$. In the ⟨3D⟩ case, without the velocity fields, the FWHM decreases with decreasing surface gravity and reflects the behavior of the W_λ. The difference between 3D- and ⟨3D⟩-lines reaches its maximal value at $\log g = 3.0$ [cgs] and is around $1.3\,{\rm km\,s^{-1}}$. This is of the order of the velocity fields in the RHD models (see Fig. 6.8). One could fit 1D spectral synthesis FeH lines to observed ones (with known $T_{\rm eff}$) with the micro- and macro-turbulence description (see Sec. 3.2) and it will be possible with the obtained velocities to determine a surface gravity with the help of Fig. 6.13.

I did not see any significantly different behavior between the ten FeH lines in the $T_{\rm eff}$-series or in the $\log g$-series.

7.2.3 Line Depth

In the bottom panel of Fig. 7.3 one can see the dependence of the line depth on $T_{\rm eff}$. The line depth increases with decreasing $T_{\rm eff}$, and almost all FeH lines, except the one with the lowest $\log gf$ values, are saturated at $T_{\rm eff} = 2800\,{\rm K}$. The difference in line depth between 3D and ⟨3D⟩-lines change in the $T_{\rm eff}$-interval. At high $T_{\rm eff}$, the line depth of the ⟨3D⟩-lines is deeper than that of the 3D lines. At $T_{\rm eff} = 2800\,{\rm K}$, this difference almost vanishes. This behavior is due to the saturation of the FeH lines at low $T_{\rm eff}$ because both the 3D- and ⟨3D⟩-lines reach their maximal depth. The decrease of the line depth with increasing $T_{\rm eff}$ is due to the dissociation of the FeH molecules at higher temperatures.

The line depth of the $\log g$-series is shown in the bottom panel of Fig. 7.4. At low $\log g$, the line depths of the 3D and ⟨3D⟩-lines increase almost linearly with increasing $\log g$. The 3D lines increase with a strong slope and the ⟨3D⟩-lines with a weaker slope. The difference in line depth between 3D- and ⟨3D⟩-models is maximal at $\log g = 3.0$ [cgs] and vanishes almost at $\log g = 5.0$ [cgs]. It is consistent with the velocity fields present in the atmospheres of the RHD models broadening the lines and lower the line strength of the 3D lines. The ⟨3D⟩-lines reflect the decreasing number of FeH molecules with decreasing $\log g$ due to the lower pressures.

With these results, which imply that FeH lines are a valuable tool to measure stellar parameters, I will investigate a larger sample of lines in the next chapter.

Chapter 8

Line by Line Identification of FeH in the z-band

Since FeH provides a very large number of usable lines in the near infrared, where M type stars reach their maximum in emitted flux, it will be very helpful to provide an atlas of identified lines in this region. In order to do this, I will use high resolution spectra with good signal to noise from CRIRES[1] observations of an M 5.5 dwarf. The methods and results which will be described in the following are also published in Wende et al. (2010). The final atlas and line list can be found in the online material of the afore mentioned publication or here [2], and are described in more detail in the appendix.

8.1 Data

8.1.1 CRIRES Spectra of GJ1002

The observational data are CRIRES spectra of the inactive M 5.5 dwarf GJ1002 (see Fig. 8.1). The M dwarf has an assumed effective temperature of 3150 K (from the spectral type), and it is a very slow rotator ($v \sin i < 3$ km s^{-1}, Reiners & Basri, 2007). There is also very low H_α and X-ray activity from which one can assume that the magnetic field strength is relatively low. Owing to the weak magnetic field and slow rotation, GJ1002 is an ideal target for identification of molecular FeH lines. The lines are only slightly broadened by the different possible mechanisms in contrast to observations in sun spots where FeH lines are always influenced by a strong magnetic field.

CRIRES observations of GJ1002 were conducted in service mode during several nights in July 2007. The entrance slit width was set to $0.2''$, hence, the nominal resolving power was $R \sim 100\,000$. Four frames with an integration time of five minutes were taken in an ABBA-nod pattern for each of the nine wavelength settings covering the region between 986 – 1077 nm, leaving only one larger gap at 991.15 – 992.45 nm and two smaller gaps at 997.15 – 997.50 nm and 1057.15 – 1057.65 nm.

Data reduction made use of the ESOREX pipeline for CRIRES. Science frames and flatfield frames were corrected for non-linearity and 1D spectra were extracted from the individual flatfielded and sky subtracted frames with an optimum extraction algorithm. The wavelength solution is based at first order on the Th-Ar calibration frames provided by ESO. Due to the slit

---

[1] Data were taken at ESO Telescopes under the program 79.D-0357(A)

[2] `http://www.astro.physik.uni-goettingen.de/~sewende/`

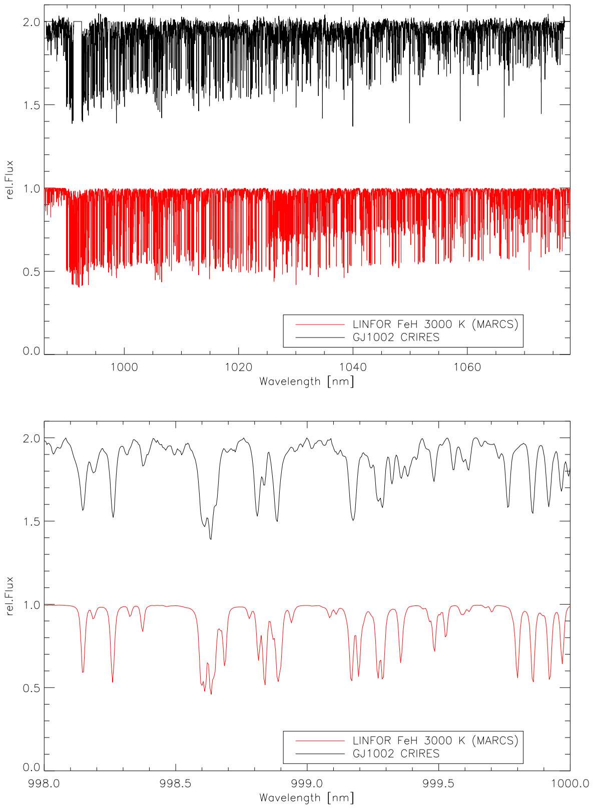

Figure 8.1: Top: FeH Wing-Ford band, observed (black) and computed (red). Bottom: a magnification of the spectrum above.

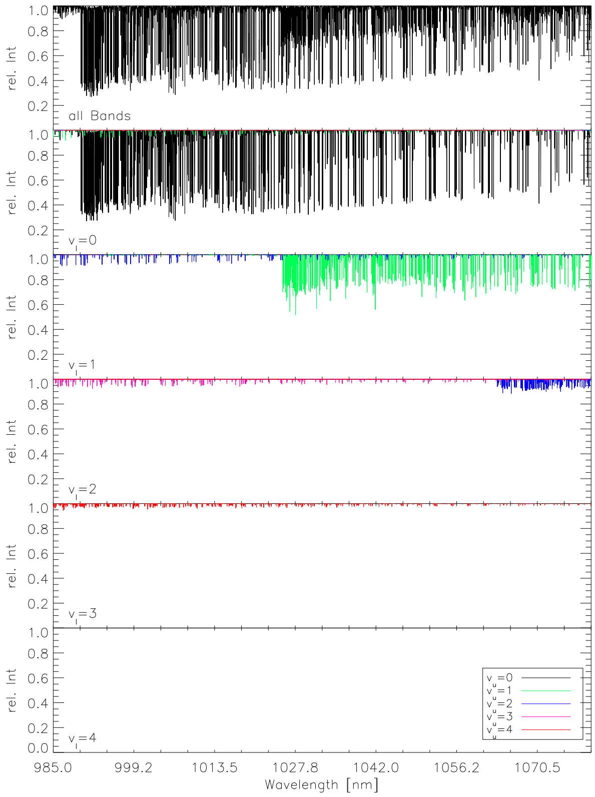

Figure 8.2: FeH vibrational bands separated by their vibrational quantum numbers. See color version for more details.

curvature, spectra taken in B-nodding positions are shifted in wavelength with respect to spectra taken in A-nodding positions. This was corrected for by mapping all 1D spectra to the spectrum of the first A-nod position.

The individual CRIRES wavelength settings provide a considerable degree of spectral overlap and up to eight individual spectra were combined into one final spectrum at each wavelength. While merging the individual settings, small mismatches in the wavelength solutions as well as imperfections in the individual spectra (detector cosmetics, ghost contamination) were corrected. The final spectrum was normalized to a pseudo-continuum level of unity and finally shifted to match the McMath FTS spectrum of solar umbra (Wallace et al., 1998). The error in the wavelength calibration should be smaller than 0.75 km s^{-1}.

The SNR at the continuum level of most parts of the final spectrum is found to exceed 200. The high signal-to-noise ratio and high spectral resolution of the CRIRES data allows one to identify FeH lines with high accuracy.

8.1.2 Theoretical FeH Molecular Data and Line Synthesis

The theoretical data which was used to identify the FeH lines is taken from Dulick et al. (2003). They provide tables of quantum numbers and energies[3]. In particular, they provide the vibrational assignment of the upper and lower states v_u and v_l, respectively, the projection of the total orbital angular momentum on to the internuclear axis for the upper and lower state, Ω_u and Ω_l, and the rotational quantum numberJ_l for the lower state. Furthermore the transition branch (P, Q, R), the parity, the wavenumber in cm^{-1}, the lower state energy of the transition E_l and the Einstein A value are given.

From this information it is possible to estimate $\log_{10} gf$-values through (Bernath, 2005)

$$g_l f = \frac{\epsilon_0 m_e c^3}{2\pi e^2 \nu^2} A g_u, \tag{8.1}$$

with $g_l = 2J_l + 1$ and $g_u = 2J_u + 1$ as the lower and upper statistical weights of the transition and $\nu = c/\lambda$ as the transition frequency. All quantities are in SI units.

The van der Waals broadening is determined following Schweitzer et al. (1996), which is basically Unsöld's hydrogenic approximation. For the ionization energy needed in this approximation I used an empirically determined value of 6 eV, which was deduced from comparison with other diatomic molecules (Wende et al., 2009, or see chapter 5). Although this is not the theoretical value, which is slightly higher, I used this one because its influence on the van der Waals broadening is not significant.

The molecular partition function for FeH, Q_{FeH}, which is needed for the concentration of FeH, is computed after Sauval & Tatum (1984) with molecular data taken from Tables 9 and 10 of Dulick et al. (2003). Equation 8.2 is given in a polynomial expression of a fit to the partition function which is valid between 1000 K and 8000 K.

$$Q_{FeH} = \sum_{i=0}^{4} a_i T^i, \tag{8.2}$$

where T is the temperature in K and

$$\begin{pmatrix} a_0 \\ a_1 \\ a_2 \\ a_3 \\ a_4 \end{pmatrix} = \begin{pmatrix} -4.9795007e+02 \\ 6.5460944e-01 \\ 3.4171590e-04 \\ 2.7602574e-07 \\ 1.0462656e-11 \end{pmatrix}, \tag{8.3}$$

are the coefficients of the polynomial. For the creation of FeH, i.e. the concentration that is governed by the Saha-Boltzmann Eq., I assume Fe + H → FeH. With this partition function and the data from Dulick et al. (2003) we can use a simple description for the absorbance (described in Sect. 8.2.4 in this paper in more detail) to compute FeH spectra with a simple reversing layer model and separate the lines into vibrational bands in the observed wavelength region (see Fig. 8.2). From this figure one can expect that there will be two sequences of vibrational transitions, namely the sequence with $\Delta v = 0$, which are the $(0,0)$, $(1,1)$, and $(2,2)$ vibrational transitions, and the sequence with $\Delta v = 1$, which are the $(1,0)$, $(2,1)$, $(3,2)$, and $(4,3)$ transitions. I note that this method does not take into account (among many other things) the atmospheric structure or the chemical composition of the star. It gives only a rough estimate of the relative strengths of the FeH bands.

---

[3] See `http://bernath.uwaterloo.ca/FeH`

The full synthetic line formation for the comparison and identification of the observed FeH lines is done with the line formation code `SYNTH3` (Kochukhov, 2007). This code is able to compute large spectral regions with all FeH lines taken from our line list (see Fig. 8.1). I used only lines with $\log_{10} gf > -7$ because I assume that other lines have no significant influence. By computing all the lines in a certain region at once, it is accounted for blends, but also all lines of the region were computed individually to measure their equivalent width W_λ with the `LINFOR3D` code (based on Baschek et al., 1966). For the input model atmospheres I used `MARCS` (Gustafsson et al., 2008) with solar composition (Grevesse et al., 2007). These models are well suited for these cool temperatures in low-mass stars, because they make use of up-to-date atomic and molecular data and reach to effective temperatures of 2500 K. I used the plane-parallel LTE models where the convection is treated in the mixing-length approximation. In the computation of these model atmospheres, the microturbulence parameter was set to zero. However, in the computations of the actual spectra, I assumed microturbulence parameters according to the results of Wende et al. (2009). I do not expect any significant influence because they are on the order of a few hundred m s^{-1}. I neglect the broadening from macro-turbulent motion, which would be hardly visible in the observed spectra.

8.2 Methods

I began with the investigation of the observed spectrum, for which I determined the position of the spectral lines and decide whether a line feature is a blend or not. Then I measured the equivalent width W_λ of the lines with a Voigt-fit procedure described below.

I compared the line positions found in the CRIRES data to theoretical ones and identified them with FeH lines. In order to confirm an identification, I used statistical means: (i) the method of coincidence, and a cross-correlation technique producing coincidence curves; and (ii) a method which takes the intensity into account. In this latter method I will compare the theoretical line strength S (Hönl-London factor) with the observed W_λ following Schadee (1964). I also use a description for the absorbance of spectral lines to correct theoretical line intensities given in terms of the Einstein A values. For this I will compare the observed and computed spectra with each other and obtain a scaling factor for the Einstein A values. The final result is a corrected line list that reproduces the observed stellar spectrum as well as the line positions in sunspot spectra from Wallace et al. (1999). The line intensities are hard to confirm in the solar case, because many FeH lines are strongly split by magnetic fields.

8.2.1 Voigt Fit

In order to measure W_λ in the observed spectra I used a 'multi-Voigt fit' procedure (based on IDL curvefit function). This is defined as

$$F = \sum\nolimits_{i=0}^{N} A_i \cdot \frac{H(u_i, a_i)}{max(H(u_i, a_i))}, \tag{8.4}$$

where A is the amplitude describing the depth of the line,

$$u = \frac{\lambda - \lambda_0}{\sigma}, \tag{8.5}$$

with σ as Gaussian (or Doppler) width,

$$a = \frac{\gamma}{4\pi} \frac{{\lambda_0}^2}{c} \frac{1}{\sigma}, \tag{8.6}$$

which will be called the Voigt constant throughout in this paper, γ is the radiation damping constant, and $H(u, a)$ is the Hjerting function (Gray, 2008, and references therein). I successively fitted the whole spectrum within bins of 7 Å . The first and the last 1 Å were cut off after the fit to avoid boundary effects, and I used only line profiles whose centers are inside the 5 Å bin. For the Voigt profiles inside a bin, I assumed a constant a-value for the Lorentz part and a fixed Gaussian width, but changes in these two parameters from one wavelength bin to another are allowed because the FeH lines tend to become narrower towards longer wavelengths. This is probably because a and σ were used only as fit parameters, and the FeH lines start to saturate at the band head, but become weaker towards longer wavelengths. Hence, the width of the line profile, which is a combination of a and σ, decreases with decreasing saturation and consequently both parameters decrease. The wavelength dependence of the Doppler width affects the width of the lines as well, but it is negligible and goes in opposite direction (for example, $\sigma = 0.1$ Å at $\lambda = 10\,000$ Å would change to $\sigma = 0.105$ Å at $\lambda = 10\,500$ Å).

With this fit procedure, I obtained the parameters (position, depth (amplitude), Voigt constant, and σ), needed for the individual Voigt line-profiles to fit the observed spectrum. In Fig. 8.3 I show an example of how the fit (red) reduced the observed spectrum (black) into single-line profiles (bottom panel).

The convergence criterion is the minimization of the residual flux between observation and fit $(O - C)$. The iteration is stopped if the maximal error of the fit is lower than three times the standard deviation of the error or if the standard deviation of the error does not change significantly between two iterations. From these Voigt profiles, W_λ can easily be computed by integrating over the single-line profiles. The fit is also able to find and separate possible blends. For this, I assume that the blended components differ in position by at least 0.1 Å .

The measured W_λ will be assigned to the associated theoretical lines. This means that if an observed line can be identified with exactly one theoretical line, W_λ is fully assigned to this one theoretical line. However, in most cases the theory predicts more than one line for an observed line position because of numerous overlapping vibrational bands in the same wavelength region and from many closely-spaced line pairs, which only differ in parity. Then W_λ will be distributed to all predicted theoretical lines at this position. This is done with the ratio R_i of theoretical equivalent widths ${}^{theo}W^i_\lambda$, which is obtained from the individual theoretical line profiles:

$$R_i = \frac{{}^{theo}W^i_\lambda}{\sum_{i \in B} {}^{theo}W^i_\lambda}, \tag{8.7}$$

with B as the set of blended components. There is of course the chance that FeH is not the only contributor to the observed blend. To avoid this uncertainty, we additionally used the line intensities in a method described below.

8.2.2 Method of Coincidence

To confirm the identification of a molecular band, or a sub-band, the ‘method of coincidence’ were used, which was first introduced by Russell & Bowen (1929). It gives the number of lines C in a spectral range that will be found by chance if one uses a set of randomly generated line-positions

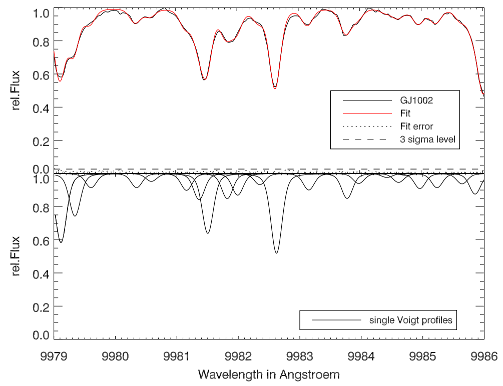

Figure 8.3: Upper panel: Part of the observed spectrum of GJ1002 with multiple Voigt fit. Lower panel: the single Voigt functions which were returned by the fit.

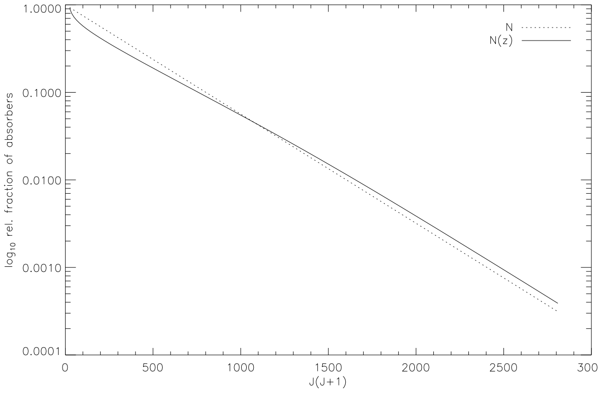

Figure 8.4: Relative number of absorbers with (dashed line), and without (solid line) constant number of FeH molecules over different atmospheric layers.

and compares them with observed ones. Fundamental probability calculations lead to

$$C = M[1 - \exp(-2xw)], \tag{8.8}$$

where M is the number of lines in a particular region, x is the tolerated deviation in position, and w is the line density (average number of spectral lines in the investigated region). This means that $C/M = p_{\text{random}}$ gives the probability of finding with a randomly chosen line position a random coincidence. If one identifies N out of M lines in the observations, then the probability of finding an identification is $N/M = p_{\text{identified}}$. The ratio N/C describes how likely it is to find a line by random coincidence per identified line. Hence, the number of actually identified lines N should exceed the number of C of purely random coincidences. If this is the case, then one can assume that the lines are probably identified in the observed spectra.

8.2.3 Theoretical Line Strength

For the identification of molecular lines it is also useful to take the intensities of the lines into account. To compare the theoretical line strength S with the observed equivalent width W_λ, we follow Schadee (1964). For weak lines (mildly saturated) W_λ is proportional to the wavelength λ_0, the oscillator strength f, and N_i, the number of absorbers (Gray, 2008):

$$W_\lambda \propto \lambda_0^2 f N_i, \tag{8.9}$$

and

$$f \propto \frac{g_u}{g_l} \lambda_0^2 A, \tag{8.10}$$

with N_i as the number of absorbers given by the Boltzmann distribution

$$N_i \propto g_l e^{\left(\frac{-hc}{kT} E_0\right)}, \tag{8.11}$$

where E_0 is the lower-state energy level in cm^{-1}. To derive the final form, I use Eqs. 8.10 and 8.11 together with Eq. 8.9 and the expression for the Einstein A value

$$A = \frac{A_{v_u,v_l} S}{g_u}. \tag{8.12}$$

Here A_{v_u,v_l} is the Einstein A for a specific vibrational transition and constant for the vibrational band. The resulting equation is

$$\log_{10} \frac{W_\lambda}{S\lambda_0^4} = C - \frac{hc}{kT} E_0 \log_{10} e, \tag{8.13}$$

which is the relation from Schadee (1964) with E_0 replacing $BJ_l(J_l+1)$. Possible stimulated emission can be neglected for this analysis because there is only a small population in the excited state. If one plots $\log_{10} W_\lambda/S\lambda_0^4$ against E_o, a straight line should be found, which then suggests the correct identification of the lines in the FeH molecular band. Equation 8.13 accounts for different branches as well as for different Ω. This is because S on the left side of Eq. 8.13 is computed for all branches (P, Q, R) and Ω values.

The S values that I will use in the analysis are computed for the intermediate Hund's case and are determined from the Einstein A values given by Dulick et al. (2003).

I point out that it is implicitly assumed in Eq. 8.11 that the total number of FeH molecules N is constant for all lines. This assumption is only valid if one considers a small isothermal atmospheric layer. However, because a spectral line forms over several layers, this assumption is not exactly valid. If one furthermore considers a set of lines with a wide range in gf and E_0 values, one expects that these lines form at different heights. Thus, the number of FeH molecules is not constant anymore: strong spectral lines are assumed to be formed in higher atmospheric layers, and weak lines in deeper layers. Hence, deviations from a straight line in the $[\log_{10} W_\lambda/S, E_0]$ diagram for lines with very low and very high J are expected. If one assumes more FeH molecules in deeper layers, larger equivalent widths for these lines can be expected owing to higher density. For a qualitative description, I assume the total number of FeH molecules to be inversely proportional to the equivalent width, which reflects the heights of formation for weak and strong lines.

$$N(z) = N \cdot \alpha W_\lambda^\beta. \tag{8.14}$$

α and β are free parameters and here chosen as 1.25 and -0.25, respectively. I plot the right hand side of Eq. 8.13 for the constant and variable molecule number in Fig. 8.4. Still, the situation is much more complicated, and I use synthetic line formation to investigate this behavior in the results section.

Following Schadee (1964), one can now use the $[\log_{10} W_\lambda/S, E_0]$ diagram to classify the identified FeH lines into one of the following classes:

1. P - the line is present, and its W_λ agrees well with the straight line of the diagram.
2. Pb - the line is present, but its W_λ is too large, i.e. the $\log_{10} W_\lambda/S$ value lies above the straight line of the diagram. This could imply that the line is blended by another element (or that its computed line strength is too weak).
3. R - the line strength is presumably reduced by perturbations. That means that the computed line strength is too great and the data point lies below the line.

4. Q - the line was identified, but its identification can not be verified, because only lines with $\Delta\Omega = 0$ were investigated in this plot.

Eventually, it should be possible to derive the excitation temperature for the rotational transitions T in Eq. 8.13 from the slope of a linear fit in the $[\log_{10} W_\lambda/S, E_0]$ diagram. Yet one has to be careful. Wöhl (1970) reports that the obtained rotational temperature from this method crucially relies on the data points which are included in the linear fit and also on the degree of accuracy in measuring W_λ. I also experienced the same difficulties.

8.2.4 Line Strength Correction

In some cases W_λ and line depths of the observed FeH lines do not match the computed ones from the line list. In general, I observe that the differences increase towards longer wavelengths and computed lines become stronger than observed ones. The strength of the lines are mainly determined by the lower state energies E_0 and the Einstein A values. I will correct only the Einstein A values, because a set of high-resolution spectra in the z-band for different temperatures would be required to correct E_0. To correct the Einstein A value, I use the formula from Bernath (2005) for the absorbance in a modified form where the Einstein A values enter the expression

$$-\ln\left(\frac{I}{I_0}\right)_x = \frac{(2J_u+1)A_x}{8\pi\bar{\nu}^2 q} e^{-E_0^x/kT}(1-e^{-h\nu/kT})GNl, \tag{8.15}$$

where $\bar{\nu}$ is the frequency of a molecular in cm $^{-1}$, N is the number of molecular absorbers per cubic cm in the energy state (population density), q is the partition function, l is the length, e.g. for an atmospheric layer, and G is a line profile function, e.g. a Voigt function. If I compare the observed spectra with the computed one (produced with the `SYNTH3` code) and assume that both atmospheres have the same structure, then A_x and E_0^x are the only variables that account for differences in the spectra (x stands for either the computed or observed spectra). I also assume E_0^x as constant and write

$$\frac{-\ln\left(\frac{I}{I_0}\right)_{obs}}{-\ln\left(\frac{I}{I_0}\right)_{comp}} = \frac{A_{obs}}{A_{comp}}. \tag{8.16}$$

This shows that the correction for the Einstein A value is merely a linear scaling with the ratio of the intensities

$$A_{obs} = \frac{-\ln\left(\frac{I}{I_0}\right)_{obs}}{-\ln\left(\frac{I}{I_0}\right)_{comp}} A_{comp} = sA_{comp}. \tag{8.17}$$

I introduced the scaling factor s for the ratio of both intensities. If I use that $A = A_{v_u,v_l}S/(2J_u+1)$ (Dulick et al., 2003), then

$$s = \frac{A^{obs}_{v_u,v_l}}{A^{comp}_{v_u,v_l}} \frac{S_{obs}}{S_{comp}}, \tag{8.18}$$

where S is the Hönl-London factor. If the theoretical S values are wrong, one could perhaps detect it using Eq. 8.13 or perhaps in a possible dependence of the scaling factors on J_l.

Table 8.1: Identified atomic lines

Ion	$Position[\ ]$	E_l	$\log gf$	Ion	$Position[\ ]$	E_l	$\log gf$	Ion	$Position[\ ]$	E_l	$\log gf$
'Cr1'	9903.6226	2.987	-2.131	'Fe1'	10116.787	2.759	-3.705	'Ti1'	10399.651	0.848	-1.623
'Ti1'	9930.0728	1.879	-1.580	'Ti1'	10123.668	2.175	-1.722	'Cr1'	10419.476	3.013	-1.806
'Ti1'	9944.1036	2.160	-1.821	'Ti1'	10148.300	3.148	-0.910	'Fe1'	10425.885	2.692	-3.627
'Ti1'	9951.7317	2.154	-1.778	'Fe1'	10148.342	4.796	-0.177	'Ti1'	10462.915	2.256	-2.054
'Cr1'	9951.7997	3.556	-1.129	'Fe1'	10157.947	2.176	-4.225	'Fe1'	10472.522	3.884	-1.187
'Ti1'	9967.4679	1.053	-4.108	'Fe1'	10170.256	2.198	-4.114	'Cr1'	10489.119	3.011	-0.972
'Ti1'	10000.700	1.873	-1.840	'Ti1'	10173.274	1.443	-3.465	'Ti1'	10498.990	0.836	-1.739
'Ti1'	10005.828	2.160	-1.124	'Fe1'	10197.900	2.728	-3.589	'Cr1'	10512.887	3.013	-1.558
'Ti1'	10008.403	1.067	-3.626	'Ca1'	10201.981	4.680	-0.369	'Fe1'	10535.121	3.929	-1.482
'Ti1'	10014.490	2.154	-1.284	'Ca1'	10205.743	4.681	-0.199	'Cr1'	10552.983	3.011	-1.976
'Sc1'	10027.787	1.865	-1.286	'Ca1'	10205.803	4.681	-1.102	'Ti1'	10554.648	1.887	-2.607
'Ti1'	10037.242	1.460	-2.227	'Ca1'	10211.457	4.681	-0.039	'Fe1'	10580.037	3.301	-3.137
'Ti1'	10051.581	1.443	-2.205	'Ca1'	10211.561	4.681	-1.102	'Ti1'	10587.533	0.826	-1.866
'Sc1'	10060.261	1.851	-1.479	'Fe1'	10221.204	3.071	-2.760	'Ti1'	10610.624	0.848	-2.761
'Fe1'	10060.397	5.033	-1.231	'Fe1'	10268.031	2.223	-4.533	'Fe1'	10619.630	3.267	-3.128
'Ti1'	10060.485	2.175	-0.894	'Ca1'	10291.397	4.624	-0.265	'Cr1'	10650.558	3.011	-1.613
'Ti1'	10062.662	1.430	-2.351	'Fe1'	10343.720	2.198	-3.574	'Ti1'	10664.544	0.818	-2.007
'Fe1'	10067.804	4.835	-0.288	'Ca1'	10346.655	2.933	-0.408	'Cr1'	10670.437	3.013	-1.489
'Ti1'	10069.273	2.160	-1.750	'Fe1'	10350.802	5.393	-0.548	'Cr1'	10675.063	3.013	-1.374
'Ti1'	10077.885	1.067	-4.065	'Fe1'	10381.844	2.223	-4.145	'Ti1'	10679.972	0.836	-2.592
'Cr1'	10083.115	3.556	-1.307	'Ti1'	10393.591	1.502	-2.595	'Fe1'	10728.124	3.640	-2.763
'Fe1'	10084.158	2.424	-4.544	'Cr1'	10394.793	3.010	-2.006	'Ti1'	10729.329	0.813	-2.156
'Cr1'	10114.770	3.013	-2.073	'Fe1'	10398.645	2.176	-3.390	'Ca1'	10729.654	4.430	-1.841

8.3 Results

8.3.1 Atomic Line Identification and Unidentified Lines

Because atomic lines are present in the wavelength region of the observed spectra of GJ1002, I use the VALD [4] (Kupka et al., 1999; Piskunov et al., 1995) database to include the available atomic line data in this calculations. I give a list of atomic lines present at $T_{\rm eff} = 3100\,{\rm K}$ in Table 8.1. I included lines deeper than 2% below the continuum in the computed spectra. I did not try to correct the atomic line positions or line strengths and took the data as provided by VALD.

After I identified the atomic lines and FeH lines, there were still unidentified lines that seemed to belong to neither FeH nor to a known atomic line. I give a list of these lines for which the line depth is deeper than 10% below the continuum (Table 8.2). Our opinion is that most of these lines belong to FeH, but I was unable to identify them with confidence.

---

[4] `http://vald.astro.univie.ac.at`

Table 8.2: List of unidentified lines deeper then 0.9.

λ_{vac} [Å]	Depth	λ_{vac} [Å]	Depth	λ_{vac} [Å]	Depth	λ_{vac} [Å]	Depth	λ_{vac} [Å]	Depth	λ_{vac} [Å]	Depth	λ_{vac} [Å]	Depth
9904.46	0.88	10084.8	0.90	10235.9	0.84	10344.9	0.86	10424.9	0.79	10547.5	0.80	10644.2	0.84
9909.42	0.87	10095.7	0.86	10238.5	0.73	10346.0	0.76	10427.8	0.89	10548.2	0.85	10645.7	0.84
9927.74	0.79	10098.8	0.89	10242.9	0.89	10347.3	0.82	10438.8	0.87	10548.7	0.89	10655.3	0.80
9930.70	0.81	10107.3	0.85	10246.4	0.81	10347.5	0.87	10440.0	0.85	10550.8	0.88	10660.2	0.79
9931.26	0.87	10107.6	0.86	10247.3	0.74	10347.7	0.87	10442.0	0.80	10555.8	0.90	10660.7	0.87
9932.82	0.88	10108.7	0.89	10247.3	0.74	10351.3	0.89	10443.2	0.84	10559.0	0.89	10665.1	0.84
9932.94	0.88	10116.9	0.65	10248.4	0.84	10354.4	0.79	10443.6	0.89	10563.5	0.82	10665.6	0.71
9938.22	0.88	10140.2	0.89	10255.4	0.84	10357.5	0.89	10444.6	0.90	10563.8	0.67	10666.9	0.87
9978.82	0.89	10141.5	0.73	10260.6	0.88	10358.5	0.74	10444.8	0.81	10565.8	0.82	10669.6	0.88
9983.94	0.90	10144.5	0.66	10261.0	0.88	10361.5	0.86	10444.9	0.90	10567.1	0.83	10671.3	0.90
9984.94	0.90	10164.4	0.89	10266.4	0.81	10363.3	0.89	10446.7	0.88	10568.8	0.90	10671.6	0.71
9985.22	0.90	10167.5	0.84	10267.3	0.79	10367.9	0.87	10449.3	0.88	10571.1	0.89	10673.3	0.88
9993.22	0.72	10171.2	0.89	10274.1	0.74	10369.1	0.88	10463.2	0.81	10577.5	0.90	10674.7	0.83
9993.82	0.77	10174.1	0.89	10280.7	0.87	10378.0	0.83	10463.9	0.84	10580.6	0.85	10675.5	0.81
9994.14	0.87	10177.2	0.90	10281.0	0.77	10381.0	0.88	10464.3	0.77	10582.8	0.80	10681.4	0.90
9997.30	0.88	10187.0	0.81	10286.1	0.89	10382.0	0.90	10464.9	0.90	10586.5	0.87	10697.2	0.89
9999.94	0.77	10188.6	0.67	10287.4	0.82	10382.7	0.78	10477.6	0.75	10586.9	0.75	10697.3	0.88
10005.3	0.89	10193.7	0.83	10297.2	0.80	10383.8	0.85	10479.6	0.86	10588.5	0.90	10711.9	0.81
10015.0	0.81	10197.2	0.87	10298.0	0.88	10383.9	0.85	10490.9	0.83	10589.6	0.89	10712.3	0.86
10021.2	0.88	10200.1	0.89	10303.5	0.88	10385.7	0.89	10493.9	0.87	10593.8	0.84	10713.0	0.74
10023.7	0.87	10202.9	0.90	10309.6	0.86	10387.8	0.86	10499.5	0.83	10594.3	0.76	10716.6	0.85
10027.7	0.89	10203.0	0.90	10310.6	0.84	10392.2	0.87	10499.6	0.83	10600.7	0.87	10724.6	0.77
10029.3	0.86	10209.1	0.86	10312.2	0.75	10396.0	0.73	10500.2	0.75	10601.8	0.89	10725.3	0.81
10031.8	0.70	10211.1	0.70	10312.5	0.89	10398.4	0.89	10500.9	0.87	10602.9	0.88	10726.4	0.86
10035.9	0.83	10214.5	0.79	10314.7	0.84	10399.2	0.87	10514.7	0.84	10604.0	0.89	10734.7	0.85
10041.9	0.90	10215.8	0.77	10319.3	0.90	10400.2	0.82	10515.1	0.88	10605.3	0.90	10739.2	0.90
10048.2	0.82	10217.8	0.89	10319.5	0.85	10400.5	0.88	10515.5	0.79	10605.5	0.88	10740.5	0.82
10051.1	0.86	10219.5	0.86	10320.6	0.86	10402.8	0.83	10516.6	0.89	10609.5	0.87	10744.1	0.86
10066.5	0.88	10219.9	0.87	10322.2	0.88	10406.5	0.89	10519.3	0.88	10609.6	0.88	10745.3	0.84
10068.7	0.79	10220.0	0.88	10322.8	0.75	10406.8	0.81	10519.7	0.89	10612.7	0.77	10748.7	0.90
10073.9	0.58	10223.9	0.85	10327.8	0.89	10408.4	0.87	10532.9	0.86	10613.1	0.82	10749.4	0.88
10074.5	0.89	10225.8	0.77	10327.9	0.87	10409.3	0.75	10535.5	0.89	10614.0	0.81	10752.1	0.90
10075.9	0.90	10226.7	0.76	10328.3	0.78	10410.1	0.81	10536.2	0.86	10626.7	0.82	10753.7	0.90
10078.5	0.86	10227.7	0.88	10332.7	0.88	10415.7	0.89	10539.5	0.83	10629.9	0.88	10754.7	0.79
10080.6	0.75	10229.4	0.89	10338.9	0.64	10417.8	0.88	10543.1	0.87	10634.8	0.89	10755.8	0.90
10083.8	0.72	10230.5	0.73	10340.0	0.89	10422.5	0.90	10546.1	0.86	10638.3	0.80	10759.4	0.89

8.3.2 FeH Line Identification

The results from the Voigt fit were used to assign the individual Voigt profiles from the observed lines to the individual theoretical FeH lines. I did this by hand, and defined a line as identified if the position of the observed line agreed within 0.1 Å to the theoretical predicted position. If the offset is larger than 0.1 Å , I identified a line feature if the characteristic shape was similar in the observations and computations (e.g. the line at 999.55 nm or 999.8 nm in Fig. 8.5). In Fig. 8.5, and also in the full FeH atlas, I labeled all identified lines with their quantum numbers, i.e. vibrational assignment (v_u, v_l), branch (P, Q, R), lower-state rotational quantum number J, Ω, and in the case of blends, with their contribution to the blend. I did this for the observed wavelength region, and the complete plot is available in the online material of Wende et al. (2010) or here [5]. In Fig. 8.6 a histogram of the residuals between the computed line positions and the observed ones is shown. There is no obvious systematic behavior of the scatter with wavelength (see inset in Fig. 8.6). The scatter follows a normal distribution centered at $\Delta\lambda = 0.02$ Å corresponding to 0.67 km s^{-1}. This mean value is beyond our spectral resolution, and in general all residuals smaller than 0.75 km s^{-1}($\sim$ 0.025 Å) are not significant because they are also smaller than the accuracy of the wavelength calibration. From the investigation of the line positions, it can be seen that the fraction of lines for which the residuals are smaller than a certain range are distributed as shown in the right inlay of Fig. 8.6. This plot shows that $\sim$ 80 % of the line features could be identified

---

[5] `http://www.astro.physik.uni-goettingen.de/~sewende/`

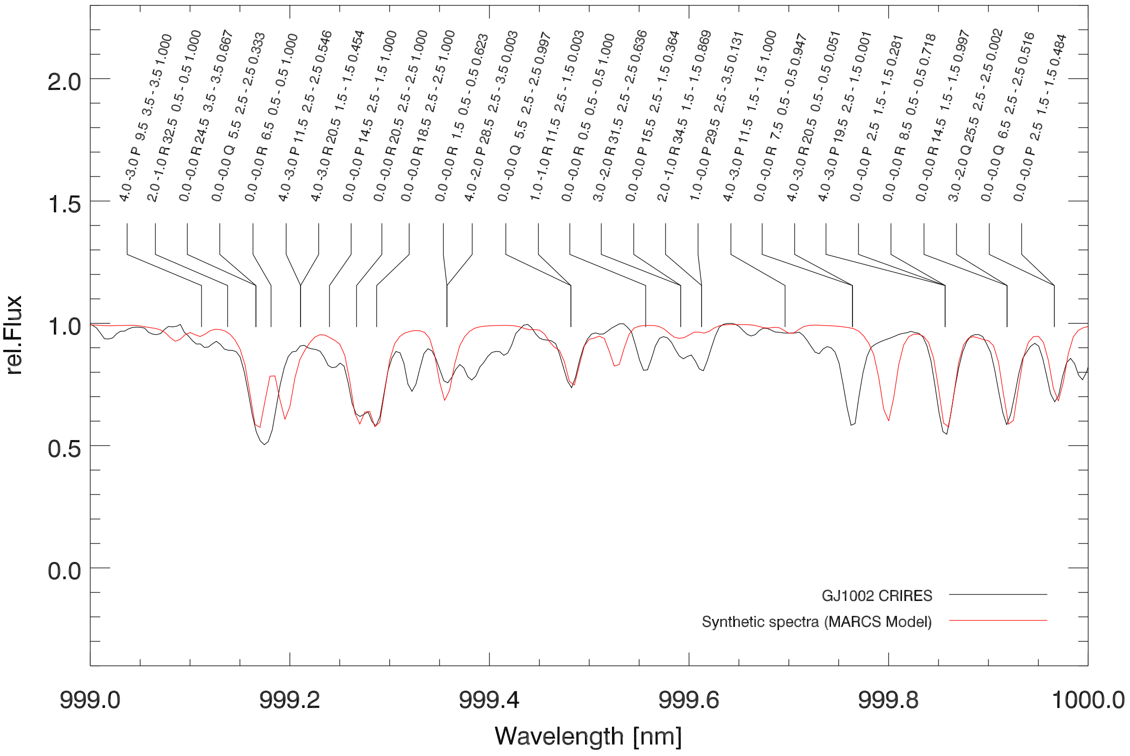

Figure 8.5: Observed spectrum of GJ1002 (black) and computed one (red) labeled with quantum numbers.

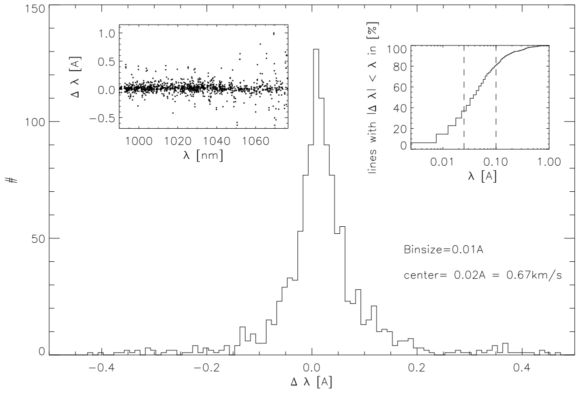

Figure 8.6: Histogram of the residuals between computed line positions and observed ones. In the upper left corner, the residuals are plotted against wavelength. In the upper right corner, the fraction of lines with residuals lower than a certain value are plotted. The left dashed line represents the accuracy of the wavelength solution which is 0.025 Å, the right one the detection boundary of 0.1 Å .

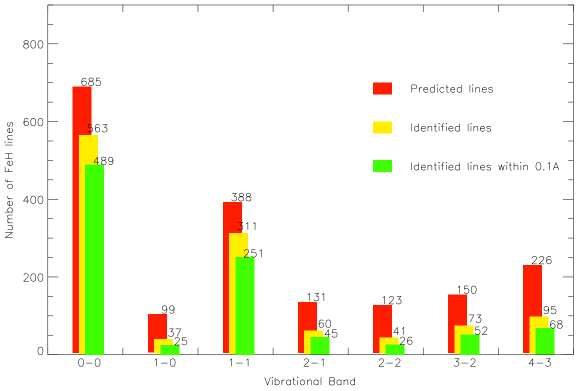

Figure 8.7: Histogram of predicted and identified FeH lines in the GJ1002 spectrum.

by their positions, which do not deviate by more than 0.1Å from the predictions. Where the residuals are larger than 0.025 Å the uncertainties in the molecular constants which were used to compute the FeH line list are responsible for these deviations.

For this analysis I used only lines with $W_\lambda > 2\,\mathrm{m\AA}$, which approximately describes a line with 2 % relative flux and a FWHM of 0.1 Å. I ignored lines with smaller contributions because their intensities are similar to the noise level. However, only 167 lines out of 1359 have equivalent widths less than 2 mÅ.

Vibrational Bands

From Fig. 8.2 I expect that the dominant vibrational bands are $(0,0)$ and $(1,1)$ from the $\Delta v = 0$ sequence, and $(3,2)$ and $(4,3)$ from the $\Delta v = 1$ sequence. In Fig. 8.7 a histogram with the number of identified lines for each vibrational band is presented, which shows that the expected vibrational bands are present. Also the number of possible lines from theory with $W_\lambda > 2\,\mathrm{m\AA}$ in the observed wavelength region is shown. This number is based on line-by-line computation of W_λ. In this histogram the bars in the foreground take into account only the lines identified by their positions.

Coincidence-by-Chance Method

For the lines with residuals smaller than 0.1 Å I computed the coincidence-by-chance factor C from Eq. 8.8. In Table 8.3 the values of C, w, N, and M are given for all identified bands. For the $(0,0)$ and $(1,1)$ transition, the number of identified lines N exceeds the number of coincidences

Table 8.3: Results from the coincidence method for lines with $W_\lambda > 2\,\mathrm{m\AA}$.

Band	Wavelength [Å]	C	w [#/Å]	N (M)
$(0,0)$	9900 – 10762	360	3.73	489 (658)
$(1,0)$	9901 – 10759	52	3.74	25 (99)
$(1,1)$	9941 – 10759	208	3.71	251 (388)
$(2,1)$	9931 – 10706	68	3.76	45 (131)
$(2,2)$	10480 – 10764	65	3.81	26 (123)
$(3,2)$	9910 – 10764	79	3.78	52 (150)
$(4,3)$	9905 – 10673	119	3.75	68 (226)

by chance C, which is a clear indication that these bands are present in the investigated region. For the other bands the situation is not as clear and I will confirm them with more investigations.

Cross-Correlation Method

I used cross-correlation techniques to investigate the agreement between the theoretical line list and the observed spectra. As a reference and a test, I cross-correlated a computed spectrum from this theoretical line list, which is broadened by an instrumental profile with a resolving power of 70 000, with the original line list (e.g. Fawzy, 1995; Fawzy et al., 1998). To be specific, I varied the theoretical positions with steps of $\Delta\sigma = 0.0125$ Å in a range of 0.375 Å and measured the relative intensity at the different positions weighted with W_λ of the line and integrate over all lines. I then normalized the results with the number of lines in the line list. I did this for all lines in the vibrational bands that are found in the M-dwarf spectra (see Fig. 8.8). If a vibrational band is present, a peak around zero appears above the noise produced by random coincidences with other lines.

I produced three different curves. For the first one, I used all possible lines from the original line list for comparison with the observed stellar spectrum (solid line in Fig. 8.8). For the second curve I computed a reference curve by cross-correlating the original line list with a synthetic spectrum computed from it (dashed line in Fig. 8.8). This case produces the maximum possible correlation. A third curve is produced with the corrected line list containing only identified FeH lines which I compared with the observed stellar spectrum (dotted line in Fig. 8.8).

As expected, for the synthetic spectrum with the theoretical line list (dashed line), all bands show clear peaks above the noise. For the observed spectrum (solid line) and original line list, the $(0,0)$ and $(1,1)$ vibrational bands show clear peaks above the noise, which agrees with the coincidences by chance values in Table 8.3. After improving the FeH line list (dotted line), all bands show peaks above the noise similar to the peaks obtained in the reference case from cross-correlating the theoretical line list with the computed spectra. The original theoretical line positions for the $(1,0)$, $(2,1)$, $(2,2)$, $(3,2)$, and $(4,3)$ bands are not accurate enough to show significant peaks in the cross correlation. To confirm the identifications, I also used the line strength in the next section.

Line Intensity Method

I used the method described in Sec.8.2 to test if the tentatively identified observed FeH lines can be identified with the theoretical ones. I plot $\log_{10} W_\lambda / S\lambda_0^4$ against E_0 (see Eq. 8.13) for the identified vibrational bands, branches, and Ω, with an appropriate estimated error (see Fig. 8.9).

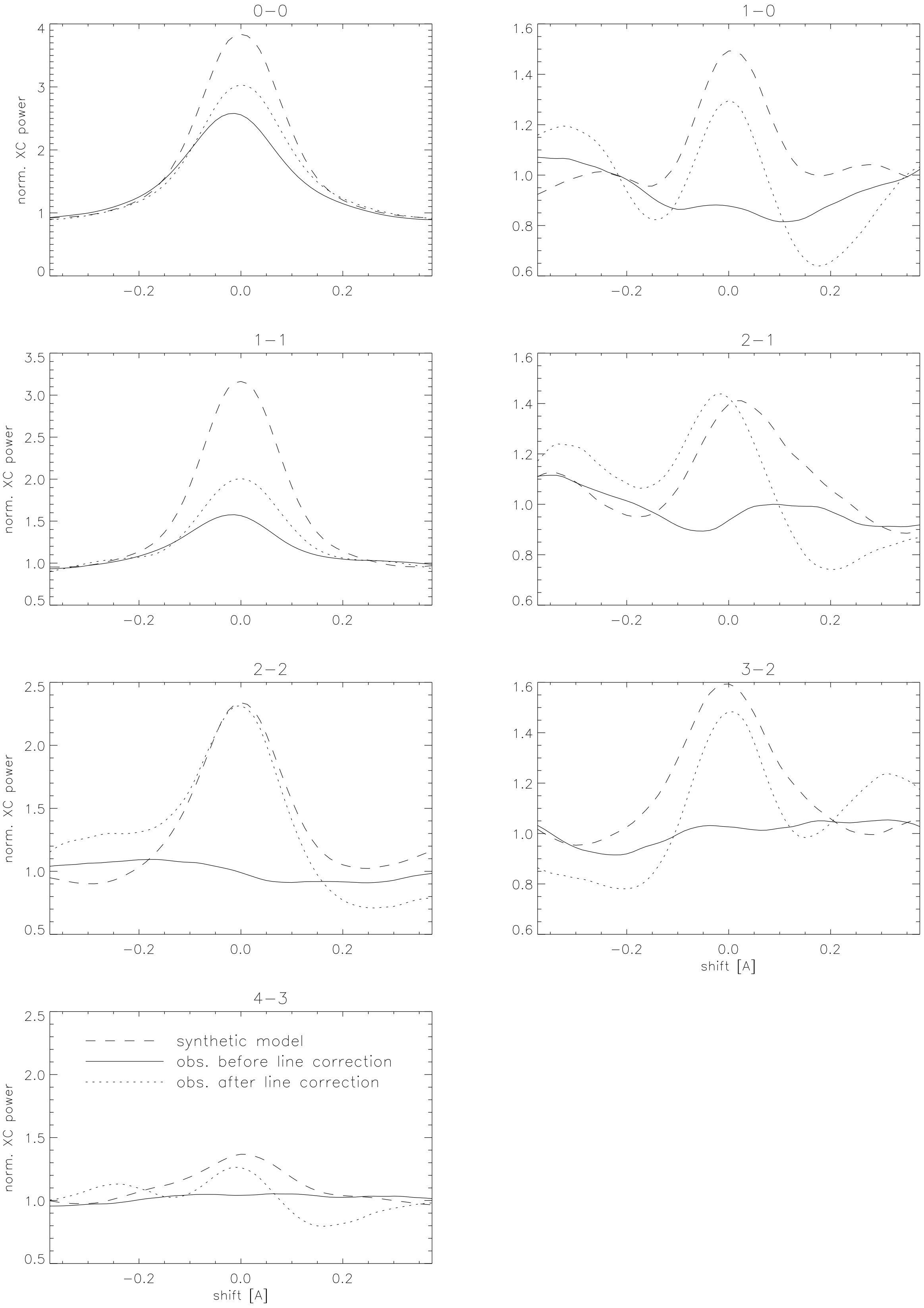

Figure 8.8: Cross-correlation curves for different vibrational bands.

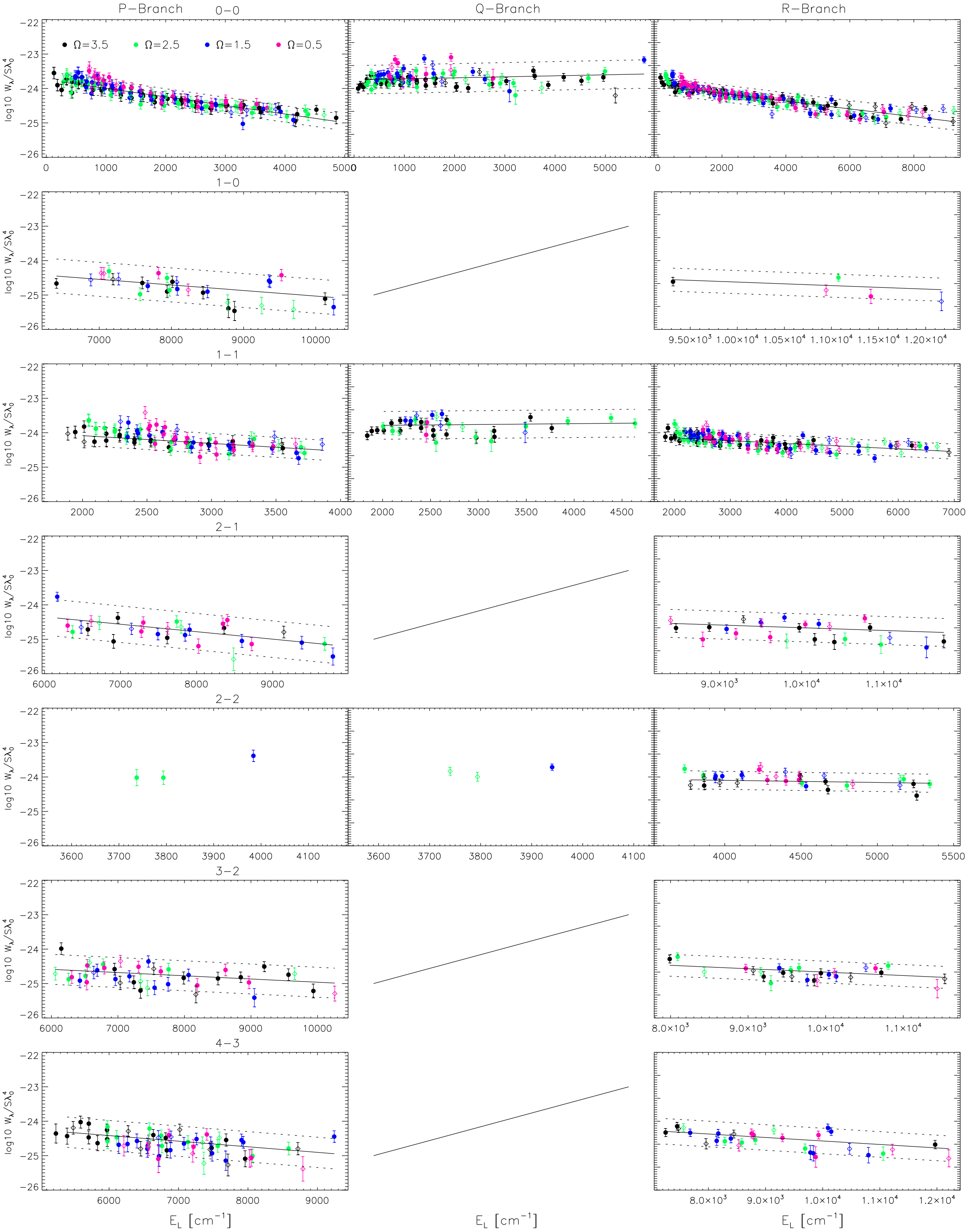

Figure 8.9: Logarithm of observed equivalent width and theoretical line strength against lower level energies. In each plot, a linear fit to the data is shown. Different colors of the data points belong to different Ω values. Dots represent lines which are identified within 0.1 Å, and diamonds lines which differ more than 0.1 Å from the theoretical position. The dotted lines represent the three σ scatter around the fit.

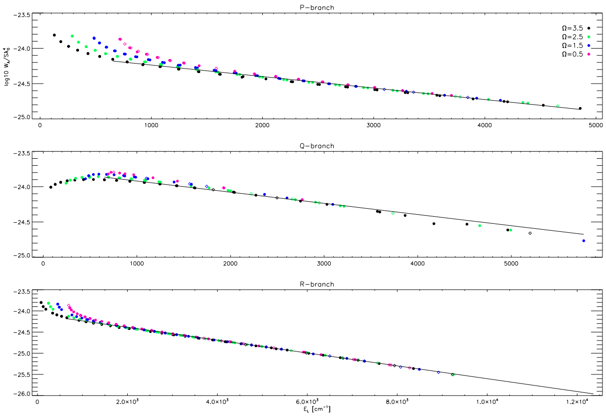

Figure 8.10: Logarithm of the computed equivalent width and theoretical line strength against lower level energies for the (0, 0) band. In each plot a linear fit to the data is shown. Different colors of the data points belong to different *Ω* values. Dots represent lines which are identified within 0.1 Å, and diamonds lines which differ more than 0.1 Å from the theoretical position.

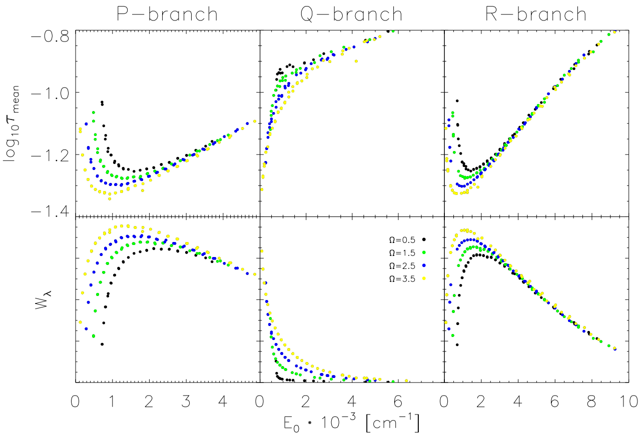

Figure 8.11: $\log_{10}\tau_{mean}$ and W_λ are plotted as a function of lower state energy for computed FeH lines from the (0, 0) band for the three branches.

In almost all cases a linear correlation is visible. In some cases where lines with small J are present, a deviation from the straight line can be seen. This deviation is expected because of the different formation heights for the FeH lines. I calculated model plots with synthetic lines, which reproduce this behavior in detail (Fig. 8.10). The computations are very similar to the observations, which supports the assumption of different heights of formation. To test this assumption, I computed the contribution function for the FeH lines (Magain, 1986) and used them to determine a weighted mean of the continuum optical depth, τ_{mean}. The latter describes a representative atmospheric line formation depth. In Fig. 8.11, I plot W_λ and τ_{mean} against E_0 for each branch from the (0, 0) band. These plots show clearly that the P- and R-lines with low and very high E_0 originate in deeper layers than the lines with medium E_0. It was also seen that the lines with low and high E_0 are the ones with small W_λ, because the Hönl-London factors for P- and R-lines are proportional to J_l and hence the lines become stronger for high J_l, but they also decrease for high J_l due to their increasing E_0s. Hence, there is a maximum in W_λ for medium J_l. For Q-branch lines the situation is different. The Hönl-London factors decrease with increasing J_l and hence the line strength monotonically decreases with J_l. In this case, the lines with low E_0 are the lines with the largest W_λ, and accordingly these lines are formed in higher layers and the Q-branch shows the opposite behavior to the P- and R-branches in the $\log_{10}\frac{W_\lambda}{S\lambda_0^4}$ plot.

I can conclude that in deeper layers, where weak lines are formed, the equivalent width is enhanced by the larger number of FeH molecules that contribute to the absorption (see Fig. 8.12). The molecule number increases towards deeper layers because of the higher overall density even though the concentration of FeH molecules relative to Fe and H decreases. Towards higher temperatures in deeper layers or in hotter stars, the number of FeH molecules would decrease

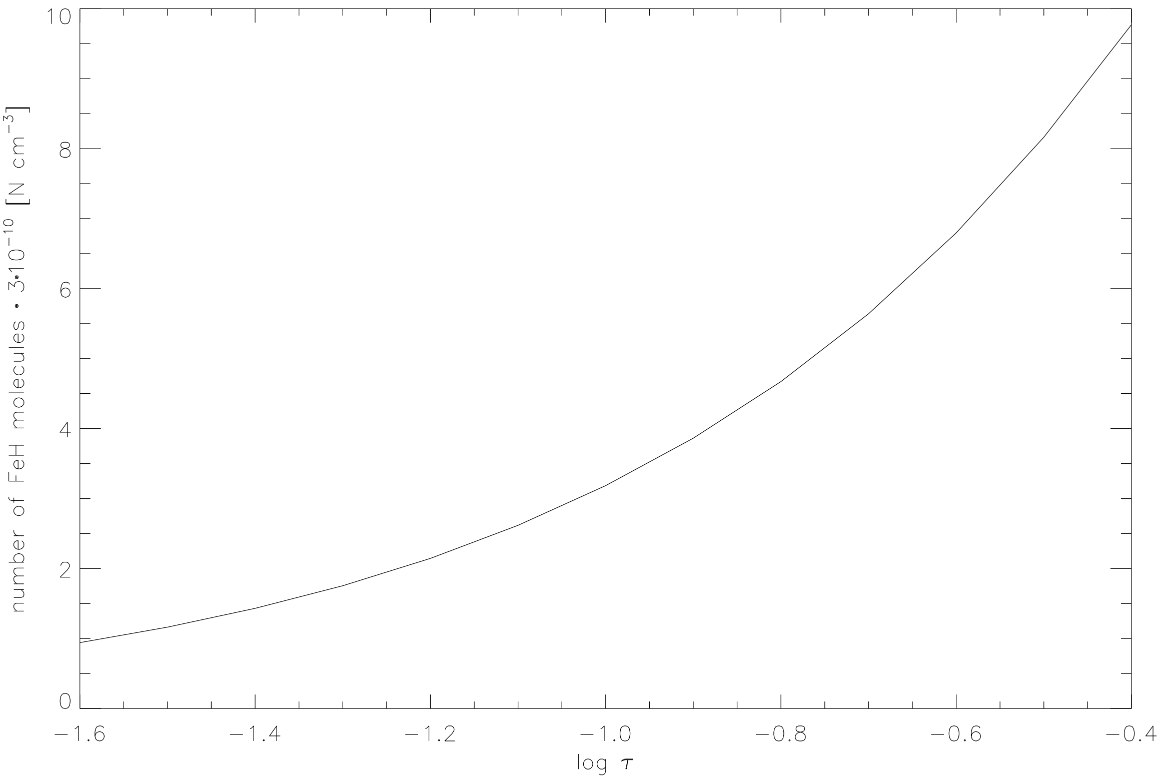

Figure 8.12: The number of FeH molecules as a function of optical depth in the region where the FeH absorption lines are formed.

again due to the ionisation of Fe, which is then no longer available for the formation of the molecule. In this case, this behavior results in a deviation from a straight line in Fig. 8.9

With this knowledge, one can use the line strength to confirm the identification of FeH . In Fig. 8.9, clearest correlations are found for the $(0, 0)$ and $(1, 1)$ bands, which also have the largest number of lines, but also for the P-branch of the $(1, 0)$ and $(2, 1)$ transitions and the R-branch of the $(2, 2)$ transition. The $(3, 2)$ and $(4, 3)$ transitions also show linear correlations but with a larger scatter. This result is a strong indication that all the identified bands are present in the observed spectra. Although the Q-branches of the $(0, 0)$ and $(1, 1)$ bands show no clear linear dependence for large E_0, I expect them to be present and correctly identified, because they show the expected downward trend for low energies. The scatter towards higher energies is much larger than in the other branches, and there are only a few measurements. The slope seems to be positive, but one could expect it to be negative if more data points were available.

I fitted the data points linearly for lines with $J_l > 7$ (to avoid the region where the influence of variable FeH number is too strong) and used the difference of the data points from the fit as a measure for the confidence of an identified line. A line is classified as “P” if the difference between $\log_{10} \frac{W_\lambda}{S\lambda_0^4}$ and the linear fit is smaller than three times the standard deviation σ of the scatter around the fit. But I assume that lines with $J \leq 7$ are also present, because they exactly show the expected behavior. It is classified as “Pb” if the deviation is greater than σ and the data point is above the linear fit, and as “R” if it is below.

Table 8.4: FeH molecular data of the identified lines. The columns are described in more detail in the appendix.

λ_{obs}	λ_{theo}	v_l	v_u	Ω_l	Ω_u	J_l	J_u	B	A	s_A	E_l	$\Delta\lambda$	blend	class	comment
9900.4846	9900.4902	0	0	3.5	3.5	17.5	18.5	3	470924.44	0.8309	0.225	0.0056	1.000	P	
9901.1049	9901.1175	0	0	3.5	3.5	14.5	15.5	3	462792.47	1.0695	0.154	0.0126	1.000	P	
9901.4704	9901.4116	0	1	3.5	3.5	32.5	31.5	1	133973.65	0.3378	0.794	-0.0588	1.000	P	
9903.9631	9903.9809	0	0	3.5	3.5	18.5	19.5	3	472886.88	1.1484	0.252	0.0178	0.998	P	
9904.9843	9904.9913	0	0	3.5	3.5	13.5	14.5	3	458947.25	1.4267	0.134	0.0070	1.000	P	
9905.8556	9905.8940	0	0	3.5	3.5	15.5	16.5	3	466010.13	1.1121	0.177	0.0384	0.969	P	
9905.8556	9905.8940	3	4	3.5	3.5	5.5	4.5	1	93477.74	1.1121	0.649	0.0384	0.026	P	
9905.8556	9905.8940	3	4	3.5	3.5	5.5	4.5	1	93477.74	1.1121	0.649	0.0384	0.026	P	
9906.2993	9906.3258	0	0	3.5	3.5	14.5	15.5	3	462784.17	1.2660	0.155	0.0265	1.000	P	
9906.6069	9906.6202	0	0	3.5	2.5	13.5	12.5	1	16687.29	2.8524	0.134	0.0133	1.000	Q	
9907.7184	9907.7489	0	0	3.5	3.5	16.5	17.5	3	468735.58	0.8068	0.201	0.0305	1.000	P	
9908.8070	9908.8092	0	0	2.5	2.5	10.5	11.5	3	459216.45	1.7090	0.116	0.0022	0.479	P	
9908.8070	9908.8387	0	0	3.5	3.5	13.5	14.5	3	458903.98	1.7090	0.134	0.0317	0.521	P	
9909.0854	9909.1136	0	0	2.5	2.5	9.5	10.5	3	453849.43	1.5113	0.100	0.0282	0.975	P	
9909.7148	9909.7519	0	0	2.5	2.5	11.5	12.5	3	463304.45	1.1935	0.134	0.0371	0.996	P	
9909.9442	9909.9778	0	0	3.5	3.5	18.5	19.5	3	473102.19	0.7455	0.253	0.0336	1.000	P	
9910.5238	9910.4688	0	0	3.5	3.5	12.5	13.5	3	454224.51	1.3628	0.115	-0.0550	0.466	P	
9910.5238	9910.5376	2	3	2.5	2.5	20.5	19.5	1	169779.53	1.3628	0.776	0.0138	0.053	P	
9910.5238	9910.5769	0	0	2.5	2.5	8.5	9.5	3	446648.26	1.3628	0.086	0.0531	0.408	R	class $\neq s_A$
⋮	⋮	⋮	⋮	⋮	⋮	⋮	⋮	⋮	⋮	⋮	⋮	⋮	⋮	⋮	⋮

It is classified as "Q" if the line could not be investigated because, I only investigated lines with $\Delta\Omega = 0$. I give a list of all identified lines with quantum numbers and corrected wavelength in Table 8.4. This list is explained in more detail in the appendix and available in its full length in the online material of Wende et al. (2010) or here [6].

8.3.3 Corrections to the Line Strengths

If one wishes to use Eq. 8.17 to correct for the differences in line depth, one have to match the stellar parameters as closely as possible. These parameters are basically effective temperature, surface gravity, and chemical composition, as well as van der Waals-broadening constants, whose influence becomes significant at these low temperatures. The van der Waals broadening was computed with Unsöld's hydrogenic approximation, and an enhancement factor was used to model the line wings correctly. Because no enhancement factor is reported for FeH, I needed to determine one. For M-type stars, an assumed surface gravity of $\log g = 5.0$ is standard and the chemical composition is usually assumed as solar. To match the strong Ti lines in the 10 300–10 700 Å region as well as the FeH lines, we increased the iron abundance from 7.41 to the Grevesse & Anders (1989) value of 7.63. I used this scaling as a parameter and do not claim this to be the actual iron abundance of GJ1002. The free parameters for GJ1002 are now T_{eff}, the van der Waals-broadening enhancement factor (which I call from now on β_{vdW}), and the instrumental resolving power, which I used as a fitting parameter to account for possible additional rotational broadening. These three parameters are strongly correlated. I created χ^2 maps to determine the most likely combination that best matches the observed spectra.

χ^2 Maps

For the comparison between observation and computation I chose a region where the original line list fits best, the lines are strongest and consequently the influence of van der Waals broadening is largest. I selected the first 100 Å from the $(0,0)$ band head at 9900 Å . For the computations I used the new line list with corrected positions and also included the identified atomic lines. To create the χ^2 maps for the three combinations of parameters, I searched for the minimum for each parameter (light cross in left plots in Fig. 8.13) and used this value to construct the χ^2 map for the other two parameters. The χ^2 maps (right hand side in Fig. 8.13) yield a consistent picture of the parameter combinations for the spectra of GJ1002.

Since the signal to noise is almost constant in the used region, I excluded it and scaled the residuals between observation O and computation C with the observed value $\chi^2 = \sum \frac{(O-C)^2}{O}$.

The most likely parameters for effective temperature, resolving power, and β_{vdW} are 3100 K, 70 000 and 1.75, respectively. It is obvious, however, that the χ^2 curves show regions with broad minima which would allow for variations in the derived parameters.

Because the observed spectra are supposed to have a resolving power of 100 000, the difference to the determined resolving power stems probably from rotation, which is measured to be lower than $3\,\mathrm{km\,s^{-1}}$, but not necessarily zero. The difference in resolving power results in $v \sin i \approx 1.3$ km $\mathrm{s^{-1}}$ at a wavelength of 10 000 Å .

An independent constraint for the instrumental resolving power and effective temperature is given by the Ti lines, which are strong and distributed over a wide wavelength range in the spectra. The computation of these lines with the parameters and broadening constants given by VALD fits the observations within 5 % for the line depth. This gives us confidence that the

---

[6] `http://www.astro.physik.uni-goettingen.de/~sewende/`

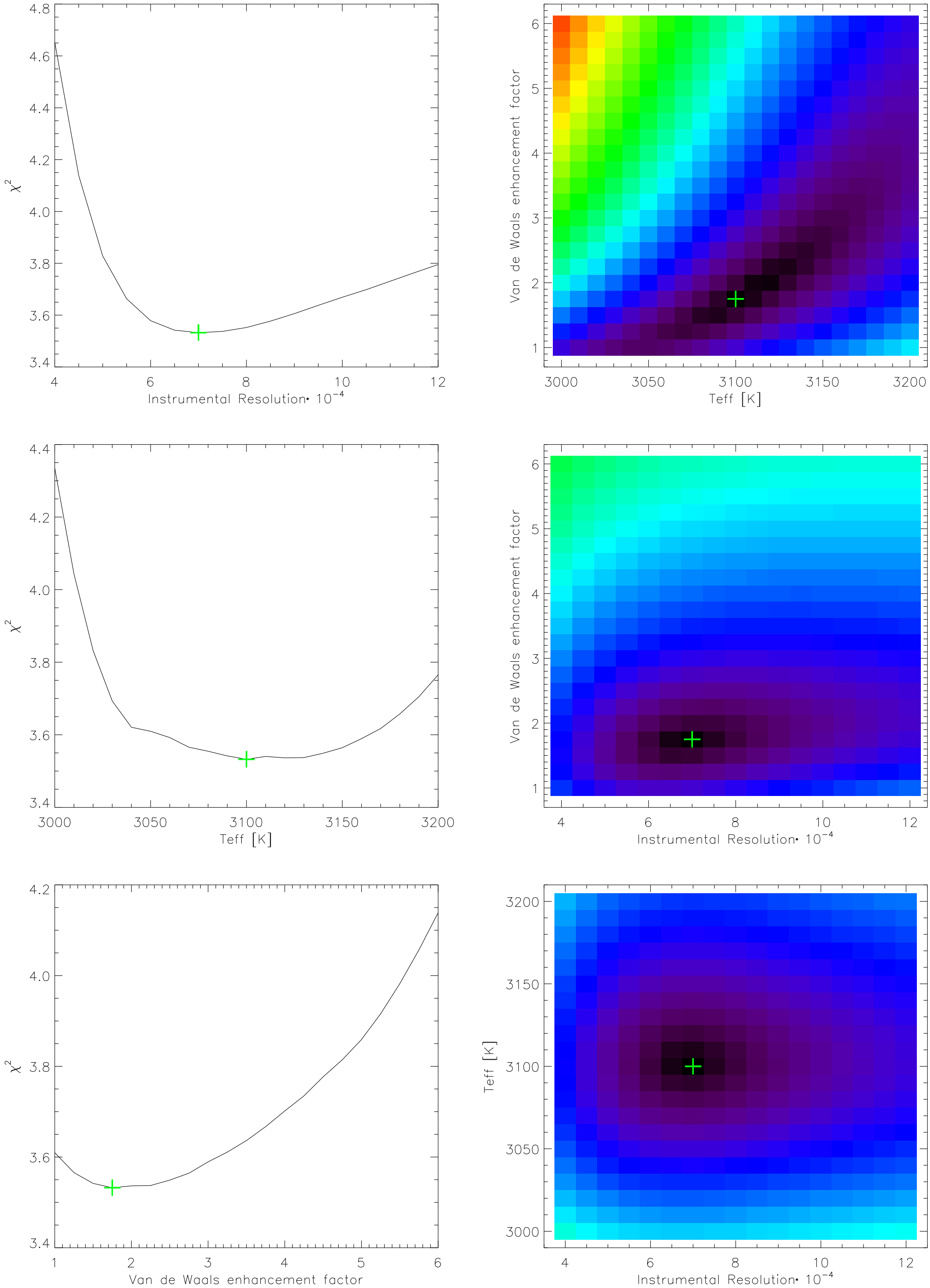

Figure 8.13: Left: Minima in χ^2 plots for the resolving power, $T_{\rm eff}$, and β_{vdW} (from top to bottom). Right:χ^2 maps for the three parameter combinations, $\beta_{vdW} - T_{\rm eff}$, β_{vdW} – resolving power, and resolving power – $T_{\rm eff}$ (from top to bottom). The χ^2 maps are computed for the minimum value of the leftover parameter on the left hand side.

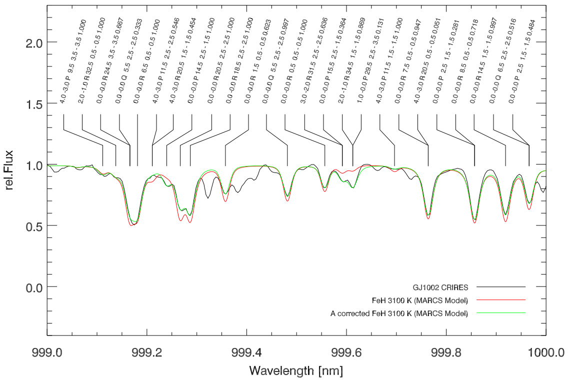

Figure 8.14: Observed spectrum of GJ1002 (black) and computed one before A correction (red) and after A correction (green) labeled with quantum numbers (both with corrected positions).

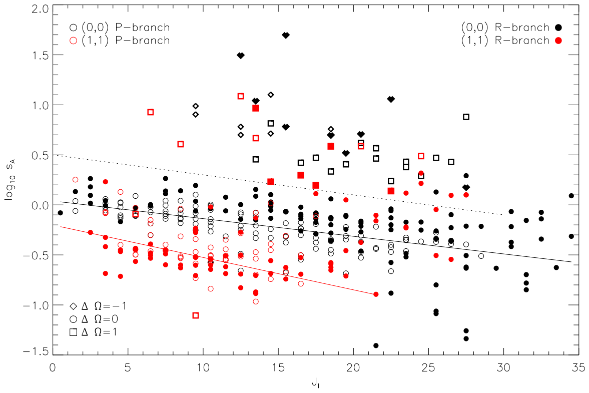

Figure 8.15: Scaling factor for the Einstein A values against rotational quantum number for the $(0, 0)$ and $(1, 1)$ bands. The plot is truncated at $J_l = 35$ for better visibility.

decreasing line depth of the FeH lines with increasing wavelength is a real feature and not due to normalization effects.

Einstein A Values

To correct for the Einstein A values I used computed spectra, which already have corrected line positions. I iteratively adjusted the Einstein A values because for saturated lines the first scaling is not sufficient. The scaling factors for each line are listed in Table 8.4, and an example for the corrected computed spectra is shown in Fig. 8.14. To estimate an error, I assumed an accuracy of 1% for the observed line depth, which results in an error of $\sim$ 3% for the scaling factors. If I furthermore assume that the line depth is modified by an unknown blended feature by, e.g., 5%, an error of $\sim$ 16% follows. The accuracy of the Einstein A scaling is also influenced by the van der Waals-enhancement factor β_{vdW}. A change of ±1 gives a mean difference of $\sim$ 5% in the scaling constants, but can be up to 30% for individual lines, due to the logarithmic ratio of the intensities (see e.g. Eq. 8.17).

I obtained a good fit to the data with the scaled Einstein A values even for some lines that were calculated to be very weak. Yet this results in some cases in unrealistic $\log gf$ values, and I assume that these weak lines are blended with unknown components. The scaling of line blends is a difficult problem because it results in equal scaling factors for lines with completely different quantum numbers. To avoid this problem one could determine scaling factors for each branch, but I chose the simpler scheme of scaling each line. I use Eq. 8.17 and plot s for the Einstein A values against J_l to search for a possible rotational dependence (Fig. 8.15). I plot only scaling factors for the $(0, 0)$ and $(1, 1)$ bands, because these are the bands with the largest number of lines, and I used only lines which contribute more than 99 % to a blended line feature to avoid contributions from incorrectly scaled lines.

Two groups of scaling factors were found. One group describes a strong enhancement of the line depths (‘positive’ scaling factors) and the other only a small enhancement for low J_l and a reduction towards lines with high J_l (‘negative’ scaling factors). I divide these two groups by a dashed line in Fig. 8.15. For the $\Delta\Omega = 0$ transitions of the $(0, 0)$ and $(1, 1)$ bands I include linear fits to the data in Fig. 8.15 to indicate the slope.

The group of positive scaling factors is strongly dominated by $\Delta\Omega \pm 1$ transitions (diamonds and rectangles), while the group of negative scaling factors consists of only $\Delta\Omega = 0$ transitions (circles). The latter scaling factors for $(0, 0)$ and $(1, 1)$ bands (black and red circles, open for P-branches and filled for R-branches) show an almost linear behavior with J_l and become stronger towards higher J_l. The positive scaling factors also show two linear groups, which originate from the $(1, 1)$ band (red rectangles) and from the $(0, 0)$ band (black diamonds and rectangles). These scaling factors describe a strong enhancement of the lines for low J_l and become smaller towards high J_l. All groups of scaling factors have a similar negative slope, and are only shifted by a constant factor to higher or lower scaling factors.

The distribution of other bands and lines that contribute less than 99 % to a blended feature gives only a larger scatter to the data points, but does not change the basic trend of the scaling factors. I conclude that the J_l dependence in the scaling factors likely indicates shortcomings in the calculated Hönl-London factors. In particular, satellite branches with $\Delta\Omega \pm 1$ are much stronger than expected for Hund's case (a). In other words, the two $^4\Delta$ electronic states are heavily mixed with other electronic states and the simple Hund's case (a) behavior anticipated for isolated electronic states with relatively large spin-orbit splittings is not found.

Chapter 9

Temperature Estimations Using FeH

The determination of effective temperatures in cool stars is, in general, a difficult task. I will present two different approaches of using FeH molecular lines to measure the effective temperature in M dwarfs.

9.1 Rotational Temperatures as a Measure of Atmospheric Temperatures

A rotational temperature T_{rot} can be obtained from the slope m of the linear fit in the $[\log_{10} W_\lambda/S, E_0]$ diagram (Fig. 8.9) using Eq. 8.13 described in the above section. T_{rot} can then be calculated from

$$T_{rot} = \frac{hc}{mk}\log_{10} e. \tag{9.1}$$

For the fit to the data, only lines with $J_l > 7$ are used, to avoid the significant influence from a varying absorber number, and neglected lines with a line depth greater than 0.5 to avoid saturation effects. Owing to the large errors of the slope of the linear fit in Fig. 8.9, only rotational temperatures with moderately small one-sigma errors are considered (see Fig. 9.1). Systematically lower temperatures are found for the P-branches in comparison to the R-branches, which is consistent with different heights of formation for most of the lines in a branch (Fig. 8.11).

If one computes the weighted mean of the rotational temperatures (grey solid line in Fig. 9.1) using the 1σ-error (grey dashed-line in Fig. 9.1), one obtains $\overline{T}_{rot} \approx 3200 \pm 100\,\mathrm{K}$. This is in the middle of the expected temperature range for this spectral type (3000 K–3300 K; dashed-dotted lines in Fig. 9.1) and is close to the estimated value of $\sim 3100\,\mathrm{K}$. The main contribution to $\overline{T}_{rot}$ stems from the P- and R-branches of the $(0, 0)$ transition due to their small uncertainties. The weighted mean of the P- and R-branches are $\overline{T}^P_{rot} \approx 2600 \pm 150\,\mathrm{K}$ and $\overline{T}^R_{rot} \approx 3750 \pm 150\,\mathrm{K}$, respectively.

It should be pointed out, that the temperature obtained, even for a single branch in a band, is an average over the individual excitation temperatures for each line. The resulting temperature crucially depends on the selection of the lines that are used: if one uses lines with similar equivalent widths and lower energy levels, then one could obtain temperatures for certain regions in the atmosphere. However, for this method a large number of lines is required; otherwise the uncertainties become too large.

I conclude that in order to use the method of rotational temperatures, a large number of well measured lines are required to minimize the error in the slope. Finally, the rotational temperature

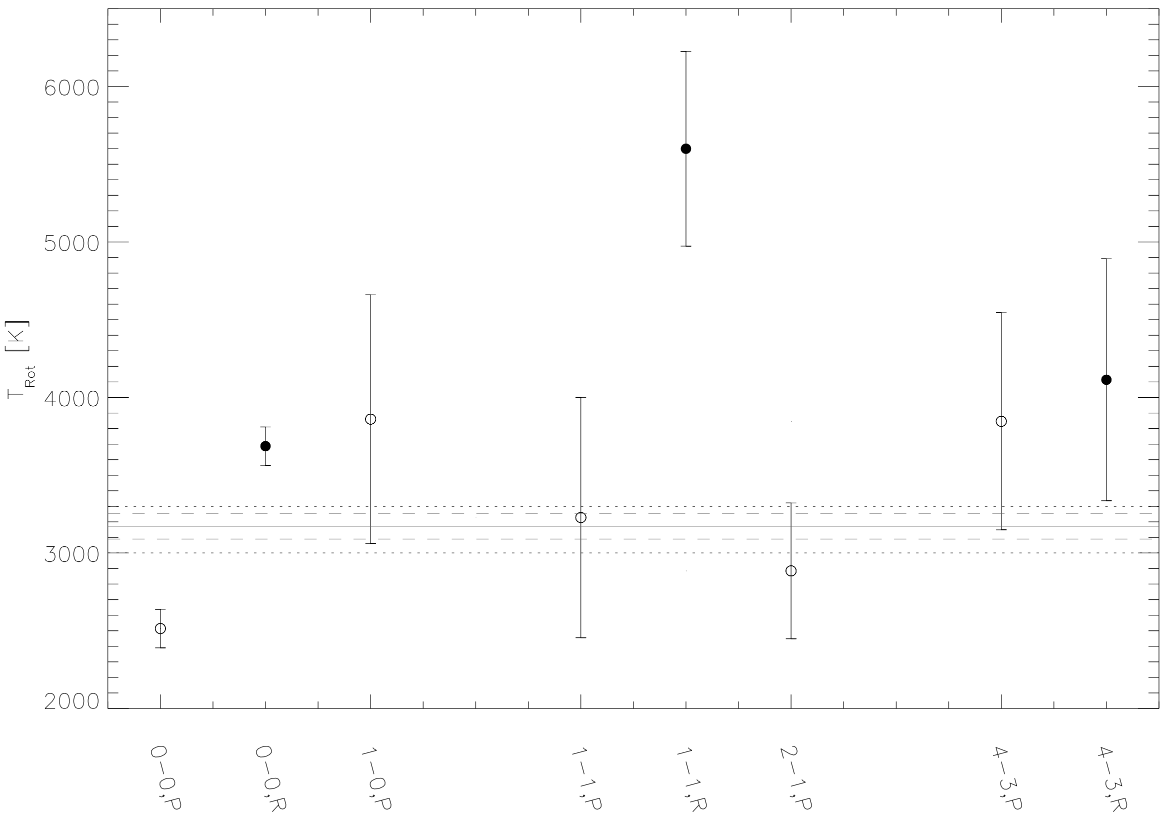

Figure 9.1: Rotational temperatures derived from the slope of the linear fits in Fig. 8.9. The error bars indicate the one sigma level. The dotted lines give the expected upper and lower effective temperatures for a 5.5 M-dwarf. The grey solid line is the weighted mean of the rotational temperatures with its one sigma error (dashed-line).

can only be expected to match the effective temperature if the lines form in a region around optical depth unity.

9.2 Deriving Effective Temperatures with the Line Ratio Method

9.2.1 Basic Idea

Using line ratios is a well-known method in atomic spectroscopy to derive excitation temperatures of spectral lines which can then be translated into effective temperatures. In equation (4.65), one can see that the absorption coefficient, and hence the intensity (see equation (4.66)), is temperature dependent due to population statistics. For two absorption lines from the same species (in this case from the FeH molecule), the logarithmic ratio of line intensities is given by,

$$\ln\left(\frac{I_1}{I_2}\right) = \frac{\alpha_1 l_1}{\alpha_2 l_2} = \left(\frac{S_1 l_1 N_1}{S_2 l_2 N_2}\right) e^{\frac{1}{kT}(E_2 - E_1)}. \tag{9.2}$$

In this relation, S_i is the line strength defined in section 4.4.4 which is constant for each line. N_i and l_i are the total number of FeH molecules and the path length through the atmosphere, respectively. Both are different for lines with different lower level energy E_i, since they originate

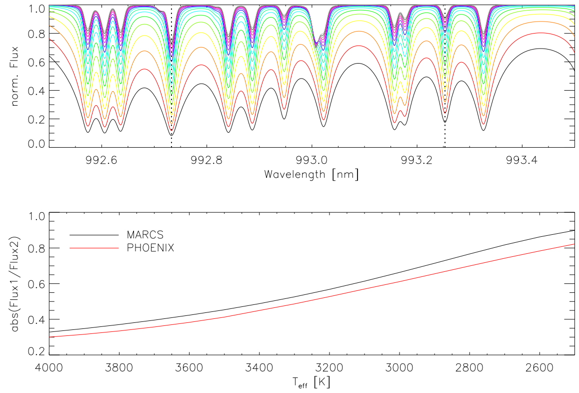

Figure 9.2: Upper panel: Computed spectra for a sequence of effective temperatures (from 2500 K–4000 K in steps of 100 K). The lines which are used for the line ratios are indicated by vertical dotts. Lower panel: Line ratios as a function of effective temperature for `MARCS` (black) and `PHOENIX` (red) atmospheres.

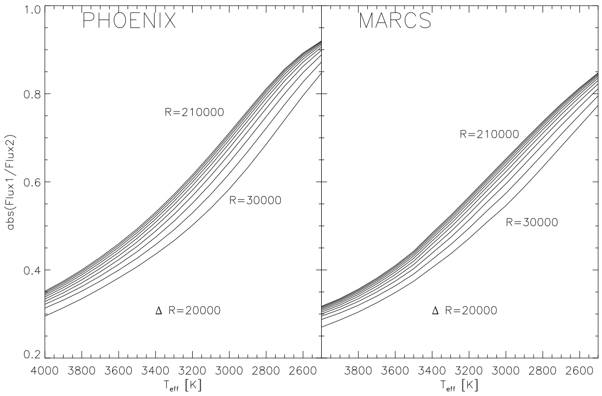

Figure 9.3: Line ratio as a function of effective temperature for different values of resolving power.

in different heights of formation (see section 8.3.2). This is mainly determined by the atmospheric structure, which, for given surface gravity and chemical composition, is governed by the effective temperature. Hence, the expression in brackets on the right hand side of equation (9.2) can be written as

$$R(T_{\mathrm{eff}}) = \left(\frac{S_1 l_1 N_1}{S_2 l_2 N_2}\right). \tag{9.3}$$

Showing that the ratio of two molecular absorption lines is, in first order, only dependent on effective temperature and can be used to measure it. The dominant change in the line ratio with changing excitation temperature is governed by the lower level energy difference $\Delta E = E_2 - E_1$ in the exponential function of equation (9.2), and becomes larger with increasing ΔE.

In order to demonstrate the dependence of line ratio on effective temperature, a pair of lines with $\Delta E = 0.05\,\mathrm{eV}$ was chosen and the line ratio for a sequence of effective temperatures was computed (see upper panel Fig. 9.2, the position of the lines used for the line ratio is marked by vertical dotted lines). These lines were chosen, since they are

- almost at the same position, in order to minimize continuum normalization effects,
- sufficient strong, even for high effective temperatures, and
- not strongly blended by neighboring lines.

The ratios of both lines for different T_{eff} are plotted in the lower panel of Fig. 9.2 for a set of `MARCS` and `PHOENIX` model atmospheres. They differ by an almost constant offset of about 0.05. This systematic offset can be translated into effective temperature and is of the order of 100 K. This difference results from slightly different atmospheric structures in both atmosphere species,

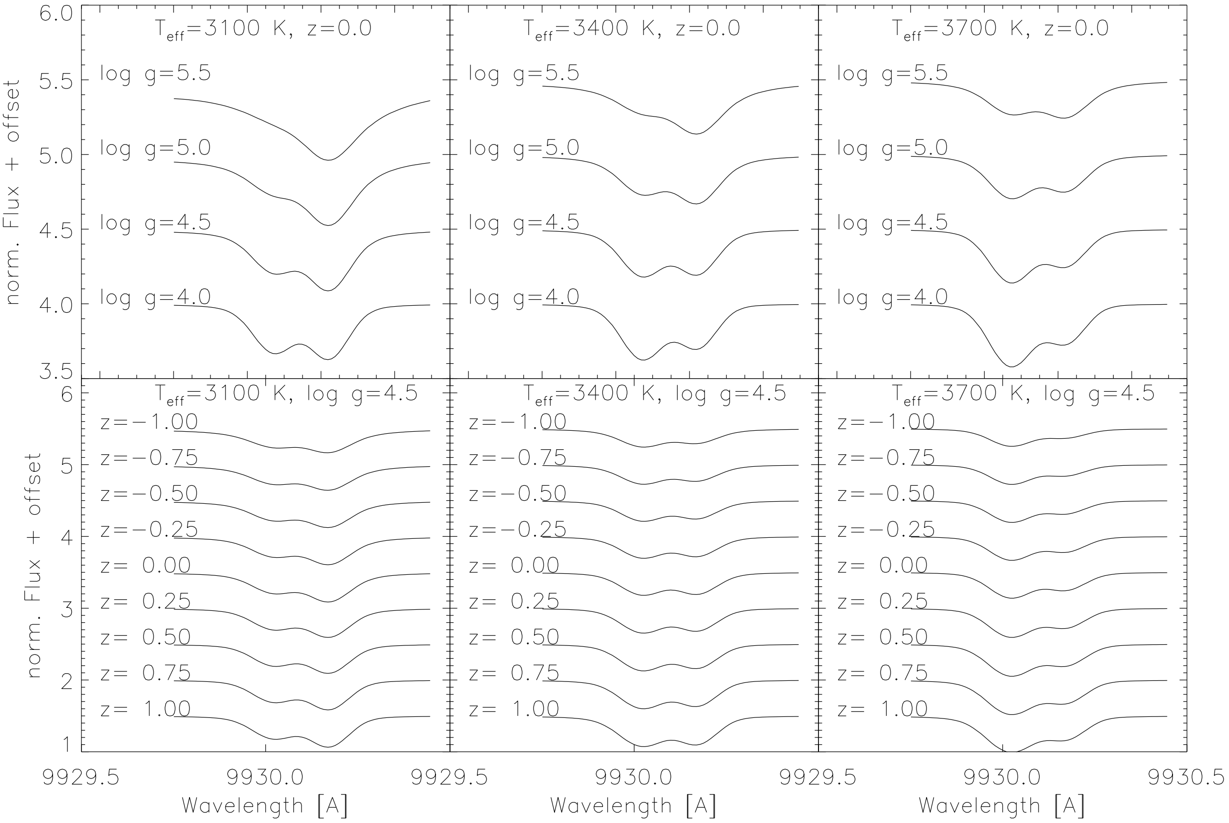

Figure 9.4: Ti-FeH pair for different effective temperatures and different metallicity (upper panel from left to right). Ti-FeH pair for different surface gravities and different metallicity (bottom panel from left to right)

i.e. different temperature stratification. In the following, the results from both atmosphere species will be investigated simultaneously.

The dependence of the line ratio from T_{eff} is also influenced by the resolution of the spectra. In Fig. 9.3, the line ratios are plotted for different values of resolving power R from 30 000–210 000 in steps of $\varDelta R = 20\,000$. This shows, that it is important to know the resolution of the investigated spectra, in order to obtain the right T_{eff} from the line ratio. Also rotational broadening has the same effect, but is not treated in this work.

9.2.2 First Results

A first test for this method is done with a set of high quality CES[1] spectra. The spectral range sample is from M0 – M5.5 dwarfs (see Table 9.1), though only appropriately, since FeH in the z-band tends to saturate for later type stars. The central intensity of the chosen line pair was measured by fitting a simple Voigt profile since noise made it difficult to determine the real center of the line. Then, the ratio were plotted against spectral type (see upper right inlay of Figs. 9.5 and 9.6). A linear trend is visible, even though for early M dwarfs the scatter becomes large. The determined ratios were then associated with an effective temperature, obtained from the line ratio computations shown in Fig. 9.2 (see lower left inlay of Figs. 9.5 and 9.6). In this step, the

---

[1] Data were taken at ESO Telescopes under the program 076.D-0092(A)

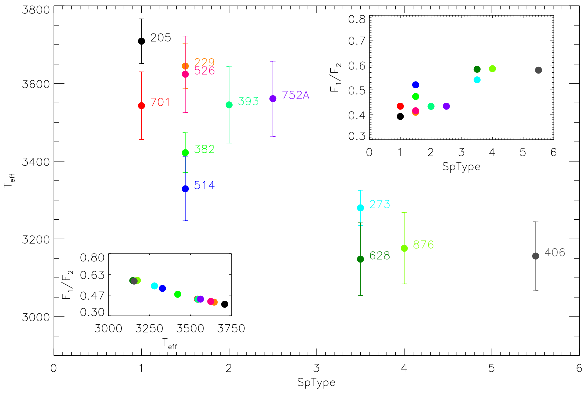

Figure 9.5: Effective temperatures determined from line ratios as a function of spectral type for a set of M dwarf CES spectra. In this plot, the `MARCS` atmospheres were used. In the upper right inlay, the line ratios are plotted against spectra type. In the lower left inlay, the line ratios are plotted against effective temperature.

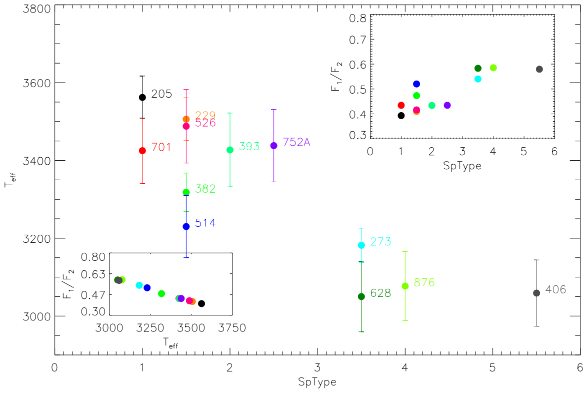

Figure 9.6: Same as Fig. 9.5, but `PHOENIX` atmospheres were used.

resolution of the spectra were taken into account. An estimate of the error could be derived from the error of the Voigt profiles. Finally, the effective temperatures obtained were plotted against spectral type in Figs. 9.5 and 9.6. Again, the scatter for early M type stars become large, but this could be due to wrong spectral classifications of these stars. In general there is an uncertainty of about ±1–2 spectral types.

Table 9.1: Derived stellar parameters. $\log g$ and metallicity are from the `PHOENIX` models for the set of M dwarfs in Figs. 9.7 ans 9.8. Reference temperatures are from Casagrande et al. (2008).

Name	Spectral Type	$T_{\rm eff}{}^{PHOENIX}$ [K]	$T_{\rm eff}{}^{MARCS}$ [K]	$\log g$ [cgs]	Fe/H	$T_{\rm eff}{}^{Ref}$ [K]
Gl205	M1.0	3562 ± 54	3709 ± 57	4.5	0.0	3520 ± 170
Gl701	M1.0	3425 ± 84	3543 ± 86	4.5	0.3	3557
Gl229	M1.0/M2.0	3506 ± 54	3645 ± 57	4.5	0.3	–
Gl382	M1.5	3318 ± 49	3422 ± 51	4.5	0.3	–
Gl514	M1.5	3230 ± 79	3329 ± 82	4.0	0.0	3242 ± 160
Gl526	M1.5	3488 ± 94	3624 ± 98	4.5	0.3	3636 ± 163
Gl393	M2.0	3427 ± 94	3545 ± 98	5.0	0.3	–
Gl752A	M2.5	3438 ± 93	3561 ± 96	5.0	0.3	3368 ± 137
Gl273	M3.5	3182 ± 44	3280 ± 45	4.5	0.0	–
Gl628	M3.5	3050 ± 90	3148 ± 93	4.5	0.3	–
Gl876	M4.0	3077 ± 88	3176 ± 91	5.0	0.3	–
Gl406	M5.5	3059 ± 85	3156 ± 87	5.5	0.0	2900

The derived effective temperatures were used to create spectra on `PHOENIX` and `MARCS` atmosphere models. In order to match the observed CES spectra best, the surface gravity and metallicity were adjusted. There were two criteria which should be fulfilled:

1. the FeH lines should fit in depth and width as well as possible; and
2. the shape of a Ti line at $\sim 9930\,\text{Å}$ and their neighboring FeH line at $9930.2\,\text{Å}$ should be resampled as well as possible.

The latter condition turned out to be a very good indicator of surface gravity. The characteristic shape is very sensitive to $\log g$, due to the much more strong dependence on surface gravity of the Ti line intensity, in comparison to the FeH line intensity. An example for three different T_{eff} is shown in the upper panel of Fig. 9.4. In the lower panel of Fig. 9.4, it is also visible that the shape of the Ti-FeH line pair varies only weakly with changing scaling of metallicity. Due to this, the way to fit the CES spectra with model spectra is the following:

1. choose a model spectra with T_{eff} obtained from the line ratio (since the atmosphere grids are available in 100 K steps, the temperature close to the line ratio temperature was chosen, within the errors);
2. adjust $\log g$ until it matches the characteristic shape of the Ti-FeH pair;
3. "fine tune" by changing the metallicity in order to fit the line depths as well as possible.

For all spectra except that of Gl406, which is strong Zeeman broadened, good results could be obtained (see Figs. 9.7 and 9.8). Adopting the effective temperatures from line ratio, one is able to measure $\log g$ and the chemical composition. The derived values are listed in Table 9.1. Comparisons with effective temperatures from Casagrande et al. (2008) show, that the temperatures derived with the line ratio method agree in general with those from Casagrande et al. (2008) (see Table 9.1).

In order to use this method in a more advanced way, one needs well resolved, high signal-to-noise spectra. There are other better suited line pairs redwards of 1 μm, which are not shown here. In order to use them, and determine line ratios of several line pairs, one needs spectra which extend towards longer wavelengths and access to model atmospheres matching the derived temperatures.

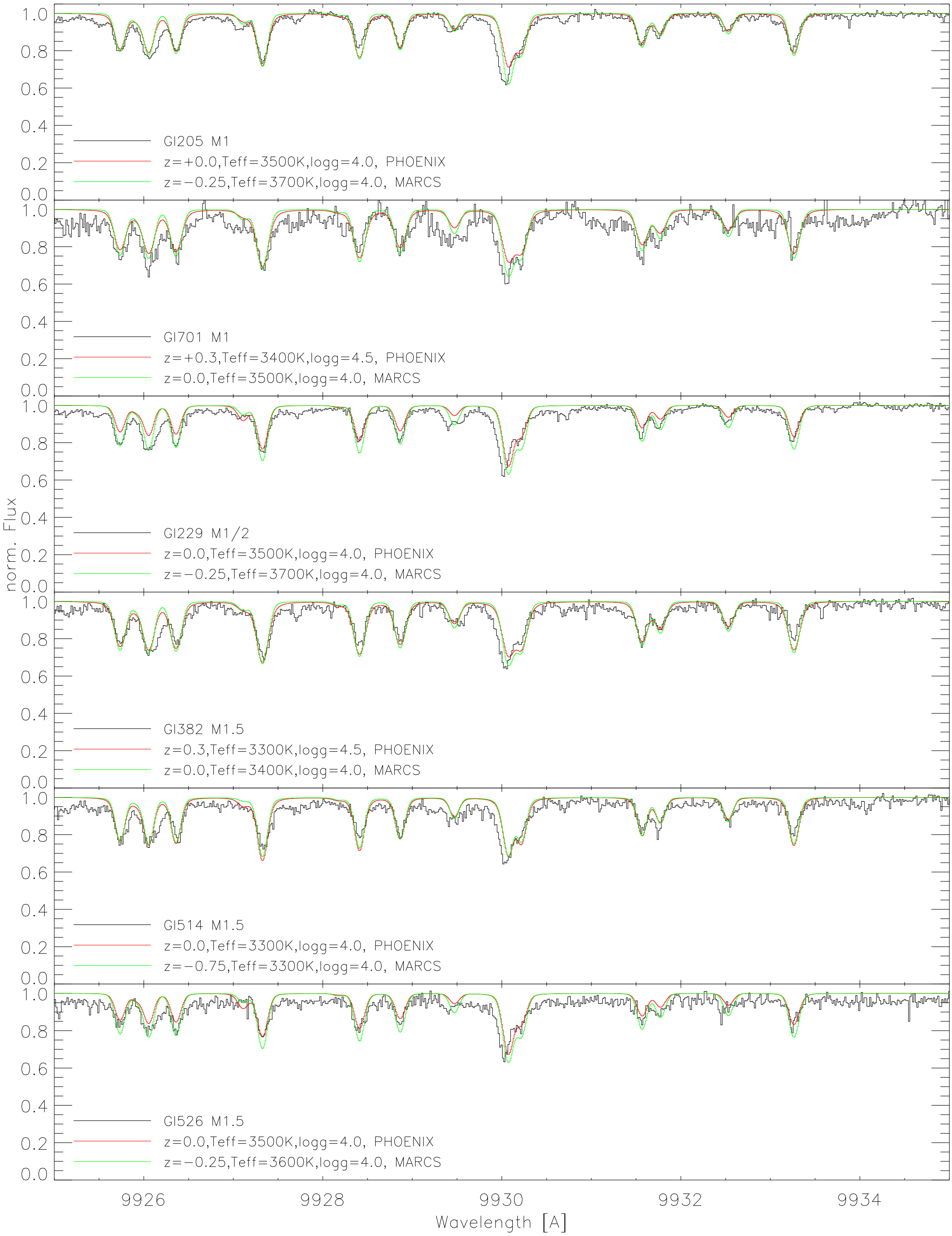

Figure 9.7: Spectra produced on `PHOENIX` (red) and `MARCS` atmospheres for the afore determined effective temperature in comparison with CES observations (black).

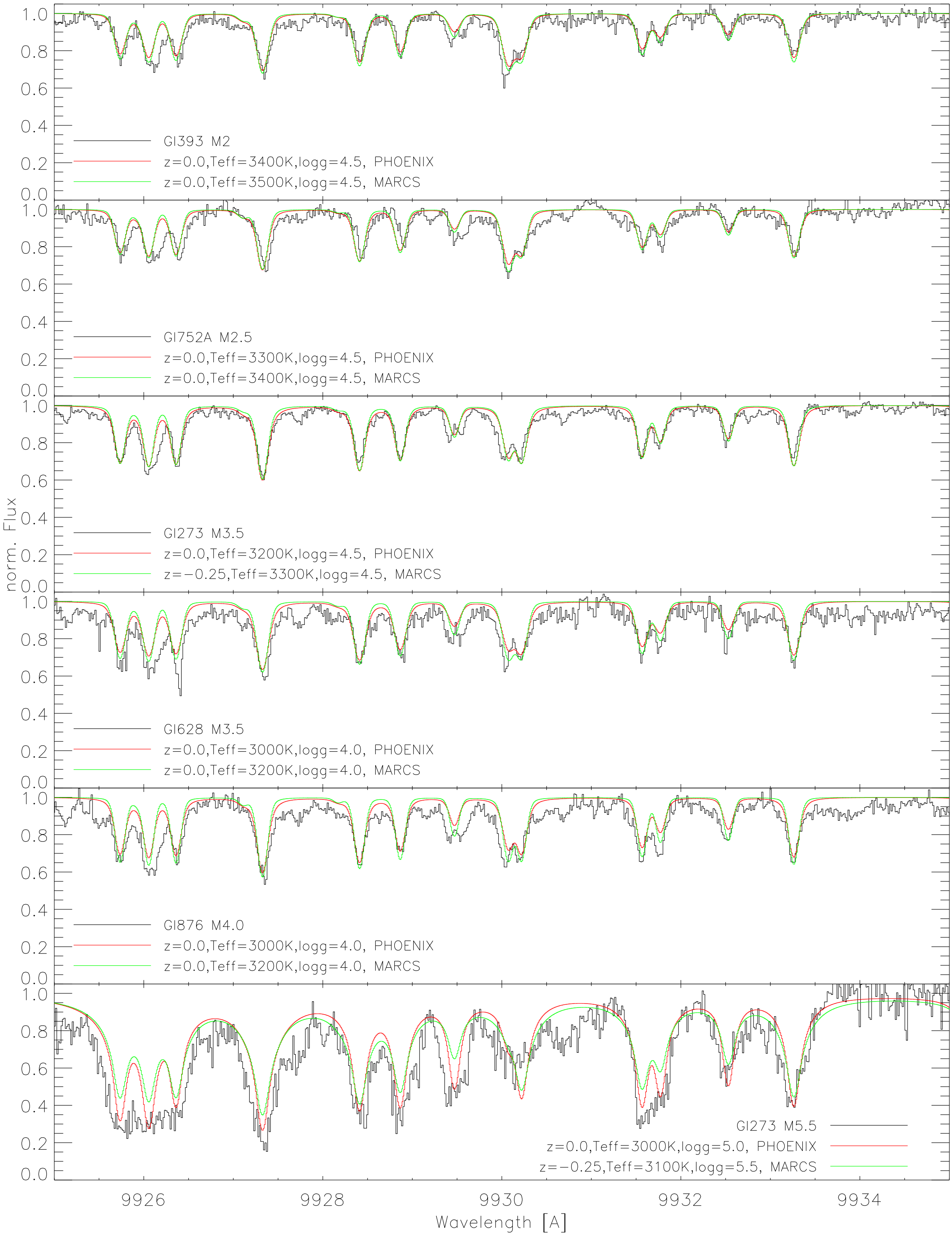

Figure 9.8: Spectra produced on `PHOENIX` (red) and `MARCS` atmospheres for the afore determined effective temperature in comparison with CES observations (black).

Chapter 10

Magnetically Sensitive FeH Lines: An Outlook

That FeH can be used to measure magnetic field strengths was demonstrated by Reiners & Basri (2006, 2007). Theoretical work on the magnetic sensitivity of FeH was published by Berdyugina & Solanki (2002); Berdyugina et al. (2003); Afram et al. (2007, 2008). This chapter should give a short outlook over the magnetically sensitive FeH lines in the range redwards of 1μm.

10.1 Identification of Sensitive Lines

When comparing FeH spectra of an M dwarf with a known strong magnetic field and spectra of an M dwarf with only weak magnetic activity and similar spectral type (i.e. effective temperature), one notices that certain lines of the magnetically active star are broader than their counterparts in the inactive star. This could, of course, be due to different rotation velocities, but since only some lines are affected, the broadening probably stems from the Zeeman effect which also takes place in molecular lines (Berdyugina & Solanki, 2002; Berdyugina et al., 2003). Reiners & Basri (2006, 2007) used this effect to determine magnetic field strengths in a sample of M type dwarfs. To make stars with different effective temperatures comparable, they used a scaling procedure which is inspired by scaling optical depth:

$$S(\lambda) = 1 - C(1 - A(\lambda)^{\alpha}). \tag{10.1}$$

In this expression, $S(\lambda)$ is the resulting scaled spectrum, $A(\lambda)$ the normalized spectrum which will be scaled, α the optical depth scaling factor, which is applied to the overall spectral range, and C is a constant controlling the maximum of absorption due to saturation. To determine the magnetic field strength, they linearly interpolate between a zero field template star and one with known magnetic field. The zero field template star is the M dwarf GJ1002 which was already investigated in this work. For GJ1224 (M 4.5 dwarf), they determined a magnetic field strength of $\sim 2.7 \pm 0.1\,$kG.

I also obtained high-resolution CRIRES[1] spectra for this star over the whole z-range and used it to detect more magnetically sensitive FeH lines redwards of 1μm. For this task, I used the optical depth scaling with $\alpha = 1.24$ for GJ1224 and compared it with the spectra of GJ1002 (both have $v \sin i \leq 3\,\mathrm{km}^{-1}$). Two exemplary spectral bins are shown in Fig. 10.1. It is obvious that some lines are strongly split and others not at all. The unsplit lines were used to scale GJ1224

---

[1] Data were taken at ESO Telescopes under the program 83.D-0124(A)

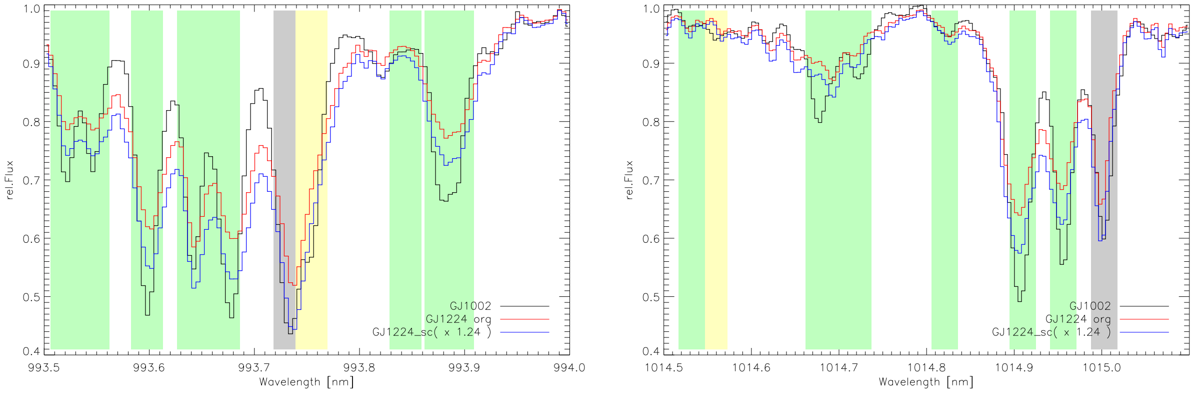

Figure 10.1: Comparison between GJ1224 (red unscaled and blue scaled) and GJ1002 (black). Strong magnetic sensitive lines are highlighted with green, mildly sensitive lines with yellow, and insensitive lines with grey.

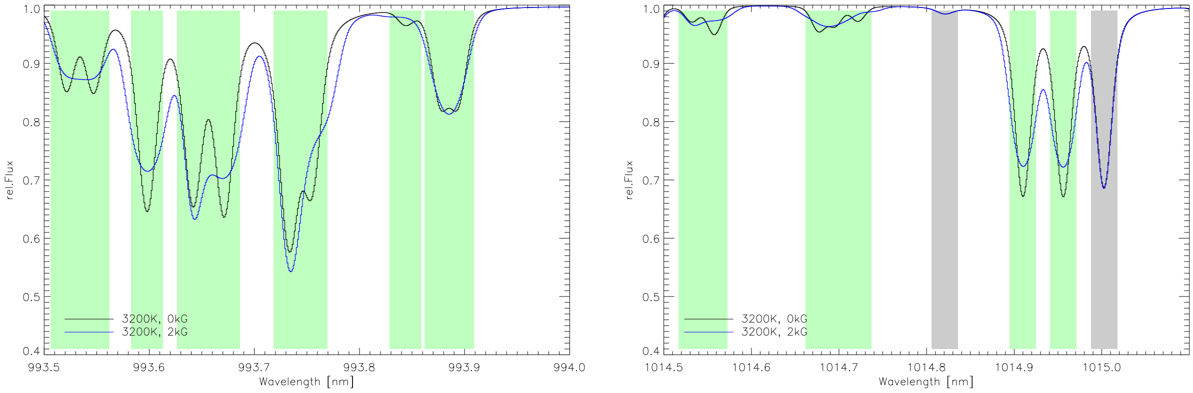

Figure 10.2: Comparison between computed spectra with (2 kG radial field) and without magnetic field. Strong magnetic sensitive lines are highlighted with green and insensitive lines with grey.

to the effective temperature of GJ1002. I will quantify the identification by fitting Gaussian line profiles to the spectra and compare line depths and line widths in Sect. 10.3

10.2 Theoretical Zeeman Splitting

The theoretical description of the Zeeman effect in FeH molecular lines is still a challenging task, since the Born-Oppenheimer Approximation is no longer useful for determining effective Lande g factors. Also, the rovibronic transitions of FeH are mostly in intermediate Hund's case, and the description of the Zeeman splitting must also treated in this intermediate case (Berdyugina & Solanki, 2002; Berdyugina et al., 2003). Not all lines can be described in this case, which make an empirical ansatz necessary (Afram et al., 2007, 2008). A semi-analytical description was presented by Shulyak et al. (2010), who found, that the intermediate case is, in general, a good approximation for the following cases:

1. $\Omega_l = 0.5$

2. $\Omega_{l\ or\ u} \leq 2.5$ and $3Y > J(J+1)$ for P and Q branches
3. $\Omega_{l\ and\ u} = 2.5$ and $5Y > J(J+1)$ for the R branch

Here, $Y = |A_v/B_v|$ is the ratio of the spin-orbit coupling and rotational constants. For all other cases, a good approximation is the assumption of Hund's case (a) for the upper level and Hund's case (b) for the lower level. I adopted this description and use a code from Leroy (2004) (modified by D. Shulyak, priv. communication) to determine Landé factors which describe the strength of the splitting. These factors can be used in the `SYNMAST` code to generate spectra including effects from Zeeman splitting. In Fig. 10.2, the spectral regions from Fig. 10.1 are shown for a computed spectra with zero magnetic field and one with a pure radial 2 kG field. The observed and computed spectra look similar, but the computed splitting is very different from the observed one for some lines. These shortcomings could be related to the inadequate theoretical description of the Zeeman splitting as well as to possible horizontal components in the geometry of the magnetic field. Fig. 10.2 also shows the possibility, that the line depth could be enhanced due to the split components. That means, that it is necessary to investigate the line width as well as the line depth to detect magnetically sensitive lines.

10.3 Comparison Between Computations and Observations

In order to quantify the identification of magnetically sensitive lines, I used a Gaussian fit to the FeH line profiles to measure their depths and widths. This was done for the magnetically broadened spectra as well as for the non magnetic ones. The ratio of the standard deviations σ can be used to investigate if a line is broadened by the magnetic field. The ratio $|1 - I_{mag}/I_{nonmag}|$ can be used to characterise the amount of variation in the line depth. Both quantities are plotted in Figs. 10.3 and 10.4 for the observations and computations as a function of rotational quantum number J. The ratios are separated by Ω since the Landé factor strongly depends on it (Berdyugina & Solanki, 2002). The Landé factor is also a function of J and different for rotational branches. Due to this, the P, Q, and R branches are indicated by different colors. One can see that there is no obvious dependence on J, which would be expected if the splitting were pure Hund's case (a) or (b). The computed spectra almost reproduce the observations, which could be regarded as a sign that the ansatz described above is a good approximation. In these figures, the average ratio is also shown as a function of Ω: the magnetic influence is clear visible stronger for lines with high Ω, in agreement with theory. Again, the results from observations and computations are very similar and differ only in the absolute values. This discrepancy could be due to noise in the observations.

I conclude that the potential of FeH lines for measuring magnetic fields is very high. Empirically, it is already possible to use them, but the results depend on well-chosen and accurate template spectra with known parameters. The theoretical approach is promising, but has to be investigated further to describe the Zeeman splitting more correctly.

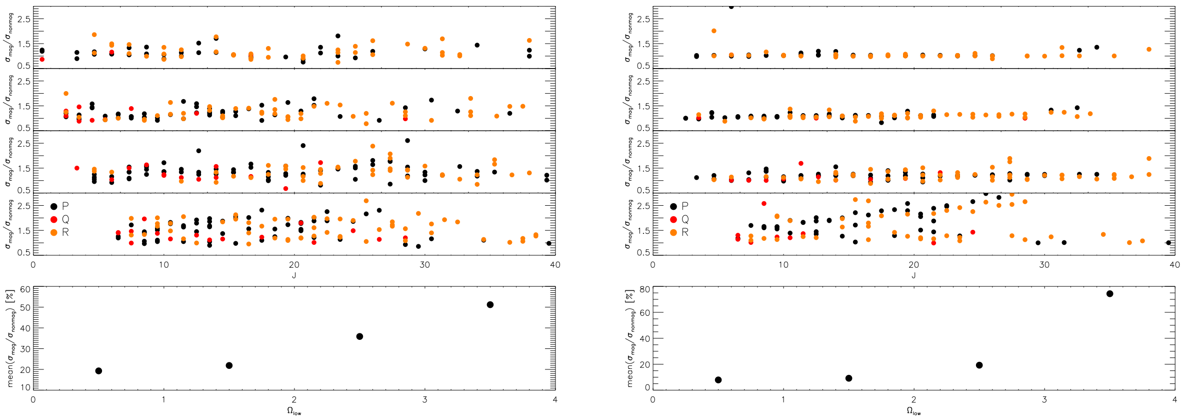

Figure 10.3: Ratio between the widths of the FeH lines in the magnetic and non magnetic case as a function of rotational quantum number J. Left plot shows the results from the observations, right plot from the computations. The lower panels shows the average ratio for each Ω.

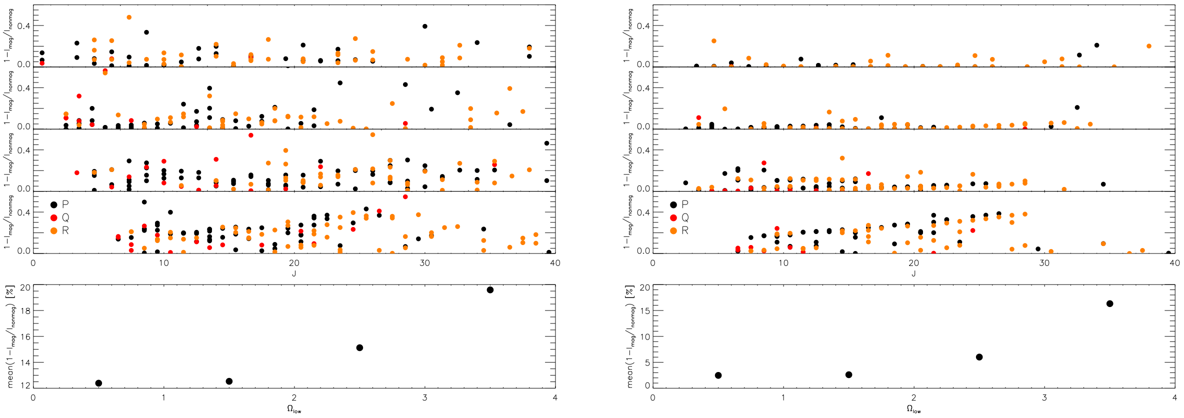

Figure 10.4: Ratio between the depths of the FeH lines in the magnetic and non magnetic case as a function of rotational quantum number J. Left plot shows the results from the observations, right plot from the computations. The lower panels shows the average ratio for each Ω.

Chapter 11

Summary and Conclusion

I have investigated a set of M-star models with $T_{\mathrm{eff}} = 2500\,\mathrm{K}$ - $4000\,\mathrm{K}$ and $\log g = 3.0 - 5.0$ [cgs] using the 3D hydrodynamic radiative transfer code `CO5BOLD`. The horizontal and vertical velocity fields in the 3D models were described with a binning method. The convective turn-over point is clearly visible in the atmospheric velocity dispersion structure. To investigate the influence of these velocity fields on spectral line shapes, a treatment of geometrical projection and limb-darkening effects was applied. With the use of contribution functions, only those parts in the atmosphere where the lines were formed were taken into account. The resulting velocity dispersions range from $400 - 100\,\mathrm{m\,s^{-1}}$ with decreasing $\log g$ and with increasing T_{eff} from $200 - 1400\,\mathrm{m\,s^{-1}}$. These values agree well with velocities deduced from line shapes. The hydrodynamical velocity fields of the 3D models were also expressed in terms of the classical micro- and macro-turbulent velocities. With this description and the obtained micro- and macro-turbulent velocities, it is possible to reproduce 3D spectral lines in 1D atmosphere models very accurately, hence time consuming 3D treatment of FeH molecular lines in the regime of cool stars is not necessary for line profile analysis. A comparison of these velocities with a set of velocities determined from observations with spectral fitting methods showed that the macro-turbulent velocities agree, but the micro-turbulent velocities are a factor of two or three smaller than the ones determined from observations.

A line shift due to the larger up-flowing area in the convection zone was investigated. It is of the order of a few m/s up to $50\,\mathrm{m\,s^{-1}}$ for a very low gravity model. The time dependent jitter in line positions is only about m/s and would be reduced to $\mathrm{mm\,s^{-1}}$ in a real star, due to the high number of contributing elements.

In order to use FeH molecular lines for investigations of spectroscopic/physical properties in cool stars (e.g. Zeeman- or rotational broadening), I explored the behavior of a set of lines for variations in $\log g$ and T_{eff}. Ten FeH lines between 9950Å and 9990Å were investigated on the RHD models with the spectral synthesis code `LINFOR3D`. FeH lines react to different effective temperatures, as expected, due to the change in chemical composition and pressure. The lines also showed a weak dependence on surface gravity due to changing densities and pressure. The broadening from velocity fields in the 3D models of the $\log g$ series is very strong, but for the T_{eff} series the broadening from velocity fields is almost covered by van der Waals broadening. The difference in line width for hot models is up to $0.5\,\mathrm{km\,s^{-1}}$ and for low gravity models around $1\,\mathrm{km\,s^{-1}}$. This means that one has to include correct micro- and macro-turbulent velocities for small surface gravities or hot T_{eff} in 1D spectral synthesis. Due to the fact that the FWHM $\log g$ dependence of FeH lines goes in the opposite direction as the $\log g$ dependence of the velocity fields, the FeH lines become a good way to measure surface gravities in cool stars: the velocity fields scale with $\log g$ and it should be easily possible to detect them.

FeH lines with different quantum numbers do not show significant differences for both $\log g$- and T_{eff}-series. This means that the broadening of the lines does not depend on J, Ω, or the branch. Furthermore, lines with weak magnetic sensitivity behave just like lines with strong magnetic sensitivity: all lines are broadened in the same way by thermal and hydrodynamical motion. Only the transition probability expressed in the $\log gf$ value influences the behavior of the lines. The line with the lowest gf-values did not saturate at low T_{eff}, but in general they are similar to the other FeH lines.

It is possible to treat the FeH molecular lines with different quantum numbers as homogeneous in the absence of magnetic fields. This allows one to use FeH lines to measure magnetic field strengths. Hence I conclude that these lines also are an appropriate means for measuring magnetic field strengths in M-type stars.

Investigations in the z-band region of the M5.5 dwarf GJ1002 with high-resolution CRIRES spectra were done to identify as many FeH lines as possible. This is the region where the $(0,0)$ vibrational band of FeH is present ('Wing-Ford band'). I was able to identify the $(0,0)$, $(1,0)$, $(1,1)$, $(2,1)$, $(2,2)$, $(3,2)$, and $(4,3)$ bands. For confirmation of the band assignment, the methods of coincidence, cross-correlation, and line intensities were used.

For the identified lines, empirical corrections to the theoretical line positions were applied. The deviations between observed and computed positions are Gaussian-distributed around zero. For small deviations (< 0.025 Å), this could be due to uncertainties in the wavelength calibration of the observed spectra and in other cases due to uncertainties in the molecular constants which were used to generate the line list. The method of coincidence confirms the presence of the $(0,0)$ and $(1,1)$ bands, but for the other bands cross-correlation techniques were needed to show their presence. Again the $(0,0)$ and $(1,1)$ bands show clear peaks in the cross-correlation function even with an uncorrected line list, but for the other bands it was necessary to use corrections to the line list to confirm them. I also used line intensity information by plotting the ratio $W_\lambda/S\lambda_0^4$ against E_0, which shows a linear behavior if the band is present in the spectra. With this method I could confirm the presence of all other bands, although not uniquely for the Q-branches.

Corrections to the line strengths in the FeH line list were done by scaling the Einstein A values, as some of these lines show large discrepancies compared to the observations. For this purpose, it was necessary to derive the instrumental broadening (which included the rotational broadening), effective temperature, and an enhancement factor for the van der Waals-broadening constants. The instrumental resolving power for the spectra of GJ1002 was derived to be $R = 70\,000$, which is equivalent to a rotational broadening with $v\sin(i) \sim 1.3\,\mathrm{km\ s^{-1}}$. I also derived an effective temperature of $T_{\mathrm{eff}} = 3100\,\mathrm{K}$, and a van der Waals-enhancement constant of 1.75. The scaling factors of the Einstein A values show an almost linear dependence on J_l, which indicates that there is likely a problem in the calculation of the Hönl-London factors.

With the improved identification of FeH lines, it is now possible to characterize the FeH lines in the z-band region (e.g. magnetically sensitive and insensitive lines, temperature sensitivities of individual lines). The improved line list will aid in the identification and simulation of FeH lines in spectra of cool stars.

From the slope of the line in $[W_\lambda/S\lambda_0^4, E_0]$ plots, it was possible to derive excitation temperatures for rotational transitions, which could be identified with the effective temperature of the star if the lines are formed in the photosphere. I showed that this method is very uncertain because the error in the slope is high. The derived temperatures for the individual vibrational transitions range from $\sim 2500\,\mathrm{K}$ to $\sim 5500\,\mathrm{K}$ for GJ1002, but the weighted mean $\overline{T}_{rot} \approx 3200 \pm 100$ K is very close to the expected temperature of an M 5.5 dwarf. However, the large error bars and differences between P- and R-branch temperatures suggests that this agreement may be more of a coincidence than a physical result.

Better results were obtained from the usage of line pair ratios. These ratios depend strongly on the effective temperature of the star and were relatively easy to measure in a set of CES M dwarf spectra. These ratios were compared with computed line ratios for various effective temperatures to estimate the effective temperature of the observed object. These temperatures were then used to compute model spectra for comparison with the observations, e.g. in order to derive surface gravity and metallicities.

I have identified magnetically sensitive FeH lines in the spectra of the M4.5 dwarf GJ1224, which is magnetically active. The FeH lines were investigated for their possible dependence on rotational quantum number, which was not found, but a strong dependence on Ω could be confirmed. Thus, FeH lines with high Ω (2.5 and 3.5) tend to be highly magnetically sensitive whereas lines with low Ω are, in general, insensitive. I also computed the FeH lines including effects from magnetic fields and compared the results with the observations. In general the computations resemble the observations, but looking at individual line profiles shows that there are still unexplained discrepancies.

Finally, I conclude that molecular FeH lines hold a great potential in exploring atmospheres of cool stars. In the z-range, where these stars are brightest, they are very numerous, strong enough, sufficient narrow, and, in enough cases, well isolated. One can use them to measure broadening from e.g. rotation, turbulent motion, Doppler motion, or Zeeman splitting and also to determine the stellar parameters surface gravity, effective temperature, and metallicity. Since all FeH lines depends on the same number of molecules, line ratios are independent of chemical composition, which is poorly known in cool stars. The large number of suitable lines improves accuracies and would make FeH also a great tool to measure Doppler shifts caused by stellar companions or extrasolar planets.

The science with FeH has just begun, and will probably be even more valuable in the future.

Bibliography

Afram, N., Berdyugina, S. V., Fluri, D. M., Semel, M., Bianda, M. & Ramelli, R. (2007) First polarimetric observations and modeling of the FeH $F^4\Delta$-$X^4\Delta$ system. *A&A*, **473**, L1–L4.

Afram, N., Berdyugina, S. V., Fluri, D. M., Solanki, S. K. & Lagg, A. (2008) The FeH $F^4\Delta$-$X^4\Delta$ system. Creating a valuable diagnostic tool to explore solar and stellar magnetic fields. *A&A*, **482**, 387–395.

Asplund, M., Grevesse, N. & Sauval, A. J. (2005) The Solar Chemical Composition. In *Cosmic Abundances as Records of Stellar Evolution and Nucleosynthesis*, edited by T. G. Barnes, III & F. N. Bash, vol. 336 of *Astronomical Society of the Pacific Conference Series*.

Balfour, W. J., Brown, J. M. & Wallace, L. (2004) Electronic spectra of iron monohydride in the infrared near 1.35 and 1.58 μm. *J. Chem. Phys.*, **121**, 7735–7742.

Barklem, P. S., Piskunov, N. & O'Mara, B. J. (2000) A list of data for the broadening of metallic lines by neutral hydrogen collisions. *A&AS*, **142**, 467–473.

Baschek, B., Holweger, H. & Traving, G. (1966) *Astronomische Abhandlung der Hamburger Sternwarte*, **8**, 26–60.

Basri, G., Marcy, G., Oppenheimer, B., Kulkari, S. R. & Nakajima, T. (1996) Rotation and activity in the coolest stars. In *Cool Stars, Stellar Systems, and the Sun*, edited by R. Pallavicini & A. K. Dupree, vol. 109 of *Astronomical Society of the Pacific Conference Series*.

Bean, J. L. (2007) *M dwarf metallicities and exoplanets*. Ph.D. thesis, The University of Texas at Austin.

Bean, J. L., Benedict, G. F. & Endl, M. (2006a) Metallicities of M Dwarf Planet Hosts from Spectral Synthesis. *ApJ*, **653**, L65–L68.

Bean, J. L., Sneden, C., Hauschildt, P. H., Johns-Krull, C. M. & Benedict, G. F. (2006b) Accurate M Dwarf Metallicities from Spectral Synthesis: A Critical Test of Model Atmospheres. *ApJ*, **652**, 1604–1616.

Berdyugina, S. V. & Solanki, S. K. (2002) The molecular Zeeman effect and diagnostics of solar and stellar magnetic fields. I. Theoretical spectral patterns in the Zeeman regime. *A&A*, **385**, 701–715.

Berdyugina, S. V., Solanki, S. K. & Frutiger, C. (2003) The molecular Zeeman effect and diagnostics of solar and stellar magnetic fields. II. Synthetic Stokes profiles in the Zeeman regime. *A&A*, **412**, 513–527.

Bernath, P. (2005) *Spectra of Atoms and Molecules*. Oxford University Press, Oxford Oxfordshire.

Bessell, M. S. (1991) The late-M dwarfs. *AJ*, **101**, 662–676.

Böhm-Vitense, E. (1958) Über die Wasserstoffkonvektionszone in Sternen verschiedener Effektivtemperaturen und Leuchtkräfte. Mit 5 Textabbildungen. *Zeitschrift fur Astrophysik*, **46**, 108–+.

Casagrande, L., Flynn, C. & Bessell, M. (2008) M dwarfs: effective temperatures, radii and metallicities. *MNRAS*, **389**, 585–607.

Cushing, M. C., Rayner, J. T., Davis, S. P. & Vacca, W. D. (2003) FeH Absorption in the Near-Infrared Spectra of Late M and L Dwarfs. *ApJ*, **582**, 1066–1072.

Cushing, M. C., Rayner, J. T. & Vacca, W. D. (2005) An Infrared Spectroscopic Sequence of M, L, and T Dwarfs. *ApJ*, **623**, 1115–1140.

Dravins, D. (1982) Photospheric spectrum line asymmetries and wavelength shifts. *ARA&A*, **20**, 61–89.

Dulick, M., Bauschlicher, Jr., C. W., Burrows, A., Sharp, C. M., Ram, R. S. & Bernath, P. (2003) Line Intensities and Molecular Opacities of the FeH $F^4\Delta_i$-$X^4\Delta_i$ Transition. *APJ*, **594**, 651–663.

Fawzy, D. E. (1995) *Study of FeH molecular lines in an umbral spectrum*. Master's thesis, M. Sci.-Thesis, Cairo University (1995).

Fawzy, D. E., Youssef, N. H. & Engvold, O. (1998) Identification of FeH molecular lines in the spectrum of a sunspot umbra. *A&AS*, **129**, 435–443.

Ferguson, J. W., Alexander, D. R., Allard, F., Barman, T., Bodnarik, J. G., Hauschildt, P. H., Heffner-Wong, A. & Tamanai, A. (2005) Low-Temperature Opacities. *APJ*, **623**, 585–596.

Fliessbach, T. (2000) *Quantenmechanik*. Spektrum-Akademischer-Verlag, Berlin.

Freytag, B., Allard, F., Ludwig, H., Homeier, D. & Steffen, M. (2009) The role of convection, overshoot, and gravity waves for the transport of dust in the atmospheres of M dwarf stars and brown dwarfs. *A&A*, **in prep.**

Freytag, B., Allard, F., Ludwig, H., Homeier, D. & Steffen, M. (2010) The role of convection, overshoot, and gravity waves for the transport of dust in M dwarf and brown dwarf atmospheres. *A&A*, **513**, A19+.

Freytag, B., Steffen, M., Ludwig, H.-G. & Wedemeyer-Boehm, S. (2008) Radiation hydrodynamics simulations of stellar surface convection. *Astrophysics Software Database*, 36–+.

Gray, D. F. (1975) Atmospheric turbulence measured in stars above the main sequence. *ApJ*, **202**, 148–164.

Gray, D. F. (1977) A test of the micro-macroturbulence model on the solar flux spectrum. *ApJ*, **218**, 530–538.

Gray, D. F. (2008) *The Observation and Analysis of Stellar Photospheres*. The Observation and Analysis of Stellar Photospheres, by D.F. Gray. Cambridge: Cambridge University Press, 2008.

Grevesse, N. & Anders, E. (1989) Solar-system abundances of the elements - A new table. In *Cosmic Abundances of Matter*, edited by C. J. Waddington, vol. 183 of *American Institute of Physics Conference Series*.

Grevesse, N., Asplund, M. & Sauval, A. J. (2007) The Solar Chemical Composition. *Space Science Reviews*, **130**, 105–114.

Gustafsson, B., Edvardsson, B., Eriksson, K., Jørgensen, U. G., Nordlund, Å. & Plez, B. (2008) A grid of MARCS model atmospheres for late-type stars. I. Methods and general properties. *A&A*, **486**, 951–970.

Hargreaves, R. J., Hinkle, K. H., Bauschlicher, C. W., Wende, S., Seifahrt, A. & Bernath, P. F. (2010) High-resolution 1.6 μm Spectra of FeH in M and L Dwarfs. *AJ*, **140**, 919–924.

Hauschildt, P. H. & Baron, E. (1999) Numerical solution of the expanding stellar atmosphere problem. *Journal of Computational and Applied Mathematics*, **109**, 41–63.

Herzberg, G. (1950) *Molecular spectra and molecular structure. Vol.1: Spectra of diatomic molecules*.

Kippenhahn, R. (1990) *Stellar Structure and Evolution*. Springer-Verlag, Berlin.

Kippenhahn, R. & Weigert, A. (1990) *Stellar Structure and Evolution*.

Kirkpatrick, J. D., Henry, T. J. & McCarthy, Jr., D. W. (1991) A standard stellar spectral sequence in the red/near-infrared - Classes K5 to M9. *ApJS*, **77**, 417–440.

Kochukhov, O. P. (2007) Spectrum synthesis for magnetic, chemically stratified stellar atmospheres. In *Physics of Magnetic Stars*.

Kupka, F., Piskunov, N., Ryabchikova, T. A., Stempels, H. C. & Weiss, W. W. (1999) VALD-2: Progress of the Vienna Atomic Line Data Base. *A&AS*, **138**, 119–133.

Kurucz, R. L. (1970) Atlas: a Computer Program for Calculating Model Stellar Atmospheres. *SAO Special Report*, **309**.

Leroy, B. (2004) Molecular Zeeman Library Reference Manual (available on-line at http://bass2000.obspm.fr/mzl/download/mzl-ref.pdf).

Ludwig, H. G. (1992) Ph.D. thesis, University of Kiel.

Ludwig, H.-G., Allard, F. & Hauschildt, P. H. (2002) Numerical simulations of surface convection in a late M-dwarf. *A&A*, **395**, 99–115.

Ludwig, H.-G., Allard, F. & Hauschildt, P. H. (2006) Energy transport, overshoot, and mixing in the atmospheres of M-type main- and pre-main-sequence objects. *A&A*, **459**, 599–612.

Ludwig, H.-G., Jordan, S. & Steffen, M. (1994) Numerical simulations of convection at the surface of a ZZ Ceti white dwarf. *A&A*, **284**, 105–117.

Magain, P. (1986) Contribution functions and the depths of formation of spectral lines. *A&A*, **163**, 135–139.

Messina, S., Rodonò, M. & Guinan, E. F. (2001) The "rotation-activity connection": Its extension to photospheric activity diagnostics. *A&A*, **366**, 215–228.

Mihalas, D. (1999) *Foundations of Radiation Hydrodynamics.* Dover, Mineola.

Mortimer, C. (2001) *Chemie. Das Basiswissen Der Chemie.* Ignatius Press, San Francisco.

Nordh, H. L., Lindgren, B. & Wing, R. F. (1977) A proposed identification of FeH in the spectra of M dwarfs and S stars. *A&A*, **56**, 1–2.

Nordlund, A. (1982) Numerical simulations of the solar granulation. I - Basic equations and methods. *A&A*, **107**, 1–10.

Palla, F. & Baraffe, I. (2005) Pulsating young brown dwarfs. *A&A*, **432**, L57–L60.

Phillips, J. G., Davis, S. P., Lindgren, B. & Balfour, W. J. (1987) The near-infrared spectrum of the FeH molecule. *ApJS*, **65**, 721–778.

Piskunov, N. E., Kupka, F., Ryabchikova, T. A., Weiss, W. W. & Jeffery, C. S. (1995) VALD: The Vienna Atomic Line Data Base. *A&AS*, **112**, 525–+.

Reid, I. N. & Hawley, S. L. (2005) *New light on dark stars : red dwarfs, low-mass stars, brown dwarfs.*

Reiners, A. (2007) The narrowest M-dwarf line profiles and the rotation-activity connection at very slow rotation. *A&A*, **467**, 259–268.

Reiners, A. & Basri, G. (2006) Measuring Magnetic Fields in Ultracool Stars and Brown Dwarfs. *ApJ*, **644**, 497–509.

Reiners, A. & Basri, G. (2007) The First Direct Measurements of Surface Magnetic Fields on Very Low Mass Stars. *ApJ*, **656**, 1121–1135.

Russell, H. N. & Bowen, I. S. (1929) Is There Argon in the Corona? *ApJ*, **69**, 196–+.

Sauval, A. J. & Tatum, J. B. (1984) A set of partition functions and equilibrium constants for 300 diatomic molecules of astrophysical interest. *ApJS*, **56**, 193–209.

Schadee, A. (1964) The formation of molecular lines in the solar spectrum (Errata: 17 537). *Bull. Astron. Inst. Netherlands*, **17**, 311–+.

Schiavon, R. P., Barbuy, B. & Singh, P. D. (1997) The FeH Wing-Ford Band in Spectra of M Stars. *ApJ*, **484**, 499–+.

Schweitzer, A., Hauschildt, P. H., Allard, F. & Basri, G. (1996) Analysis of Keck high-resolution spectra of VB 10. *MNRAS*, **283**, 821–829.

Shulyak, D., Reiners, A., Wende, S., Kochukhov, O., Piskunov, N. & Seifahrt, A. (2010) Modelling the molecular Zeeman-effect in M-dwarfs: methods and first results. *A&A*, **523**, A37+.

Simon, T. (2001) The Connection Between Rotation and Activity (CD-ROM Directory: contribs/simon). In *11th Cambridge Workshop on Cool Stars, Stellar Systems and the Sun*, edited by R. J. Garcia Lopez, R. Rebolo, & M. R. Zapaterio Osorio, vol. 223 of *Astronomical Society of the Pacific Conference Series*.

Sneden, C. A. (1973) *Carbon and Nitrogen Abundances in Metal-Poor Stars.* Ph.D. thesis, AA(THE UNIVERSITY OF TEXAS AT AUSTIN.).

Steffen, M., Ludwig, H.-G. & Freytag, B. (1995) Synthetic spectra computed from hydrodynamical model atmospheres of DA white dwarfs. *A&A*, **300**, 473–+.

Tatum, J. B. (1966) Accurate Partition Functions and Dissociation Equilibrium Constants of Diatomic Molecules of Astrophysical Interest. *Publications of the Dominion Astrophysical Observatory Victoria*, **13**, 1–+.

Unsöld, A. (1955) *Physik der Sternatmospharen, MIT besonderer Berucksichtigung der Sonne.*

Vögler, A., Bruls, J. H. M. J. & Schüssler, M. (2004) Approximations for non-grey radiative transfer in numerical simulations of the solar photosphere. *A&A*, **421**, 741–754.

Wallace, L., Hinkle, K. & Livingston, W. (1998) *An atlas of the spectrum of the solar photosphere from 13,500 to 28,000 cm-1 (3570 to 7405 A).*

Wallace, L., Livingston, W. C., Bernath, P. F. & Ram, R. S. (1999) *An atlas of the sunspot umbral spectrum in the red and infrared from 8900 to 15,050 cm(-1) (6642 to 11,230 [angstroms]), revised.*

Wende, S., Reiners, A. & Ludwig, H. (2009) 3D simulations of M star atmosphere velocities and their influence on molecular FeH lines. *A&A*, **508**, 1429–1442.

Wende, S., Reiners, A., Seifahrt, A. & Bernath, P. F. (2010) CRIRES spectroscopy and empirical line-by-line identification of FeH molecular absorption in an M dwarf. *A&A*, **523**, A58+.

Wilkinson, P. G. (1963) Diatomic Molecules of Astrophysical Interest: Ionization Potentials and Dissociation Energies. *ApJ*, **138**, 778–+.

Wing, R. F. (1972) Molecular absorption spectra of S-type stars in the one-micron region. In *Les Spectres des Astres dans l'Infrarouge et les Microondes.*

Wing, R. F. & Ford, W. K. J. (1969) The Infrared Spectrum of the Cool Dwarf Wolf 359. *PASP*, **81**, 527–529.

Wöhl, H. (1970) On Rotational Temperatures of Umbrae. *Sol. Phys.*, **15**, 342–344.

Appendix

FeH Data

Table 8.4 contains the observed wavelength λ_{obs}, which is obtained with the Voigt fit, and the theoretical wavelength λ_{theo} from the list of Dulick et al. (2003). The wavelengths are in vacuum. I also give the quantum numbers of the lines and the Einstein A values with their scaling factors s_A. The lower-level energy E_l is given in eV. The difference in position $\Delta\lambda = \lambda_{theo} - \lambda_{obs}$ is also printed in the table. If the line is a blended line, then its contribution to the blend is given as the fraction normalized to one. If the line is not blended, its blend value is one. Then, the classification of the line as defined in Sect. 8.2.3 is given. I add a comment if the line is blended by an atomic feature, or if the classification of the line did not agree with the scaling factor of the Einstein A values.

Explanation of the FeH Atlas

I plotted the whole spectrum in bins of 1 nm from 990 nm to 1076.6 nm. Shown are the observed spectrum of GJ1002 (black), the computed spectrum with corrected positions (red), the computed spectrum with corrected positions and scaled Einstein A values (green). I also labeled all lines with $W_\lambda \geq 2\,\mathrm{m\AA}$ with quantum numbers for the vibrational transition, the branch, the lower J, the upper and lower Ω, and in the last position, their blend fraction. The blend fraction is unity if a line is not blended. Also labeled is the position of atomic lines with the element name below the spectrum.

Danksagung

Zuerst einmal möchte ich vorwegschicken, dass solch eine Danksagung nicht das ausdrücken kann, was einigen Leuten gebührt. Auch die Reihenfolge des Dankes sollte nicht überbewertet werden, da sie nur eine Ordnung dessen ist, was man nicht ordnen sollte. Nichtsdestotrotz, möchte ich meine Danksagung mit dem Dank an meinen Betreuer Ansgar Reiners beginnen:

Ich danke Ansgar für die Art und Weise, wie er mich meine Arbeit verrichten ließ. Er hielt sich immer mit zu eng gefassten Anweisungen zurück und ermöglichte es mir somit meine eigene Arbeitsweise und meinen eigenen Geist zu entwickeln. Auch meine eigene Disziplin wurde durch den geringen bis gar nicht ausgeübten Druck auf die Probe gestellt und trainiert.

Wenn ich ihn brauchte, war er hingegen immer zur Stelle und konnte meine Fragen auf kompetenteste Weise beantworten sowie sehr lohnenswerte Hinweise geben. Sein Gespür für die Natur der Sache ist unbezahlbar und unermesslich hilfreich nicht nur wenn ich nicht weiter wusste.

Daher: Danke Ansgar für die schönen drei Jahre meiner Doktorarbeit. Und auch für die vielleicht noch schöneren zwei Monate meiner Elternzeit, die ich dank der unkomplizierten Handhabung sehr geniessen konnte.

Mein nächster Dank geht an das CO^{5}BOLD team (Bernd Freytag, Sven Wedemeyer-Böhm, Matthias Steffen und Hans-Günther Ludwig), welches mir grade in der Anfangsphase aber auch darüberhinaus eine immens große Hilfe war. Insbesondere möchte ich hier Hans-Günther danken, der quasi den ersten Teil meiner Arbeit betreut hat. Er konnte mich durch sein klares theoretisches Wissen immer wieder erhellen und mich durch seine *Mausfragen* auf schöne Art und Weise auf die Probe stellen.

Des weiteren danke ich Derek Homeier, den ich immer wieder mit Fragen physikalischer und numerischer Natur behelligen durfte. Sein enorm breitgefächertes Wissen führte zudem zu sehr erkenntnissreichen Diskussionen und Gesprächen.

Weiterhin danke ich Peter Hauschildt für seine Hilfe während meiner Arbeit sowie für das Referieren meiner Dissertation.

Auch möchte ich Sonja Schuh danken, für ihre hilfreichen Tipps und Beistand während der Promotionszeit.

Ganz besonders danke ich Stefan Dreizler für das Referieren meiner Arbeit und seine großartige Arbeit als Leiter unserer Abteilung. Die angemehme Atmosphäre innerhalb der Arbeitsgruppe ermöglichte ein schönes und produktives Schaffen. An dieser Stelle danke ich der gesammten Abteilung "Stellare Astrophysik". Insbesondere danke ich hier Rick Hessman für seine Hilfe bei diversen Fragen der englischen Sprache sowie für die sprachliche Durchsicht meiner Dissertation.

Ich danke Klaus Reinsch, der mir desöfteren meine Rechner wieder zum Laufen brachte und in letzter Minute noch meine Arbeit rettete.

Ich danke der kompletten Emmy-Noether Nachwuchsgruppe, deren Teil ich bin, für die schöne, produktive und spaßige Zusammenarbeit.

Ich bedanke mich ganz herzlich bei Simon Daniel Hügelmeyer für unzählige wissenschaftliche und

auch private Diskussionen sowie für wunderschöne Konferenzen und Dienstreisen.

Bei Andreas Seifahrt möchte ich mich auch bedanken für die wirklich schöne Zeit mit ihm und die äußerst interessanten Diskussionen. Auch bedanke ich mich bei Nandan Joshi, Ronny Lutz, Timo Reinhold, Richard Anderson, Ulf Seemann, Marin Treslj (nice time man), und Feo Lenz für die schöne Zeit.

Ebenfalls für die schöne Zeit bedanke ich mich bei Markus Hundertmark, der mich nun schon seit gut vier Jahren als super Bürokollege begleitet. Danke Markus für deine Hilfe bei all meinen Fragen, und das waren und sind eine Menge, und für deine Akzeptieren aller meiner Eigenheiten und Macken, die so im Büroalltag zu Tage treten.

Jetzt möchte ich mich noch bei einer Gruppe von *Jungs* bedanken, ohne die ich es gar nicht bis hierhin geschafft hätte. Danke Jan, danke Jens, danke Tobi, danke Moped und danke Raffi (Naib, Tresor, Schniebli, ...).

Weiterer Dank geht an Klaudia Wolters, Melanie Hüttenmeister und Nicole Böker, ohne deren Hilfe ich oftmals im Dschungel der Bürokratie verschollen gewesen wäre.

Den letzten Abschnitt dieser Danksagung widme ich meiner Familie, die sich wie schon erwähnt, während der Promotionszeit vergrössert hat.

Ich danke meiner Freundin Alice von Berg für ihre Unterstützung, Rückendeckung und ihre großartige Arbeit in der Erziehung unseres Sohnes Marin von Berg.

Meiner Mutter, Marion Peterwitz, danke ich für ihre Liebe und Wärme, die mir immer wieder Kraft geben hat für meine Aufgaben. Meinem Vater, Michel Wende, danke ich für seine Unterstützung materieller wie geistiger Natur während meines Studiums.

Für die Übernahme diverser Wohnungs- und Katzen-Sitter Tätigkeiten danke ich meiner Schwester Katarina Wende, ohne die keine erholsamen Urlaube während der Promotion möglich gewesen wären.

Zu guter Letzt möchte ich all meinen Grosseltern danken, die mittlerweile alle diese Welt verlassen haben. Sie waren immer eine großartige Inspiration und Stütze auf meinen Wegen.

Curriculum Vitae

Dipl.-Phys. Sebastian Wende
Am Feuerschanzengraben 1
37083 Göttingen

Geburtstag: 09.06.1980
Geburtsort: Osterode/Harz
Staatsangehörigkeit: Deutsch

09/2007 – 10/2010	Promotionsstipendiat (Universität Göttingen)
09.08.2007	Diplom Physik (Universität Göttingen)
21.10.2005	Vordiplom Physik (Universität Göttingen)
10/2002 – 08/2007	Physikstudium (Universität Göttingen)
14.06.2002	allgemeine Hochschulreife
08/2000 – 06/2002	BBS I Arnoldi-Schule Göttingen
09/1999 – 08/2000	Zivildienst in Osterode
08/1998 – 07/1999	BBS I Osterode
08/1993 – 07/1998	Tillman-Riemenschneider Gymnasium Osterode
08/1991 – 07/1993	Orientierungsstufe Röddenberg Osterode
08/1987 – 07/1991	Grundschule Röddenberg Osterode